

**Characterization of coke obtained  
over MgO-modified Ni/SiO<sub>2</sub>  
in the decomposition of methane.**

**By**

**Prisca Ndhlovu**

# Declaration

I know the meaning of plagiarism and I declare that all the work in this dissertation is my own, unaided work. It is being submitted for the degree of Masters of Science in the University of the Witwatersrand. It has not been submitted before for any degree or examination in any other body or organization or person outside the University of the Witwatersrand, Johannesburg.

-----

(Signed) Prisca Ndhlovu

-----Day of ----- 2010

# **Dedications**

*Dedicated to my parents*

*Mr and Mrs Ndlovu*

# Acknowledgements

Firstly, I would like to thank Professor M. Scurrall for the guiding me through my confusion and his patience and support.

I am also grateful to the staff and students in the school of chemistry who made my studies and life in the department fun.

To the CATOMAT group, especially K. Salipira, your support and love for laughter made boring days and nights of dry literature come to life!

I fully acknowledge SANERI and the University of the Witswatersrand for their financial assistance.

This thesis would not exist if the Almighty, had not granted it. To my family, I will always be grateful for your support towards my selfish pursuit of the intellectual life.

**Poster presentations arising from this work:**

Characterization of coke obtained over MgO-modified Ni/SiO<sub>2</sub> in the decomposition of methane in “CO<sub>x</sub>-free H<sub>2</sub> production, CATSA conference, Cape Town, (2009)

## Abstract

In the present work, the effect of MgO incorporation on the catalytic performance of a conventional 20%Ni/SiO<sub>2</sub> catalyst in the direct methane decomposition for CO<sub>x</sub>-free H<sub>2</sub> production at an optimum temperature of 600 °C was investigated. A series of MgO modified 20%Ni/SiO<sub>2</sub> catalysts of Mg<sub>at</sub>/Ni<sub>at</sub> ratio of 0.1-2.2 were prepared by the co-impregnation method and the physico-chemical properties characterized using ICP, BET, H<sub>2</sub>-chemisorption, TPR and XRD. The highest pseudo steady state methane conversions for all the catalysts were in the range of 45-55%. The effect of MgO incorporation in the 20%Ni/SiO<sub>2</sub> catalyst on the nature of the coke was also investigated. TEM, TGA, Raman and IR spectroscopy studies on the coke revealed that the MgO had little effect on the nature of the coke. CHNS analysis revealed that high coke yields were obtained with catalysts with an average Ni particle size of 36 nm, high degree of reduction and low MgO content, indicating that Ni catalysed methane decomposition is dependent on the size of Ni particle, the reducibility of the nickel species and perhaps MgO enhanced coke gasification. The unmodified 20%Ni/SiO<sub>2</sub> had the best performance in terms of coke capacity (3.0g<sub>C</sub>/g<sub>cat</sub>). The optimum ratio of Mg<sub>at</sub>/Ni<sub>at</sub> in 20%Ni/SiO<sub>2</sub> for methane decomposition was 0.1, with a coke capacity of 2.6g<sub>C</sub>/g<sub>cat</sub>. Initial attempts to separate the coke from the spent catalyst are also presented.

## List of Tables

<b>Table 2.1</b> A summary of the possible applications for other components of the spent Ni catalysts .....	<b>31</b>
<b>Table 4.1</b> Inductively Coupled Plasma -Atomic Emission Spectroscopy (ICP-AES) analysis results.....	<b>50</b>
<b>Table 4.2</b> Physico-chemical properties of the 20%Ni/SiO <sub>2</sub> catalysts.....	<b>51</b>
<b>Table 4.3</b> Surface area and pore volume measurements from nitrogen physisorption.....	<b>71</b>
<b>Table 4.4</b> Effect of temperature on structural disorder.....	<b>77</b>
<b>Table 4.5</b> Effect of MgO addition on carbon nanofilament structural disorder.....	<b>79</b>
<b>Table 4.6</b> Mass of the spent catalyst before and after Soxhlet extraction.....	<b>83</b>
<b>Table 4.7</b> Results for nickel leaching.....	<b>85</b>

## List of figures

<b>Figure 2.1</b> An illustration of estimated global carbon dioxide emissions.....	9
<b>Figure 2.2</b> Geographical distribution of proven natural gas reserves.....	10
<b>Figure 2.3</b> Deactivation mechanisms: (A) coke formation, (B) poisoning, (C) sintering of active metal particles and (D) sintering and solid-solid phase transitions and encapsulation of active metal particle.....	17
<b>Figure 2.4</b> An illustration of growth process of the CNTs.....	22
<b>Figure 3.1</b> A schematic diagram for the reactor system.....	42
<b>Figure 3.2</b> A typical gas chromatogram of the exit gas obtained from catalytic methane decomposition over 20%Ni/SiO <sub>2</sub> catalyst.....	43
<b>Figure 4.1</b> Typical XRD pattern for MgO -modified 20%Ni/SiO <sub>2</sub> catalysts.....	53
<b>Figure 4.2</b> XRD patterns of SiO <sub>2</sub> , N-SiO <sub>2</sub> , 1M9N-SiO <sub>2</sub> , 1M4N-SiO <sub>2</sub> , 1M2N-SiO <sub>2</sub> , 1M1N-SiO <sub>2</sub> and 2M1N-SiO <sub>2</sub> .....	54
<b>Figure 4.3</b> TPR profile for NiO, N-SiO <sub>2</sub> , 1M9N-SiO <sub>2</sub> , 1M4N-SiO <sub>2</sub> , 1M2N-SiO <sub>2</sub> , 1M1N-SiO <sub>2</sub> and 2M1N-SiO <sub>2</sub> catalysts.....	55
<b>Figure 4.4</b> Carbon yield obtained over N-SiO <sub>2</sub> in the range of 500 - 800°C.....	58
<b>Figure 4.5</b> Carbon yield on N-SiO <sub>2</sub> , 1M9N-SiO <sub>2</sub> , 1M4N-SiO <sub>2</sub> , 1M2N-SiO <sub>2</sub> , 1M1N-SiO <sub>2</sub> , 2M1N-SiO <sub>2</sub> catalysts at 600 °C.....	59
<b>Figure 4.6</b> Graphical illustrations of $g_C/g_{N_{\text{ired}}}$ values for yields obtained over N-SiO <sub>2</sub> , 1M9N-SiO <sub>2</sub> , 1M4N-SiO <sub>2</sub> , 1M2N-SiO <sub>2</sub> , 1M1N-SiO <sub>2</sub> and 2M1N-SiO <sub>2</sub> catalysts at 600 °C.....	61
<b>Figure 4.7a</b> TEM micrograph of carbon nanofilaments obtained over the N-SiO <sub>2</sub> catalyst at 600 °C.....	63
<b>Figure 4.7b</b> Diameter distribution of carbon nanofilaments obtained over the N-SiO <sub>2</sub> catalyst at 600 °C.....	64
<b>Figure 4.8a</b> TEM micrograph of carbon nanofilaments obtained over the 1M9N-SiO <sub>2</sub> catalyst at 600 °C.....	64
<b>Figure 4.8b</b> Diameter distributions of carbon nanofilaments obtained over the 1M9N-SiO <sub>2</sub> catalyst at 600 °C.....	65
<b>Figure 4.9a</b> TEM micrograph of carbon nanofilaments obtained over the 1M4N-SiO <sub>2</sub> catalyst at 600 °C.....	65
<b>Figure 4.9b</b> Diameter distributions of carbon nanofilaments obtained over the 1M4N-SiO <sub>2</sub> catalyst at 600 °C.....	66

<b>Figure 4.10a</b> TEM micrograph of carbon nanofilaments obtained over the 1M2N-SiO <sub>2</sub> catalyst at 600 °C.....	<b>66</b>
<b>Figure 4.10b</b> Diameter distributions of carbon nanofilaments obtained over the 1M2N-SiO <sub>2</sub> catalyst at 600 °C.....	<b>67</b>
<b>Figure 4.11a</b> TEM micrograph of carbon nanofilaments obtained over the 1M1N-SiO <sub>2</sub> catalyst at 600 °C.....	<b>67</b>
<b>Figure 4.11b</b> Diameter distributions of carbon nanofilaments obtained over the 1M1N-SiO <sub>2</sub> catalyst at 600 °C.....	<b>68</b>
<b>Figure 4.12a</b> TEM micrograph of carbon nanofilaments obtained over the 2M1N-SiO <sub>2</sub> catalyst at 600 °C.....	<b>68</b>
<b>Figure 4.12b</b> Diameter distributions of carbon nanofilaments obtained over the 2M1N-SiO <sub>2</sub> catalyst at 600 °C.....	<b>69</b>
<b>Figure 4.13</b> TEM micrograph of a carbon nanofiber obtained over the 1M2N-SiO <sub>2</sub> catalyst at 500 °C, showing the presence of the Ni particle at the tip of the carbon nanofiber.....	<b>69</b>
<b>Figure 4.14</b> Corresponding EDX pattern of the carbon nanofiber obtained over the 1M2N-SiO <sub>2</sub> catalyst at 500 °C.....	<b>70</b>
<b>Figure 4.15</b> Methane conversion profiles of the 20% Ni/SiO <sub>2</sub> catalysts; N-SiO <sub>2</sub> , 1M9N-SiO <sub>2</sub> , 1M4N-SiO <sub>2</sub> , 1M2N-SiO <sub>2</sub> , 1M1N-SiO <sub>2</sub> and 2M1N-SiO <sub>2</sub> catalysts at 600 °C.....	<b>74</b>
<b>Figure 4.16</b> A typical Lorentzian-Gaussian fit of a Raman spectrum obtained from coke deposited on 20%Ni/SiO <sub>2</sub> catalyst at 600 °C.....	<b>75</b>
<b>Figure 4.17</b> Raman spectra of carbon nanofilaments obtained over N-SiO <sub>2</sub> at; (a) 500 °C, (b) 600 °C, (c) 700 °C and (d) 800 °C.. ..	<b>76</b>
<b>Figure 4.18</b> Raman spectra of carbon nanofilaments obtained over unmodified-Ni/SiO <sub>2</sub> and MgO- modified Ni/SiO <sub>2</sub> catalysts; (a) N-SiO <sub>2</sub> , (b) 1M9N-SiO <sub>2</sub> , (c) 1M4N-SiO <sub>2</sub> , (d) 1M2N-SiO <sub>2</sub> , (e) 1M1N-SiO <sub>2</sub> (f) 2M1N-SiO <sub>2</sub> at 600 °C.....	<b>78</b>
<b>Figure 4.19</b> The oxidative stability curves for the carbon nanofilaments obtained at 600 °C over the unmodified and MgO-modified Ni/SiO <sub>2</sub> catalysts; N-SiO <sub>2</sub> , 1M9N-SiO <sub>2</sub> , 1M4N-SiO <sub>2</sub> , 1M2N-SiO <sub>2</sub> , 1M1N-SiO <sub>2</sub> and 2M1N-SiO <sub>2</sub> at 600 °C.....	<b>80</b>
<b>Figure 4.20</b> The differential curve for the carbon nanofilaments obtained at 600 °C over the 1M2N-SiO <sub>2</sub> catalyst.....	<b>81</b>

<b>Figure 4.21</b> FTIR transmission spectra of the spent catalyst obtained over (a) N-SiO <sub>2</sub> , (b) 1M1N-SiO <sub>2</sub> catalysts at 600 °C.....	<b>82</b>
<b>Figure 4.22</b> Chromatogram of neat Toluene before Soxhlet extraction.....	<b>84</b>
<b>Figure 4.23</b> Chromatogram of Toluene after Soxhlet extraction.....	<b>84</b>
<b>Figure 4.24</b> TEM micrograph of the carbon nanofilaments obtained over N-SiO <sub>2</sub> catalyst at 600 °C after nickel leaching.....	<b>85</b>

## Nomenclature

### Abbreviation Description

BET	Brunauer-Emmett-Teller
CH <sub>4</sub>	Methane/Natural gas
CHNS	Carbon, Hydrogen, Sulphur and Nitrogen elemental analysis
CNTs	Carbon nanotubes
CNFs	Carbon nanofibers
CTEM	Conventional Transmission Electron Microscopy
$d_s$	Crystallite diameters
% <i>D</i>	Percentage dispersion
DFT	Density Functional Theory
DRIFTS	Diffuse Reflectance Infrared Fourier Transform Spectroscopy
EDX	Energy Dispersive X-ray Analysis
EM	Electron Microscopy
FID	Flame Ionization Detector
FTIR	Fourier Transform Infrared Spectroscopy
GC	Gas Chromatography
GTL	Gas-to-liquid
h	Hours
MWNTs	Multi-walled carbon nanotubes
TEM	Transmission Electron Microscope
TCD	Thermal Conductivity Detector
TGA	Thermogravimetric Analysis
TPH	Temperature Programmed Hydrogenation
TPR	Temperature Programmed Reduction
T <sub>R</sub>	Temperature of methane decomposition
ICP-AES	Inductively Coupled Plasma -Atomic Emission Spectroscopy
IR	Infrared Spectroscopy
SA <sub>BET</sub>	Surface Area
SMSI	Strong Metal-Support Interactions
XRD	X-Ray Diffraction

## CONTENTS

Dedications.....	i
Acknowledgements.....	ii
Poster presentations.....	iii
Abstract.....	iv
List of Tables.....	v
List of Figures.....	vi
Nomenclature.....	ix
Contents.....	x

### CHAPTER 1 INTRODUCTION

1.0 Introduction.....	1
1.1 Project Justification.....	2
1.2 Aims of the project.....	4
1.3 Outline of the dissertation.....	5
1.4 References.....	6

### CHAPTER 2 LITERATURE REVIEW

2.0 Introduction.....	8
2.1 Background.....	8
2.2 The Effect of Metals in Catalytic Methane Decomposition.....	12
2.3 The effect of support in the catalytic methane decomposition.....	13
2.4 Catalyst Deactivation.....	16
2.4.1 Coke Deposition/ Formation.....	17
2.4.2 Sintering and Attrition.....	19
2.4.3 Sulphur Poisoning.....	20
2.5 Mechanism of Coke formation.....	20
2.5.1 The effect of reaction temperature.....	23
2.6 Approaches to coke suppression.....	23

<b>2.7 Methods of catalyst preparation.....</b>	<b>26</b>
<b>2.8 Catalyst Regeneration and Component Recovery.....</b>	<b>28</b>
<b>2.9 Applications of CNFs and CNTs.....</b>	<b>29</b>
<b>2.10 References.....</b>	<b>32</b>

## **CHAPTER 3 EXPERIMENTAL**

<b>3.0 Introduction.....</b>	<b>36</b>
<b>3.1 Catalyst Preparation.....</b>	<b>37</b>
<b>3.1.1 Inductively Coupled Plasma -Atomic Emission Spectroscopy (ICP-AES).....</b>	<b>37</b>
<b>3.1.2 Nitrogen Physisorption.....</b>	<b>37</b>
<b>3.1.3 X-Ray Diffraction (XRD).....</b>	<b>38</b>
<b>3.1.4 Temperature Programmed Reduction (TPR).....</b>	<b>38</b>
<b>3.1.5 H<sub>2</sub> Chemisorption and O<sub>2</sub> Titration Analysis.....</b>	<b>39</b>
<b>3.1.6 Vibrational Spectroscopy.....</b>	<b>40</b>
<b>3.1.6.1 Infrared Spectroscopy (IR).....</b>	<b>40</b>
<b>3.2 Catalytic Activity and Characterisation of coke.....</b>	<b>41</b>
<b>3.2.1 Methane Decomposition Experimental.....</b>	<b>41</b>
<b>3.2.2 Gas Chromatography (GC).....</b>	<b>42</b>
<b>3.2.3 Carbon, Hydrogen, Sulphur and Nitrogen Analysis (CHNS).....</b>	<b>43</b>
<b>3.2.4 Electron Microscopy (EM).....</b>	<b>44</b>
<b>3.2.4.1 Conventional Transmission Electron Microscopy (CTEM).....</b>	<b>45</b>
<b>3.2.4.2 Analytical EM - Energy Dispersive X-ray Analysis (EDX).....</b>	<b>45</b>
<b>3.2.5 Raman Spectroscopy.....</b>	<b>45</b>
<b>3.2.6 Thermogravimetric Analysis (TGA).....</b>	<b>46</b>
<b>3.3 Spent Catalyst Component Recovery.....</b>	<b>46</b>
<b>3.4 References.....</b>	<b>48</b>

## **CHAPTER 4 RESULTS AND DISCUSSION**

<b>4.0 Introduction.....</b>	<b>49</b>
<b>4.1 Catalyst Characterization.....</b>	<b>49</b>

4.1.1 Inductively Coupled Plasma -Atomic Emission Spectroscopy (ICP-AES) analysis.....	49
4.1.2 Physico-chemical Properties of the 20%Ni/SiO <sub>2</sub> catalysts.....	50
4.1.3 X-Ray Diffraction analysis (XRD).....	52
4.1.4 Temperature Programmed Reduction (TPR).....	53
4.2 Catalytic Activity and Characterisation of Coke.....	54
4.2.1 Methane Conversion.....	55
4.2.2 The Effect of Temperature on Methane Decomposition.....	56
4.2.3 Effect of MgO in 20%Ni/SiO <sub>2</sub> on carbon yield.....	58
4.2.4 TEM analysis.....	61
4.2.5 BET analysis.....	70
4.2.6 The Effect of MgO-modified 20%Ni/SiO <sub>2</sub> on methane decomposition.....	71
4.2.7 Raman Spectroscopy.....	73
4.2.8 Thermogravimetric Analysis (TGA).....	78
4.2.9 Infrared Spectroscopy (FTIR).....	80
4.3 Spent Catalyst Component Recovery.....	81
4.4 References.....	87

## CHAPTER 5 CONCLUSION AND RECOMMENDATIONS

5.0 Conclusion.....	90
5.1 Recommendations.....	93

# CHAPTER 1 INTRODUCTION

## 1.0 Introduction

The ecological problem of global warming has led experts to assert that capitalism has reached its natural limit. This is because of capitalism's reliance on fossil fuel. Globally, fossil fuels are the main source of energy yet their reserves are estimated to be exhausted by 2040 [1]. Fossil fuel combustion is one of the greatest emitters of carbon dioxide (CO<sub>2</sub>), a greenhouse gas linked to global warming. Other greenhouse gases responsible for increased global warming are methane (CH<sub>4</sub>) and oxides of nitrogen (NO<sub>x</sub>) [2]. Global warming is a phenomenon causing frequent flooding, arid regions and climate change [3]. Ascending levels of CO<sub>2</sub>, CH<sub>4</sub> and NO<sub>x</sub> are largely as a result of the expansion of agriculture and industry, reflecting a rapid rise in the world population [4].

As early as the 1970, measures to ensure that energy security has been replaced by concerns over renewable energy sources. Renewable energy is energy from natural resources that can naturally replenished without depletion of the resources. Examples of these resources include: hydroelectricity, gas from sewage, landfills and waste, solar energy, biofuels, geothermal energy and wave power [5]. By early 2006, climate experts had estimated that the global atmospheric capacity to absorb greenhouse gases had reached its limit beyond which, any increase will inevitably cause irreversible climate change [5]. For this reason hydrogen, the most abundant, and energy efficient element in the atmosphere was posed as a lucrative source of energy [3].

Hydrogen has intrinsic advantages over methane or gasoline in that, it generates sufficient energy for electricity generation and has an environmentally benign combustion product [7]. The challenges/ disadvantages to H<sub>2</sub> usage are that conventional

approaches to H<sub>2</sub> production from hydrocarbons emit huge quantities of CO<sub>2</sub> into the atmosphere [8]. The H<sub>2</sub> production processes include steam reforming of methane **(1.1)**, partial oxidation of heavy oil, coal gasification, thermo-chemical water decomposition and water [9]. Although H<sub>2</sub> production by water electrolysis and steam reforming are important industrial processes, steam reforming of natural gas has so far been the most economic near-term process;



## 1.1 Project Justification

Owing to its high H:C ratio, Ni catalysed direct decomposition of methane at moderate temperatures **(1.2)** is considered a better alternative to “CO<sub>x</sub>-free” H<sub>2</sub> production with minimum NO<sub>x</sub> emissions [11] One such example is that reported by Italiano *et al.* [12].



Italiano *et al* [12] reported a massive production of coke as a by-product of the reaction but with a deactivation of the catalyst. The coke generated during the hydrogen production was not fully characterized as the main interest was on hydrogen production. The spent catalysts were regenerated through combustion of the coke. However oxidative regeneration of metal catalysts in the direct catalytic decomposition of methane for hydrogen production may contribute to CO<sub>x</sub> contamination of hydrogen in the production stream. Further gas purification would then be required [13].

The discovery of some novel properties possessed by the deposited coke, in the form of carbon nanofilaments, has triggered intense research into further studies on the process. Examples of novel properties of the carbon nanofilaments include: high surface area, electrical conductivity [7], porosity and high tensile strength [14]. Carbon nano filaments have found their way into industrial applications such as: polymer and elastomer fillers, commercial hydrogen storage systems, radiowave-absorbing composites, lithium battery electrodes, construction composites, oil additives, gas-distribution layers for fuel cells, filters and absorbents [14]. However carbon nano-filaments have limitations to their use because of difficulties with the separation of the metal and the carbon [12].

Nickel has a good carbon carrying capacity and is more efficient in methane decomposition at moderate temperatures than Fe and Co [15]. The price of nickel is highest among common non-ferrous metals and the incentives for recovering and recycling nickel effectively at all stages of the fabrication and use cycle are also very strong. Nickel can be acid leached from carbon and be used for electroplating purposes [16]. However, according to IUPAC, the acceptable regeneration activity is 90% of the original activity [17]. Owing to growing environmental concerns associated with CO<sub>2</sub> emissions [4] and nickel disposal implications [16], there is a need to devise methods of utilizing the coke [14], and simultaneously retaining Ni catalyst activity for other possible uses [18], to economically sustain the industrial process.

Italiano *et al* used a series of MgO-modified 20%Ni/SiO<sub>2</sub> catalysts in the form of thin layer plates with no pressure drop in the reactor [12]. The MgO-modified 20% Ni/SiO<sub>2</sub> catalyst with Mg<sub>at</sub>/Ni<sub>at</sub> ratio of 0.5 gave the best carbon capacity (C/Ni index) at a temperature range of 500-600 °C . In the present study, a similar catalyst formulation was adopted for MgO-modified 20%Ni/SiO<sub>2</sub> catalysts for methane decomposition. The promotional effects of MgO on 20%Ni/SiO<sub>2</sub> catalyst and the characteristics of the coke deposited during the methane decomposition were investigated. Catalyst preparation and

reaction conditions were adopted from the work by Italiano *et al* [11] with some modifications where necessary.

## 1.2 Aims of the project

The overall aim of the study was to investigate the relationship between the physico-chemical properties of the 20%Ni/SiO<sub>2</sub> conventional catalysts and the nature of coke deposited on the Ni based catalyst for methane decomposition. The project was undertaken with the objectives listed below in mind.

1. To synthesize a series of MgO-modified 20%Ni/SiO<sub>2</sub> catalysts with a  $Mg_{at}/Ni_{at}$  ratio in the range 0.1-2.2 by the co-impregnation method.
2. To study the characteristics of the coke obtained from methane decomposition over the MgO-modified 20%Ni/SiO<sub>2</sub> catalysts and determine the mechanism of catalyst deactivation, by analysing the catalyst after exposure to methane at moderate temperatures (500-800 °C).
3. To monitor the activity of the MgO modified Ni/SiO<sub>2</sub> catalysts and the composition of the coke obtained at the optimum methane decomposition temperature.
4. In an initial manner; recover the coke and Ni from spent Ni/SiO<sub>2</sub> catalysts for other possible applications.

### 1.3 Outline of the dissertation

The dissertation of 5 chapters covers aspects related to the study of 20%Ni/SiO<sub>2</sub> based catalytic decomposition of methane and coke characterisation.

Chapter 2 contains the literature review section of the dissertation. A brief discussion on issues related to energy production and the contribution of CO<sub>2</sub> and methane to global warming is given. The chapter also reviews the preparation of Ni -based catalysts for direct methane decomposition as well as the possible uses of recovered carbon and Ni.

Chapter 3 serves as the experimental section of the dissertation. A description of the various characterisation techniques used to study the promotional effects of MgO on 20%Ni/SiO<sub>2</sub> and the coke deposited during the methane decomposition is given.

Chapter 4 provides and discusses the results obtained in the preliminary study of the promotional effects of MgO on 20% Ni/SiO<sub>2</sub> catalysts and the characteristics of the coke deposited during the methane decomposition for CO<sub>x</sub>-free H<sub>2</sub> production. The results show the physico-chemical effects of the Ni-based catalysts on methane decomposition and the nature of the coke.

Chapter 5 presents the overall conclusion of the study, research deliverables and recommendations for future research.

## 1.4 References

1. R. Dahlberg, *Int. J. Hydrogen Energy*, 7 (1982) 121-142
2. [http://www.eoearth.org/article/greenhouse\\_gas](http://www.eoearth.org/article/greenhouse_gas) 2009/08/12
3. L. K. Fenton, P. E. Geissler, R. M. Haberle, *Nature*, 446 (2007)
4. C. Ponting, “*A New Green History of The World. London*”, Vintage Books (2006), 385- 387
5. B. Harriss-White, E. Harris, “*Unsustainable Capitalism: The Politics of Renewable Energy in the UK*”, in *Socialist Register*, New Delhi: Leftwardbooks (2007) 72-74
6. S. Lin, Y. Suzuki, H. Hatano, M. Oya, M. Harada, *J. South African Inst. Mining and Metall.*, (2001)53-60
7. D. Sebastian, I. Suelves, M.J. Lazaro, R. Moliner, *J. Power Sources*, 192 (2009) 51-56
8. Y. Pan, Z-X. Wang, T. Kan, X-F. Zhu, Q-X. Li, *Chin. J. Chem. Phys.* 19, (2006) 190-193
9. M. A. Rosen, D. S. Scott, *Int. J. Hydrogen Energy*, 23 (1989) 653-659
10. A. Kazim, “*Hydrogen Materials Science & Chemistry of Carbon Nanomaterials*” Vol 172, Springer Netherlands (2005) 467-472
11. J. R B. Mota, E. Saatdjian, D. Tondeur, A.E. Rodrigues, *Adsorption*, 1(1995) 1-27
12. G. Italiano, C. Espro, F. Arena, F. Frusteri, A. Parmaliana, *Catal. Lett.*, 124 (2008) 7-12
13. <http://en.wikipedia.org/wiki/carbon> 2010/01/05
14. [http://nanotechnology.e-spaces.com/carbon\\_nanofibers.html](http://nanotechnology.e-spaces.com/carbon_nanofibers.html). 2010/01/05
15. S.P. Chai, S.H.S. Zein, A.R. Mohamed,” *A Review On Carbon Nanotubes Production Via Catalytic Methane Decomposition*”, 1<sup>st</sup> National Postgraduate Colloquim , School Of Chemical Engineering University of Sains Malaysia, Seri Ampangan (2004) 60-69
16. [http://www.nickelinstitute.org/index.cfm/ci\\_id/6561/la\\_id/1.htm](http://www.nickelinstitute.org/index.cfm/ci_id/6561/la_id/1.htm) 2009/12/18

17. J. Haber, J. H. Block, B. Delmon, *Pure & Appl. Chem.*, 67(1995)1257-1306
18. K. R. Vuyyuru, K. K. Pant, V. V. Krishnan, K. D. P. Nigam, *Ind. Eng. Chem. Res.*, 5 (2010) 2014–2024

## CHAPTER 2 LITERATURE REVIEW

### 2.0 Introduction

The increase in global pollution has raised environmental awareness with regards to energy usage, CO<sub>2</sub> emission, catalyst regeneration and disposal. This has called for reviews and new approaches to undertake industrial processes.

This chapter discusses the rationale for South Africa's interest in hydrogen, fuel-cell, carbon capture and storage technologies as well as issues related to energy and hydrogen production, including the use of catalysts in methane decomposition, catalyst deactivation and regeneration. The use and possible applications of carbon and spent catalyst from methane decomposition, citing recent research, will also be covered.

### 2.1 Background

Currently, approximately 89% of South Africa energy is derived from fossil fuel with CO<sub>2</sub> emissions of about 400 million tons a year representing 1% of total emissions on a global scale [1]. Removing CO<sub>2</sub> produced from fossil fuels through a process called carbon capture and storage (CCS) is now a South African national research priority. The initiative aims to address global climate change and clean coal technologies by stabilising CO<sub>2</sub> emissions between 2020 and 2025 [1]. **Figure2. 1** illustrates estimated world carbon dioxide emissions. It can be observed

from the **Figure 2.1**, that the imbalance in the global atmospheric capacity to absorb CO<sub>2</sub> as a greenhouse gas to the present political economy cannot be over emphasised.

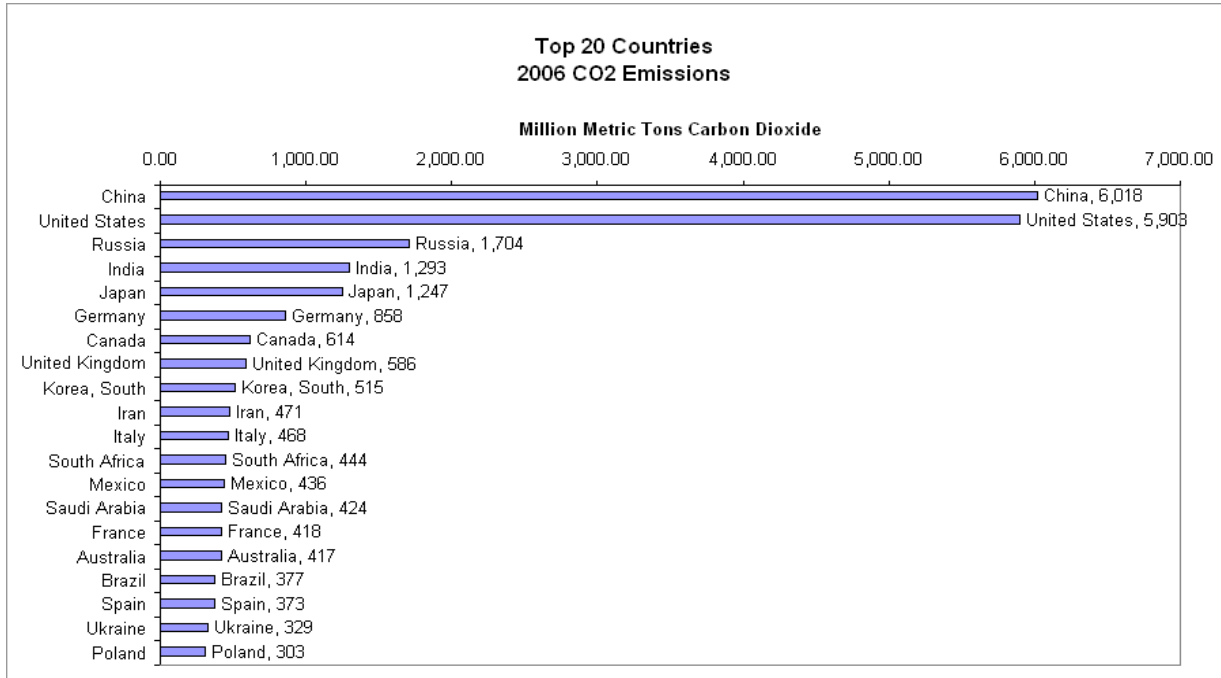


**Figure2.1** An illustration of estimated global carbon dioxide emissions [2].

Although CO<sub>2</sub> contributes about 77.6% of the earth's global warming potential [3], methane is 20 times more effective in absorbing infrared radiation than CO<sub>2</sub> as a greenhouse gas in the atmosphere [4]. Methane in its minute levels contributes about 20% of the overall additional greenhouse effect [4]. According to data from the Intergovernmental Panel on Climate Change (IPCC) in 2007, human activities such as animal husbandry, rice cultivation, biomass burning and waste management reflect about 60% of the global methane emissions [5]. Another contributor is nitrous oxide, produced from vehicle engine exhausts and nitrate fertilisers [6].

In view of the energy and environmental crises, methane is an underutilized resource to liquid fuels and non toxic energy carriers like hydrogen that can replace the rapidly exhausting crude

oil reserves [7]. Currently, methane is used for electricity generation, domestic and industrial heating. Figure 2.2 illustrates the geographical distribution of proven natural gas reserves [8]. The major challenge in the utilisation of methane is the transportation of the gas from the reserves to the potential industry through pipelines. This would be expensive [9].

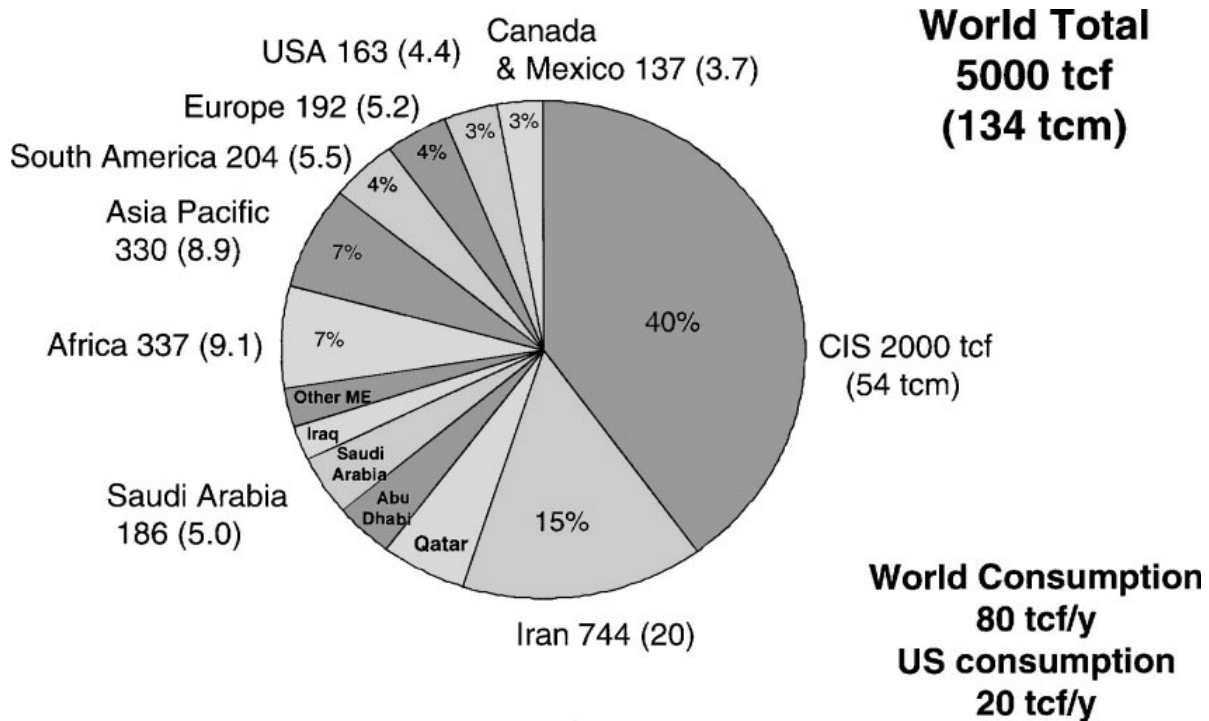


**Figure 2.2** Geographical distribution of proven natural gas reserves [8]

Methane is a primary component of natural gas (95%) and has the highest H:C ratio amongst the hydrocarbons, which makes its direct decomposition a lucrative source of hydrogen with minimum CO<sub>x</sub> and NO<sub>x</sub> emissions [10]. The carbon produced from methane decomposition is very pure as it is easy to separate from the product hydrogen [11]. Furthermore, the process simultaneously removes methane from the atmosphere. Besides hydrogen, filamentous carbon is formed by direct decomposition of methane [12]. The carbon nanofilaments; carbon nanotubes (CNTs) and carbon nanofilaments (CNFs) have novel properties such as high surface area and high electrical conductivity and they can be employed as an electrocatalyst support in hydrogen fuel cell systems [12].

Carbon nanotubes and carbon nanofilaments have not been used in direct carbon fuel cells. A Direct Carbon Fuel Cell (DCFC) is a fuel cell that utilizes a carbon source such as coal, coke, char or a nonfossilized source of carbon as a fuel. Although the combustion of the carbon and oxygen emits carbon dioxide as a by-product, the direct fuel cell is twice as efficient (~70%) as the conventional combustion reaction [13]. The overall reaction of the cell is:



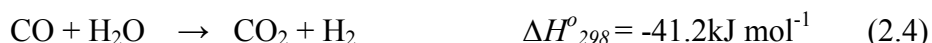
The high thermal stability of methane is a challenge to using methane as a source of hydrogen. Non-catalytic decomposition of methane is not economically viable as effective methane decomposition occurs at temperatures  $>1200$  °C [3]. An estimated 440 kJ/mol is required to break the strong  $\text{sp}^3$  hybridized C-H bonds [3].



Hydrogen as a major energy source possesses intrinsic advantages over fossil fuels in that it has a non-polluting by product, water and is abundant in nature, and is an efficient energy carrier that can be used in fuel cell systems [14]. Furthermore the mixture of hydrogen and unreacted methane is a more effective fuel for internal combustion engines and gas turbine power plants than natural gas [15]. The use of hydrogen can be used not only as a source of fuel, but can be used as a reactant in chemical processing, electronics, food processing, and metal manufacturing [16]. Apart from electrolysis, the challenges to  $\text{H}_2$  usage are that conventional approaches to  $\text{H}_2$  production are major sources of CO and  $\text{CO}_2$  emissions into the atmosphere [17]. Furthermore, CO and  $\text{CO}_2$  in  $\text{H}_2$  streams are difficult to separate [18]. Amongst the conventional processes of hydrogen production mentioned in Chapter One, steam reforming of natural gas has so far been the most economic near-term process [3]:



The above reaction is reversible and additional hydrogen together with CO<sub>2</sub> can be recovered by the WGS (water gas shift) reaction at high temperatures produced: [19]



Furthermore, steam reforming often generates some CO. The CO contamination of the hydrogen, even in small concentrations, is undesirable especially where the hydrogen is to be used in fuel cells equipped with platinum electrodes [15]. The CO poisons the platinum electrodes used in the proton exchange membrane (PEM) fuel cells [20].

## 2.2 The Effect of Metals in Catalytic Methane Decomposition

Metal-catalysed direct decomposition of methane is of most practical importance to curb climate change and sustain economic development. Among the metals of the iron subgroup (Fe, Co, Ni), supported Ni exhibits the best catalytic function for methane decomposition from temperatures as low as (450-500) °C [21]. Co and Fe exhibit lower activity and lower carbon capacity in methane decomposition than Ni on similar supports under the same reaction conditions [22]. Generally Ni catalysts produce filamentous carbon [23]. Furthermore, Co is expensive and toxic. Hu *et al* produced 90 % purity SWNTs over Co/MgO catalyst at 1273 °C while Colomer *et al* obtained 70-80 % pure SWNTs at 100 °C using Co/MgO [24]. Iron on the other hand is non toxic and resistant to high temperature deactivation [15]. Fe/Al<sub>2</sub>O<sub>3</sub> catalysts are very efficient in carbon deposition at a temperature range of 600-650 °C, [25].

The addition of the right promoter to produce a bimetallic catalyst, may improve the carbon capacity, influence the type and morphology of carbon and catalyst lifetime. Reshetenko *et al* discovered that introducing Cu into Ni/Al<sub>2</sub>O<sub>3</sub> improves carbon capacity from 22.4g<sub>c</sub>/g<sub>cat</sub> to 525 g<sub>c</sub>/g<sub>cat</sub> and prolongs the catalyst lifetime from 2 h to 54 h at 625 °C [26]. Lu *et al* reported the absence of amorphous carbon in CNTs obtained over Fe/Mo/Al<sub>2</sub>O<sub>3</sub> [27].

The highest carbon capacity of 1170 g<sub>c</sub>/g<sub>cat</sub> on the palladium promoted Ni/SiO<sub>2</sub> bimetallic system was reported by Takenaka *et al* [28]. Italiano *et al* reported a carbon capacity index (C/Ni, number of CH<sub>4</sub> molecules converted per Ni atom until complete catalyst deactivation) of about 170 at 600 °C in catalysts with an atomic ratio of Mg<sub>at</sub>/Ni<sub>at</sub> as 0.5 in MgO-modified 20% Ni/SiO<sub>2</sub>/ silica cloth than bare 20% Ni/SiO<sub>2</sub>/ silica cloth in the direct decomposition of methane [29].

### **2.3 The effect of support in the catalytic methane decomposition**

It is generally accepted that the most important factors influencing carbon deposition during metal catalyzed methane decomposition are the particle size, dispersion and stabilization of the metallic catalyst particles, which are strongly influenced by the nature of metal-support interactions [30]. There are no typical strong metal-support interactions (SMSI) with Ni/SiO<sub>2</sub> catalysts. In addition, silica, compared to other supports, usually ensures a better dispersion of nickel, regardless of the method of preparation [31].

Interaction of components in the catalyst greatly affects catalytic properties differently even if Ni particle sizes are similar. Carbon yield over a Ni catalyst on Al<sub>2</sub>O<sub>3</sub>, ZrO<sub>2</sub>, MgO and TiO<sub>2</sub> have been reported to be lower than on a SiO<sub>2</sub> despite similar [15] particle size, although the yield of carbon is possibly related to the average size of the nickel particles on the fresh catalysts [32].

Nickel particle with diameters in the range of 60-100 nm have been observed to have the longest catalytic lifetime for methane decomposition and maximum carbon yield [11]. Takenaka *et al* studied the catalytic activities and lifetimes of Ni supported on different supports and they reported that Ni catalysts supported on SiO<sub>2</sub>, TiO<sub>2</sub> and graphite showed high activities and long lifetimes for methane decomposition, whereas the catalysts supported on Al<sub>2</sub>O<sub>3</sub>, MgO and SiO<sub>2</sub>/MgO were inactive for the reaction [11].

As mentioned before, Ni catalysts produce filamentous carbon [23] but an abnormality is observed with Ni supported on the H-ZSM-5 zeolite. The combination of Ni/H-ZSM5 does not produce filamentous carbon [23]. Nickel particles larger than 100 nm in size are incapable of producing filaments, since graphitic carbon isolates them from the reaction medium. Thus, carbon nanotubes with diameters exceeding 100 nm are unstable and rarely grown [11, 22].

Although MgO as a catalyst support has advantages over Al<sub>2</sub>O<sub>3</sub> and SiO<sub>2</sub> in that MgO can be acid-leached to separate it from carbon nanofilaments, MgO supported metals display low catalytic activity towards methane decomposition. However MgO supported Ni catalysts has been used effectively in the CO<sub>2</sub> reforming of methane. Zirconia-supported Ni has been reported to show a lower methane conversion, lower carbon capacity and higher deactivation rate [11].

Silica has been reported to be the most complementary support for methane decomposition, although the Ni/SiO<sub>2</sub> systems can sinter to sizes larger than 150 nm, which are catalytically inactive for methane decomposition [11]. This result could be due to poor metal-support interactions between the Ni and the SiO<sub>2</sub> support. Methane decomposition over Ni/SiO<sub>2</sub> catalysts occurs at a minimum temperature of 450 °C with highest activity at moderate temperatures of 500-600 °C [11]. Italiano *et al* studied methane decomposition using MgO-modified 20%Ni/SiO<sub>2</sub>/silica cloth thin layer catalysts in the range 450-600 °C and reported the highest carbon capacity and H<sub>2</sub> productivity when compared to unmodified 20%Ni/SiO<sub>2</sub> at 600 °C [29].

The longest catalyst lifetime of a single catalyst system (70 h) has been displayed by a 40%Ni/SiO<sub>2</sub> at 500 °C. At temperatures higher than 650 °C, silica supported catalysts cannot decompose methane efficiently. Titania supported nickel on the other hand, has the lowest methane activation energy (~ 60 kJ/mol) over 13% wt Ni/TiO<sub>2</sub>. Methane conversions of up to 92% have been achieved with Ni/TiO<sub>2</sub> at 900 °C without rapid deactivation. Furthermore, catalytic activity in Ni/TiO<sub>2</sub> is superior to that of Ni/SiO<sub>2</sub> in that methane decomposition is kept high with successive regeneration cycles as the metal particle size approaches the optimum size for methane decomposition (60-100 nm) [11].

As discussed above, Ni-based catalysts have optimum catalytic activity at moderate temperatures of 600 °C. At 600 °C, methane conversion is thermodynamically limited such that hydrogen streams (H<sub>2</sub>>60%) cannot be attained using a nickel based catalyst. Takenaka *et al* reported that at a temperature of 500 °C a typical 40% Ni/SiO<sub>2</sub> catalyst with a nickel particle size of 60-100 nm achieved a carbon capacity of 491 g<sub>C</sub>/g<sub>Ni</sub>. Furthermore, Ermakova *et al* reported that at 550 °C, 90% Ni/SiO<sub>2</sub> catalyst with nickel particles in the range 10-40 nm size had a carbon carrying capacity of 385 g<sub>C</sub>/g<sub>Ni</sub>, while other supports such as TiO<sub>2</sub>, MgO, ZrO<sub>2</sub> and Al<sub>2</sub>O<sub>3</sub> gave relatively lower carbon yields [30].

Nickel particles with diameters in the range of 60-100 nm have the longest catalytic lifetime for methane decomposition and the maximum yield being observed in the range of 20-60 nm [11]. Nickel supported on titania on the other hand, has the lowest methane activation energy of 60 kJ/mol over 13% wt Ni/TiO<sub>2</sub>. Methane conversions of up to 92% have been achieved with Ni/TiO<sub>2</sub> at 900 °C without rapid deactivation. Moreover, catalytic activity in Ni/TiO<sub>2</sub> is superior to Ni/SiO<sub>2</sub> in that methane decomposition is kept high with successive regeneration cycles as the metal particle size approaches the optimum size for methane decomposition (60-100 nm). Ni/SiO<sub>2</sub> systems sinter to sizes larger than 150 nm, which are catalytically inactive for methane decomposition [11].

The deactivation of a catalyst is greatly influenced by the mode of growth of the carbon which is directly related to the metal-support interaction (MSI). Hernadi *et al* have reported that the catalyst support exerts effects on both the production of hydrogen and carbon [33]. Pease *et al* proposed that there NiO-SiO<sub>2</sub> interactions that are induced by the formation of SiO<sub>4</sub> groups in the lattice of the NiO crystal at temperatures as low as 550 °C [34]. The formation of silicates may hinder Ni particle reconstruction, sintering and fragmentation of faces which are necessary for growth of filamentous carbon [35].

Catalysts with strong metal-support interaction (SMSI) favour base growth carbon formation over tip growth formation [29]. Small Ni particles with SMSI also prevent carbon nucleation on the rear side of the Ni particle hindering growth of carbon filaments [11, 29]. Strong metal support interaction can exist between easily reducible metal oxides and transition metals in the presence of hydrogen [36]. Essentially, a less porous support with a large surface area provides more surface sites for anchoring the catalyst precursor, resulting in better catalyst dispersion [11].

## 2.4 Catalyst Deactivation

Like any catalyzed process, catalyst deactivation however, is the major hindrance to the methane decomposition process. Postulated factors contributing to catalyst deactivation in hydrocarbon processing include coke formation, sulphur poisoning, thermal sintering and attrition, physical attrition and volatilization of active component. Chief among the catalyst deactivation factors in industrial processes is coke formation [37]. **Figure 2.3** shows some of the deactivation mechanisms.

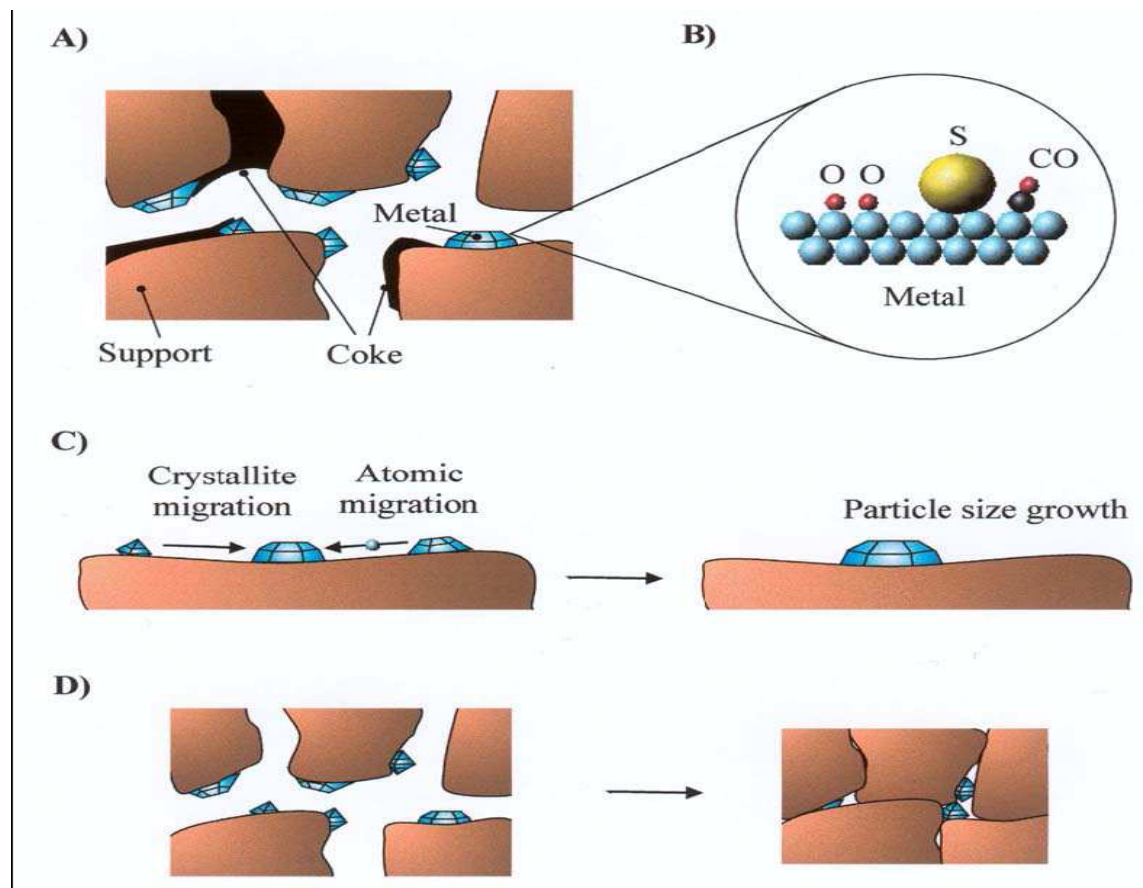


**Figure 2.3** Deactivation mechanisms: (A) coke formation, (B) poisoning, (C) sintering of active metal particles and (D) sintering and solid-solid phase transitions and encapsulation of active metal particles [38]

### 2.4.1 Coke Deposition/ Formation

Coke may be defined as an unwanted by-product formed by the polymerisation and dehydrogenation (condensation) of organic molecules present in the feed or formed as product, adsorbed on the surface of solid catalysts during organic catalytic reaction [23]. It may consist of a large number of aromatic components with hydrogen deficient carbonaceous material [39]. It is a question of taste whether this is referred to as coke or carbon, although the latter term is most

often used. Carbon deposition is usually the main cause of catalyst deactivation as the carbon blocks the active sites of the catalyst [40].

Depending on the conditions (temperature, partial pressures of reactants and products), different morphologies of coke may exist, that is: pyrolytic carbon, encapsulating carbon, whisker and carbides. However the nature and morphology depends on the active metal, metal particle size, and hydrocarbon source and reaction temperature [29]. At high temperatures poly-aromatic or even graphitic compounds that deactivate the catalyst are formed. Coke formation may block the active nickel sites [15]. The coke accumulation may cause pressure drops which lead to nonisothermal conditions in reactors. Loss of catalytic activity may also occur through pore blockage, encapsulation of the metal crystal, or collapse of the catalyst support [29].

As mentioned before, the deactivation of a catalyst is greatly influenced by the mode of growth of the carbon which is directly related to the metal-support interaction (MSI) [41]. Catalyst deactivation caused by carbon deposition depends on the amount, type and location of carbonaceous species formed. The reactivity of coke deposits towards gasification is primarily determined by the structure, which in turn depends on the mechanisms of carbon formation [23]. Generally, Ni catalysts have been reported to give long filamentous carbon nanofilaments at relatively low methane decomposition rates, low operating temperatures and long residence time [42]. This filamentous carbon can be in the form of CNTs and CNFs [11]. The carbon nanofilaments with increasing time on stream become the support of the Ni catalyst particle in a tip-based mode of growth, prolonging the catalyst life time. Breakage of the carbon nanofilaments may lead to loss of catalyst particle exposure [29].

## 2.4.2 Sintering and Attrition

Sintering describes a strongly temperature dependent process in heterogeneous catalysts, where small catalytically active particles grow in size. However, a reduction in total surface energy is the main driving force of sintering. The rate of nickel particle sintering also depends on **the** atmosphere over the catalyst. Two mechanisms for sintering have been proposed: (i) particle migration over the support followed by coalescence, (ii) metal transport species emitted from one crystallite, migrate over the support or via the gas phase and are captured by another crystallite [43].

The sintering mechanism is directly related to the melting temperature and is defined by the so-called Hüttig and Tamman temperatures which indicate the temperature at which sintering starts. The semi-empirical relations for the Huttig and Tamman temperatures are defined in equations 2.7 and 2.8 respectively [37]. When the low Huttig temperature is reached, atoms at defects become mobile. While upon reaching the Tamman temperature, atoms from the bulk will exhibit mobility, and at the melting temperature, the mobility will be so high that liquid-phase behaviour is observed.

$$T_{\text{Huttig}} = 0.3T_{\text{melting}} \quad (2.7)$$

$$T_{\text{Tamman}} = 0.5T_{\text{melting}} \quad (2.8)$$

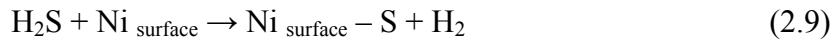
where  $T_{\text{melting}}$  is the melting point of Ni, is equivalent to 1453 °C [44].

It has been proposed that the increased rates of sintering at temperatures above 600 °C are due to a change in sintering mechanism from particle migration to atom migration. Sintering in an H<sub>2</sub>/H<sub>2</sub>O atmosphere at temperatures above approximately 600 °C is accelerated. However, at 600°C particle migration dominates [43]. During transport and loading of the catalyst in the reactor catalyst particles may experience strong stresses in their life cycle: during start up heating and during cooling down. During catalyst regeneration, the expansion and contraction of the

reactor mechanical degradation through catalyst break-down may occur. This mechanical degradation is known as attrition [37].

### 2.4.3 Sulphur Poisoning

Hydrocarbon feeds usually contain sulfur compounds that can be converted into hydrogen sulfide under reaction conditions. The sulfur atom in the hydrogen sulfide adsorbs irreversibly at the active nickel site:



Thus, the maximum sulphur poison capacity for the nickel catalysts is related to the nickel surface area and the shape of the catalyst pellet. On a weight basis, 440 ppm S per  $\text{m}^2\text{g}^{-1}$  of metallic nickel can adsorb irreversibly. Sulphur poisoning has also been related to the extent of sintering in steam reforming. Sulphur poisoned catalysts are usually inactive at temperatures below 700 °C [43].

### 2.5 Mechanism of Coke formation

The catalytic decomposition of methane can be referred as a catalytic chemical vapour deposition of volatile carbon to solid non-volatile carbon product. The formation of coke includes several steps [45];

- (i) adsorption and decomposition of methane molecule at the nickel surface,

- (ii) dissolution and diffusion of carbon through the metal particle,
- (iii) surface diffusion of carbon species, and
- (iv) precipitation of the carbon species at the rear/ top face of the metal particle.

Generally it has been accepted that bulk or surface diffusion of carbon in the nickel particles is the main pathway for carbon transport and that the driving force for carbon diffusion could be the temperature gradient through the metal particle and the carbon concentration gradient [45].

Carbon nanofilaments have an external diameter between a few nanometers to about one hundred nanometers. Carbon nanofilaments exceeding 100 nm diameters are rarely grown [11]. CNFs and CNTs differ in the arrangements of graphite sheets. The main difference in the two carbon nanofilaments is that CNFs lack a hollow cavity. CNFs are formed by graphite sheets at a determined angle with respect to the growth axis. In single walled carbon nanotubes, SWNT, a hollow is created by a single sheet of graphite while in multi-walled carbon nanotubes (MWNTs) the hollow is formed by several concentric sheets with increasing diameter. Temperature, carbon source and the presence of hydrogen may also determine the morphology and properties of the carbon nanofilaments [12]. Figure 2.3 shows a schematic illustration of the mechanism of CNT formation.

A tip-growth and a base growth mechanism for CNT growth has been proposed. These growth mechanisms are based on the locations of the active metallic particles. The growth model manifested depends on the strength of the metal-support interactions. For catalysts with weak MSI, the catalytic particle is easily detached from the anchoring support during CNT growth, thus tip growth dominates. CNTs/CNFs grown on catalysts with SMSI are subject to base a growth mechanism [11, 29].

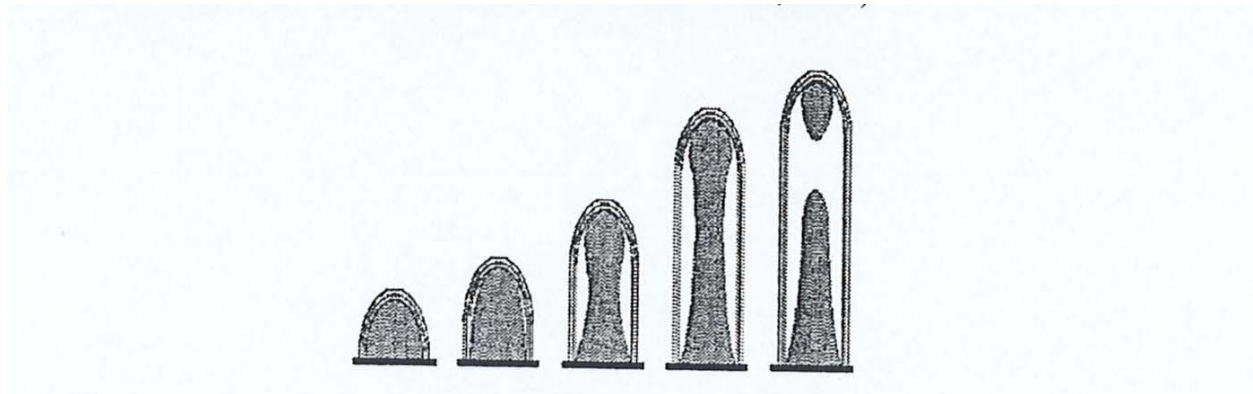


**Figure 2.4** An illustration of growth process of the CNTs [11].

Apart from the influence of temperature carbon diffusion depends on several factors such as (i) the thickness of the particle; (ii) metal surface area; (iii) concentration of carbon at the metal-gas interface; and (iv) concentration of carbon at the metal-support interface. Chen *et al* found that the size of the nickel crystal had an influence on both the coking rate and the initiation or nucleation of carbon nanofilaments from methane decomposition. Small nickel particles are poor carbon nucleation centres as the short length for effective carbon diffusion saturates the concentration of carbon, lowering the driving force for carbon diffusion and carbon diffusion rate. The low driving force of diffusion results in fast catalyst deactivation. Thus, the carbon on the Ni surface polymerises and encapsulates the active Ni particle isolating it from the methane gas [46]. On large Ni particles the carbon diffusion is lower than the surface carbon formation rate so coke accumulates on the metal surface blocking the Ni active sites [29]. It is supposed that there is a critical methane partial pressure that corresponds to the diffusion rate of carbon atoms in the catalyst. At a methane partial pressure higher than the critical value, catalytic methane decomposition is constant, independent of the methane partial pressure at a given temperature [47].

### **2.5.1 The effect of reaction temperature**

The major concern in reaction temperature selection is to produce effective methane conversion with good carbon carrying capacity. As mentioned before, methane decomposition with Ni/SiO<sub>2</sub> catalysts occurs at a minimum temperature of 450 °C with optimum catalytic activity at moderate temperatures as low as 500-600 °C. Reaction temperature has a strong influence because at temperatures higher than 650 °C, decomposition of methane over Ni/SiO<sub>2</sub> catalysts is not efficient. Although at temperatures above 650 °C methane decomposition over Ni/SiO<sub>2</sub> is not efficient, MWNTs formation is favorable at 700 °C whilst CNFs are formed at temperatures around 500 °C. Furthermore, the diameters of carbon nanofibers CNFs and CNTS decrease with temperature elevation. Carbon nanotubes produced at high temperatures have smaller interlayer distances and high crystallinity [11].

At low temperatures, the rate determining step is the rapid pre-equilibrium adsorption of methane. The rate determining step is the dissolution of surface C atoms into nickel particles. The solubility of carbon decreases with elevation of temperature leading to accumulation of carbon atoms on the surface of the catalyst as graphite layers on the surface of Ni particles [47]. The carbon accumulation on the catalyst particle is aggravated on small particles [29].

### **2.6 Approaches to coke suppression**

Heterogeneous catalysts in hydrocarbons processing have had their catalytic activity and selectivity enhanced through the incorporation of small amounts of various elements which act as promoters. The promoter may exhibit its beneficial effect in a limited concentration range.

The promoter need not be catalytically active but may directly or indirectly affect the overall catalytic performance of the active element [48, 49].

Beneficial promotional effects can be structural, electronic or synergistic. Structural promoters affect the formation, dispersion and stability of the active phase of a catalyst material. Electronic promoters affect the local electronic structure of an active metal mostly by adding or withdrawing electron density near the Fermi level in the valence band of the metal. This directly affects the chemisorption properties of the active metal and the elementary steps involved in each turnover on the catalyst [48].

Synergistic promotion effects may alter the local feed composition or may, due to its catalytic properties, influence the overall reaction production distribution. Possible synergistic promotion effects may occur through increased H<sub>2</sub>S tolerance, hydrogenation/dehydrogenation and coke burning during regeneration. A single promoter may induce several effects on the catalyst performance making it difficult to distinguish its specific effect [48].

The right catalyst promoter may improve the carbon capacity; influence the type of selectivity and morphology of carbon and lengthen the catalyst lifetime [11]. Several catalyst formulations have been made to suppress coke accumulation as the mechanism of deactivation, including addition of alkali, earth alkali elements and basic oxides like MgO and CaO as promoters [36].

Density Functional Theory (DFT) calculation studies on Ni catalysed methane reforming, undertaken by Bengaard *et al.* have revealed that carbon atoms adsorb stronger at step sites than at terrace sites. Thus the step sites are better nucleation sites for carbon. The transport of carbon proceeds via the nickel surface and the nickel-graphite interface [43]. Some researchers have suggested that hydrocarbons decompose favourably on the Ni (100) and Ni (110) faces whilst the Ni (111) and Ni (311) faces are the favourable rear faces. Therefore, it may be argued that filamentous carbon predominantly grows from the (111) and (311) steps for carbon nanofilaments which grow by the tip-growth mechanism and vice versa [50].

The DFT studies suggest that promoter or poisoning species such as potassium, sulfur, and gold are preferentially located at step sites. Sulfur and gold have been reported to be 48 and 36 kJ/mol more stable at steps than at terrace sites, while potassium as -K-O-K-O- rows along nickel steps have 75 kJ/mol more stability than at terraces [43]. Thus, the carbon suppression effect of these promoters arises through the blocking of the nickel steps fundamental for carbon nucleation sites for graphite formation. The nickel step density may depend on the nickel particle size. Van Hardeveld and van Montfoort also suggested that there is a strong decrease in the number of step sites per surface area with increasing particle size [43].

Italiano *et al* studied the influence of MgO incorporation on the catalytic performance of 20% Ni /SiO<sub>2</sub>/Silica Cloth systems in CO<sub>x</sub>-free H<sub>2</sub> production and decomposition of methane and reported improved catalyst stability to deactivation and better catalyst regeneration relative to an unmodified 20% Ni /SiO<sub>2</sub>/Silica Cloth system. Since the overall catalyst deactivation is the outcome of the competing reactions: coke deposition and coke gasification (hydrogenation in the present case), the effect of MgO on Ni based catalysts may be assumed to be the formation of easily gasifiable carbon. The high activity and stability of the MgO modified catalysts in Italiano's work can be attributed to the strong Lewis basicity of MgO on the relatively neutral silica support surface and strong metal support interaction induced by the Ni<sub>x</sub>Mg<sub>1-x</sub>O solid solution, which inhibits carbon deposition and sintering of nickel particle to catalytically inactive particles [51].

MgO has also been used as a promoter in the production of syngas (CO and H<sub>2</sub>) by CO<sub>2</sub> reforming of methane ( $\text{CH}_4 + \text{CO}_2 \rightarrow 2\text{H}_2 + 2\text{CO}$ ). The effect of MgO on the process has been favourable at a low H<sub>2</sub>/CO ratio (1: 1) and is also observed for carbon monoxide hydrogenation in Fischer Tropsch synthesis. This is because higher H<sub>2</sub>/CO ratios favours methanation and suppresses chain growth [51]. Wang *et al* reported that MgO improved CO<sub>2</sub> adsorption affinity, and depressed CO disproportionation and methane decomposition such that the catalyst deactivation was retarded [51]. To determine the reactivity of the coke obtained in CO<sub>2</sub> reforming of methane over nano-MgO supported Ni catalyst (Ni/MgO-AN), temperature programmed hydrogenation (TPH) studies were conducted. Comparative temperature programmed hydrogenation (TPH) studies of coke formed under atmospheric and high pressure

CO<sub>2</sub> reforming of methane over a Ni/MgO-AN catalyst have revealed that there are two forms of coke deposits: *alpha-C* and *beta-C*. At atmospheric pressure only coke in the *alpha-C* form is formed from the decomposition of methane on Ni catalysts while *beta-C* is formed at high pressure from the disproportionation of CO. The *beta-C* is the more stable form that usually leads to poisoning of the Ni catalysts in CO<sub>2</sub> reforming of methane [36, 51].

With reference to CO<sub>2</sub> reforming of methane, MgO reduces the electron-donor ability of metallic Ni in the activation of CO molecules, leading to efficient inhibition of the disproportionation reaction of CO [51]. Jeong *et al* found that addition of MgO to supported Ni catalysts for CO<sub>2</sub> reforming reduced the size of the Ni<sup>0</sup> metal and produced highly dispersed Ni<sup>0</sup> species, significantly suppressing carbon deposition in CO<sub>2</sub> reforming [36]. The presence of MgO in pumice supported nickel catalysts has been reported to favour the formation of C<sub>2</sub><sup>+</sup> hydrocarbons in the hydrogenation of CO [52].

Generally MgO modified Ni catalysts maintain a balance on competing reactions of deposition and gasification of coke at the surface as well as a strong resistance of the small Ni particles to sintering under the working conditions [29]. However it should be noted that the reason why Ni catalysts are usually regarded as methanation catalysts and are not used in carbon monoxide hydrogenation catalysts is that are highly selective to methane and have low selectivity to high molecular weight hydrocarbons [48]. Thus, hydrogasification of coke could lead back to methane formation.

## **2.7 Methods of catalyst preparation**

Catalyst preparation methods are crucial in achieving the desired promotional effect. The promoter elements should be added in a precise and controlled manner as they only exhibit their beneficial effect in a limited concentration range. However the catalyst preparation methods should also be applicable to large-scale industrial production of Ni-based catalysts for methane decomposition.

The most common methods of heterogeneous catalyst preparation are impregnation, ion exchange, adsorption and deposition-precipitation [53]. Ion-exchange involves replacing an ion in an electrostatic interaction with the surface of a support by another catalytically active species. In adsorption, ionic species from aqueous solution are attracted electrostatically by charged sites on a solid surface. Adsorption allows the controlled anchorage of a precursor in an aqueous solution on the support. Deposition-precipitation involves two processes: (i) precipitation from bulk solutions or from pore fluids; (ii) interaction with the support interface. Sufficient amounts of the salt and alkali are required to cause precipitation of the desired component in the pores of the support and not outside the support.

Impregnation consists of contacting a solid with a certain volume of liquid containing the components (precursor) to be deposited on the surface. The procedure is carried out with a certain volume of solution containing the precursor of the active phase that is contacted with the solid support, which, in a subsequent step, is dried to remove the imbedded solvent. Depending on the volume of solution, two methods of contact can be distinguished, namely wet impregnation and incipient wetness impregnation. In wet impregnation excess solvent is used and then removed by drying. Incipient wetness impregnation requires precise volumes of appropriate concentration of solution of the precursor to be more or less equal to the pore volume of the support. The controlling variable for both methods is temperature which influences the precursor solubility and solution viscosity. Co-impregnation involves introducing two or several active components to a support in a single step. Co-impregnation with uniform distribution and without segregation of species is extremely difficult to achieve [53]. It is generally accepted that impregnation, results in inhomogeneous distribution of the active component and low dispersion [31].

## 2.8 Catalyst Regeneration and Component Recovery

Catalyst deactivation is inevitable for most processes prompting research into the development of design and operation of commercial processes. On economic grounds, catalyst regeneration is preferred, but only when 90% of the original activity is achieved [35]. The regeneration of catalysts can only work for a while but eventually catalysts deactivate to the point of disposal [54]. The regeneration and component recovery or disposal of deactivated catalysts depends on chemical, economic and environmental factors [54]. This prompts the need to devise methods of utilizing the carbon at the same time retaining catalyst activity and to economically sustain the industrial process. A spent catalyst can also be used in another application. A summary of the possible applications of spent catalysts are shown in **Table 2.1**.

Regeneration procedures are often specific to the catalyst and the species causing deactivation. Removal of coke deposited on a catalyst is possible through: oxidation, reaction with water to form carbon monoxide and hydrogen, methanation, and the Boudouard reactions. Of these, the oxidation reaction is most efficient producing heat which results in sintering. Sensitive catalysts may be regenerated with  $H_2$ , but the rates of the reaction are slow and the process inefficient. Oxidative regeneration through steam is endothermic and more efficient. However, sintering of catalysts is accelerated by steam conditions. Thus, regeneration procedures are a compromise of good temperature-programming and steam control. Often mixtures of air and steam are used [35].

The most common approach to recover totally the metals in the catalyst is through roasting and leaching [54]. In this instance when recovery carried out on spent silica-supported Ni-based catalysts used for methane decomposition is accompanied by coke deposition. Roasting is unnecessary as it leads to undesired  $CO_2$  emissions. It is, however, possible to carry out selective leaching of the components of the spent catalyst [54]. To use a spent catalyst the soluble hydrocarbons can be removed through Soxhlet extraction [23, 55]. The remaining insoluble

component of the spent catalysts is then separated from the silica support by dissolution [23]. After the support has been removed the nickel and magnesium oxide can be acid leached from the coke and filtered [11].

## **2.9 Applications of CNFs and CNTs**

Today, carbon nanofilaments represent one of the most active research fields but have limitations to their use because of difficulties with the separation of metal and carbon without loss of catalytic activity. This major problem associated with carbon nanofilament production has led to catalyst regeneration by oxidation of carbon leading to massive CO<sub>2</sub> emissions to the atmosphere [29]. However oxidative regeneration of metal catalysts in direct catalytic decomposition of methane for hydrogen production contributes to CO<sub>x</sub> contamination of hydrogen and consequently the need for further purification steps [18]. This has increasingly led to devising methods of utilizing the carbon at the same time retaining catalyst activity, to economically sustain the industrial process. Studies on the properties and applications of as grown CNTs have been made to improve and control their properties through different functionalization methods [56, 57].

Industrial applications of the carbon nanofilaments include: polymer and elastomer fillers, commercial hydrogen storage systems, radiowave-absorbing composites, lithium battery electrodes, construction composites, oil additives, gas-distribution layers for fuel cells, filters and absorbents [58]. CNFs are used in composite materials, scanning microscopy tips, carrier material for various catalysts in petrochemistry and gene delivery [65]. CNT pores have also found their way as "nanoscale chemical reactors" and for gas storage owing to their favourable surface and porosity properties. CNTs have also displayed positive results in hydrogen fuel cells and as electrocatalyst supports due to their CO poisoning resistance [12]. CNTs have been used

as catalyst supports due to their mechanical strength [12]. In methane decomposition, the carbon based catalysts are superior to metal based catalysts in that they are available, cheap and sulphur and temperature resistant [3].

It has been reported that K and Li doping of MWNTs enhanced hydrogen storage capacities at ambient pressure and temperature [59]. The use of CNTs, especially SWNTs, has also been extended to replacing platinum electrodes in hydrogen fuel cells, owing to their resistance to CO poisoning, large surface area, porosity and low weight. Dai *et al* discovered that vertically aligned CNTs, in which some of the carbon atoms have been swapped with nitrogen, reduce oxygen in alkaline solution more effectively than the platinum catalysts that have been favored in fuel cells since the 1960s [56].

A computational study on SWNTs as CO<sub>2</sub> adsorbent has reported a CO<sub>2</sub> adsorption capacity of SWNTs to be twice that of activated carbon [57]. 3-aminopropyl-triethoxysilane (APTS)-modified CNTs have also exhibited increased CO<sub>2</sub> adsorption in gas streams [60]. In both cases, CO<sub>2</sub> is physisorbed even at ambient temperatures. Koo *et al* reported that MgO incorporation improved the adsorption of CO<sub>2</sub> on MgO-modified nickel catalyst in CO<sub>2</sub> reforming of methane due to increased base strength [61]. From the work done by Cinke *et al*, it is clear that CNTs might play a big role in CO<sub>2</sub> detection, bioremediation [57] and Carbon Capture and Storage (CSS). **Table 2.1** shows a summary of the possible applications for other components of the spent Ni catalysts.

**Table 2.1** A summary of the possible applications for other components of the spent Ni catalysts

Extractable Component	Use
Carbon encapsulated Ni nanoparticles	Nanomechanical and nanoelectronic devices, magnetic recording media, and biological sensors [62].
Nickel sulphate	Mainly used in electroplating [63].
Magnesium sulphate	Fertilizer, in medicine as a laxative, relief in asthma patients, lowering blood pressure and bath salts [64].

## 2.10 References

1. <http://www.engineeringnews.co.za/article/sa-pushes-ahead-with-carbon-dioxide-storage-atlas-project/2009/10/07>.
2. [http://www.ucsusa.org/global\\_warming/science\\_and\\_impacts/science/graph-showing-each-/2009/10/07](http://www.ucsusa.org/global_warming/science_and_impacts/science/graph-showing-each-/2009/10/07)
3. N. Muradov, F. Smith, Ali Raissi “*Catalytic Dissociation of Hydrocarbons: a Route to CO-free Hydrogen* “, Florida Solar Energy Center, University of Central Florida, Florida, U.S.A (2005)
4. <http://en.wikipedia.org/wiki/methane/2009/10/0732>
5. <http://www.epa.gov/methane/sources.html> 2009/10/07
6. C. Ponting, “*A New Green History of The World. London*”, Vintage Books (2006) 385- 387
7. V. Fornés, C. López, H.H. López, A. Martinez, *Appl. Catal. A: General*, 249 (2003)345–354
8. J. H. Lunsford, *Catal. Today*, 63 (2000) 165-174
9. A. M. Diskin, R. H. Cunningham, R. M. Ormerod, *Catal. Today*, 46 (1998) 147-154
10. J.R. B. Mota, E. Saatdjian, D. Tondeur A.E. Rodrigues, *Adsorption*, 1(1995) 1-27
11. S.P. Chai, S.H.S. Zein, A.R. Mohamed,” *A Review On Carbon Nanotubes Production Via Catalytic Methane Decomposition*”, 1<sup>st</sup> National Postgraduate Colloquim , School Of Chemical Engineering University of Sains Malaysia, Seri Ampangan (2004) 60-69
12. D. Sebastian, I. Suelves, M. J. Lazaro, R. Moliner, *J. Power Sources*, 192 (2009) 51-56.
13. [http://en.wikipedia.org/wiki/direct\\_carbon\\_fuel\\_cell](http://en.wikipedia.org/wiki/direct_carbon_fuel_cell) 2010/01/05
14. [www.alternative-energy-news.info/new-hope-for-hydrogen-storage/](http://www.alternative-energy-news.info/new-hope-for-hydrogen-storage/) 2009/10/07
15. M. A. Ermakova, D.Y. Ermakov, *Catal. Today* (2002) 225-235
16. R. Ramachandran, R.K. Menon, *Int. J. Hydrogen Energy*, 23 (1998) 593-598

17. S.A. Grigoriev, V.I. Poremsky, V.N. Fateev, *Int. J. Hydrogen Energy*, 31 (2006)  
171 – 175
18. L. Huang, E. E. Santiso, M. B. Nardelli, K.E. Gubbins, *J. Chem. Phys.*, 128 (2008)  
214702
19. A. Boudjemaa, A. Auroux, S. Boumaza, M. Trari , O. Cherifi , R. Bouarab, *Catal. Lett.*, (2009) 98:319–325
20. C-P Wang, H-S Chu, Y-YYan , K-L Hsueh, *J. Power Sources*, 170 (2007) 235–241
21. T. V. Choudhary, C. Sivadinarayana, C. C. Chusuei, A. Klinghoffer, D. W. Goodman, *J. Catal.*, 199 (2001) 9-18
22. K. Otsuka, S. Kobayashi, S. Takenaka, *Appl. Catal. A: General*, 190 (2000) 261-268
23. C.A. Querin, *Catal. R. Soc. Chem.*, 1 (2004) 166-206
24. P. Hu, Xianbao Wang, Yunqi Liu, Biao Wang, Daoben Zhu, *Syn. Met.*, 135 (2003)  
833-834
25. T. V. Reshetenko, L. B. Avdeeva, V. A. Ushakov, E. M. Moroz, A. N. Shmakov, V. V. Kriventsov, D. I. Kochubey, Yu. T. Pavlyukhin, A. L. Chuvilin, Z. R. Ismagilov, *Appl. Catal. A: General*, 270 (2004) 87-99
26. T.V. Reshetenko, L. B Avdeeva, Z. R. Ismagilov, A. L. Chuvilin , V. A. Ushakov, *Appl. Catal. A: General*, 247 (2003) 51-63
27. B. C. Liu, S. C. Lyu, T. J. Lee, S. K. Choi, S. J. Eum, C. W. Yang, C. Y. Park, *Chem. Phys. Lett.*, 373 (2003) 475-47
28. S. Takenaka, Y. Shigeta, E. Tanabe, K. Otsuka, *J. Catal.*, 220 (2003)  
468–477
29. G. Italiano, C. Espro, F. Arena, F. Frusteri , A. Parmaliana, *Catal. Lett.*, 124 (2008)7–12
30. H. F. Abbas, W.M.A.W. Daud, *Int. J. Hydrogen Energy*, 35(2010)  
1160– 190
31. K. Hadjiivanov, M. Mihaylov, D. Klissurski, P. Stefanov, N. Abadjieva, E. Vassileva,

- L. Mintchev, *J. Catal.*, **185** (1999)314–323
32. D. Chen, K. O. Christensen, E. Ochoa-Fernández, Z. Yu, B. Total, N. Latorre, A. Monzón, A. Holmen, *J. Catal.*, 229 (2005) 82–96
33. K. Hernadi, *Chem. Phys. Lett.*, 363 (2002)169-174
34. P. S. Arora, R. St. C. Smart, *Surf. Interf. Anal.*, 24 (1996) 539-548
35. J. Haber, J. H. Block, B. Delmon, *Pure & Appl. Chem.*, 67,( 1995)1257-1306
36. B. Huang, X. Li, S. Ji, Baolang, F. Habimana, C. Li, *J. Nat. Gas Chem.*, 17 (2008)225–231
37. J. A. Moulijn, A. E. Van Diepen, F. Kapteijn, *Appl. Catal.*, A 212 (2001) 3-16
38. <http://herkules.oulu.fi/isbn9514269543/html/x546.html> 2009/08/12
39. Z. Sarbak, *React. Kinet. Catal. Lett.*, 84 (2005) 263-270
40. M. A. Ermakova, D.Y. Ermakov, A. L. Chuvilin, G. G. Kuvshinov, *J. Catal.*, 201 (2001)183-197
41. F. Pompeo, N. N. Nichio, M. G. González, M. Montes, *Catal., Today*, 107 (2005) 856–862
42. J. L. Pinilla, I. Suelves, M.J. Lazaro, R. Moliner, J.M. Palacios, *Appl. Catal. A: General*, 363 (2009) 199-207
43. J. Sehested, *Catal. Today*, 111 (2006) 103–110
44. <http://www.chemicalelements.com/show/meltingpoint.html> 2009/07/06
45. G. Italiano , C. Espro , F. Arena , F. Frusteri , A. Parmaliana, *Appl. Catal. A: General* 357 (2009) 58–65
46. D. Chen, K. O. Christensen, E. Ochoa-Fernández, Z. Yu, B. Total, N. Latorre, A. Monzón, A. Holmen, *J. Catal.*, 229 (2005) 82–96
47. M. Inoue, K. Asai, Y. Nagayasu, K. Takane, S. Iwamoto, E. Yagasaki, K. Ishii *Diamond and Related Materials* 17 (2008)1471-1475
48. <http://igitur-archive.library.uu.nl/dissertations/2006-0906-201148/c2.pdf> 2009/06/12
49. C. H. Bartholomew, R.J. Farrato, “*Fundamentals of industrial catalytic processes*”, 2<sup>nd</sup> Edition; Wiley-Interscience: Hoboken, NJ, (2006)
50. A. K. M. F. Kibria, Y. H. Mo, K.S. Nahm, M.J. Kimb, *Carbon*, 40 (2002) 1241–1247
51. Y-H Wang, Bo-Qing Xu, *Catal. Lett.*, 99 (2005) 89-96

52. A. M. Venezia, A. Parmaliana, A. Mezzapica, G. Deganello, *J. Catal.*, 172 (1997) 463-470
53. M. Campanati, G. Fornasari, A. Vaccari, *Catal. Today*, 77 (2003) 299-314
54. D.L. Trimm, *Appl. Catal. A: General*, 212 (2001) 153-160
55. <http://www.chem-ilp.net/apparatus/Soxhlet.htm> 2009/05/12
56. Bethany Halford, *Chem. Eng. News.*, 87 (2009)7
57. M. Cinke, J. Li, C.W. Bauschlicher Jr., A. Ricca, M. Meyyappan, *Chem. Lett.*, 376 (2003) 761-766
58. [http://nanotechnology.e-spaces.com/carbon\\_nanofibers.html](http://nanotechnology.e-spaces.com/carbon_nanofibers.html). 2009/05/12
59. J. H. Cho, C. R. Park, *J. Catal. Today*, 120 (2007) 407-412
60. F. Su, C. Lu, W. Cnen, H. Bai, J. F. Hwang, *Sci. Total Environ.*, 407 (2009) 3017-3023
61. K.Y. Koo, H-S Roh, Y. T. Seo, D.J.Seo, W.L. Yoon, S.B. Park, *Appl. Catal. A: General*, 340 (2008) 183-190
62. J. Cheng, X. Zhang, Y. Ye, *J. Solid State Chem.*, 179 (2006) 91-95
63. [http://en.wikipedia.org/wiki/nickel\(ii\)\\_sulfate](http://en.wikipedia.org/wiki/nickel(ii)_sulfate) 2009/05/05
64. <http://www.buzzle.com/articles/uses-of-magnesium-sulfate.html> 2009/05/05

## CHAPTER 3 EXPERIMENTAL

### 3.0 Introduction

Owing to the vast range of industrial applications of heterogeneous catalysts, catalyst preparation methods are crucial in achieving a reproducible, desired catalytic performance such as activity, yield and selectivity. The composition and surface structure of the catalyst are key factors that control catalytic performance. In the case of supported metals, the nature of the support used to disperse the active metal also determines the catalytic activity through the nature of the metal-support interactions. Furthermore, modifiers/ promoters may exert intrinsic surface properties on the supported phase. As such, modifiers/promoters are incorporated into catalyst in a precise and controlled manner as they only exhibit their beneficial effects at a limited concentration [1].

This chapter will introduce the theories of the experimental techniques used, citing the reasons behind the choice of technique and the advantages and limitations of the technique. The chapter is broken into three parts, of which the first part begins with the preparation of the silica supported catalysts. The first part provides, by means of catalyst characterization, insights into the promotional effects of MgO in 20%Ni/SiO<sub>2</sub> catalysts used in direct methane decomposition. Catalyst characterisation techniques applied were; Induced Coupled Plasma - Atomic Emission Spectroscopy (ICP-AES), Nitrogen Physisorption, X-ray Diffraction (XRD), Temperature Programmed Reduction (TPR), H<sub>2</sub> -chemisorption and Oxygen titration.

The second part deals with the determination of the catalyst performance and the characterization of coke obtained from the series of the unmodified and MgO-modified 20%Ni/SiO<sub>2</sub> catalysts. Techniques used to provide information in this section were: Gas Chromatography (GC), Fourier Transform Infrared (FTIR) Spectroscopy, Raman Spectroscopy, Carbon/ Hydrogen/ Sulphur/ Nitrogen elemental analysis (CHNS), Thermogravimetric analysis (TGA), and Electron Microscopy (EM). A combination of the above techniques was used to obtain the overall effect

of MgO incorporation in 20%Ni/SiO<sub>2</sub> catalysts towards coke characteristics. The final part describes issues relating to the spent catalyst component recovery.

### **3.1 Catalyst Preparation**

A series of MgO-modified 20% Ni/SiO<sub>2</sub> catalysts was prepared by co-impregnation of colloidal silica, with crystals of Ni(NO<sub>3</sub>)<sub>2</sub>.6H<sub>2</sub>O and Mg(NO<sub>3</sub>)<sub>2</sub>.6H<sub>2</sub>O. The MgO dosage exploited the Mg<sub>at</sub>/Ni<sub>at</sub> ratio of 0.1- 2.2. The precursor slurry was then dried in an oven at 120 °C before calcination at 600 °C for 3 h [2]. The catalyst was heated at a rate of 10 °C/min to 600 °C. The calcined catalysts were ground to a mesh size ≤ 150 μm.

#### **3.1.1 Inductively Coupled Plasma -Atomic Emission Spectroscopy (ICP-AES)**

The chemical composition of the catalysts was determined by Induced Coupled Plasma- Atomic Emission Spectroscopy (ICP-AES SPECTRO Analytical Instruments). The samples were first digested in aqua-regia, microwaved in a closed system before dilution to concentrations within the detection range of the instrument. The technique exploits the fact that excited electrons emit energy at a given wavelength as they return to the ground state after excitation by a high temperature argon plasma. The intensity of the emitted energy at the chosen wavelength is proportional to the concentration of that element in the sample being analysed [3].

#### **3.1.2 Nitrogen Physisorption**

Textural characteristics such as the specific surface areas and pore volume were carried out using nitrogen adsorption and desorption isotherms, measured at -196 °C in a static volumetric apparatus (Micrometrics Tristar Sorptometer). About 0.3 g was used in each case for measurements. Prior to the analysis the samples were outgassed in a nitrogen flow at 150 °C for

6 h under vacuum. The Brunauer -Emmett -Teller (BET) equation and the single point method were applied for the calculation of the total surface area and the average pore volume respectively.

### **3.1.3 X-Ray Diffraction (XRD)**

X-ray diffraction studies on freshly ground calcined catalysts were performed on a Bruker AXS D8 diffractometer (Cu *K* radiation,  $\lambda = 0.15418$  nm), equipped with a graphite monochromator using silicon as an internal standard. Phase identifications were carried out by comparing the collected spectra with spectra in the database. Data were collected in the  $2\theta$  range of  $10^\circ$  to  $90^\circ$ .

### **3.1.4 Temperature Programmed Reduction (TPR)**

The reduction kinetics of a catalyst are crucial as they aid in determining the number of reducible species, the nature of metal-support interaction and the influence of MgO on the reducibility of NiO. Chemical reduction of the active component is a complex process that depends on: the nature of the precursor, particle size, surface pretreatment and stoichiometry. The reduction of NiO in the bulk of the active phase proceeds as follows:



In a typical TPR procedure, about 0.1 g of the calcined catalysts was loaded in a U-shaped quartz micro-reactor heated by an electrical furnace. Prior to the temperature-programmed reduction, samples were degassed in  $\text{N}_2$  at a pressure of 1 bar and temperature of  $150^\circ\text{C}$ . Upon cooling, 5%  $\text{H}_2$  in argon mixture was passed over the catalyst at a flow rate of 50 ml/min at 1 bar whilst heating at  $10^\circ\text{C}/\text{min}$  to  $900^\circ\text{C}$ . The  $\text{H}_2$  consumption was measured by analyzing the effluent gases with a thermal conductivity detector (TCD). The steam formed during the reduction was removed by a cooling trap. The  $\text{H}_2$  consumption profiles obtained were then integrated and recorded using Clarity software.

### 3.1.5 H<sub>2</sub> Chemisorption and O<sub>2</sub> Titration Analysis

Catalytic activity has been logically related to particle size distribution and dispersion of Ni particles which can be related to the physico-chemical characteristics of the support. H<sub>2</sub> gas chemisorption and O<sub>2</sub> titration were used to determine (i) the particle size of the Ni metal and (ii) the effect of MgO addition in silica supported Ni based catalysts on the dispersion of the metal on the support, sintering and the degree of reducibility. The methods applied for these techniques were adopted from Italiano *et al* [2] and Bartholomew *et al* [4]

About 0.2 g of the fresh calcined catalyst sample were loaded into a U-shaped quartz tube and evacuated. For the O<sub>2</sub> titration, samples were treated in oxygen (30 ml/min) for 30 mins at 400 °C and then reduced at 650 °C in H<sub>2</sub> (100 ml/min) for 3 h. The system was then flushed with pure He (100 ml/min) at 650 °C before reoxidising the exposed metallic metal with O<sub>2</sub> at 650 °C. The O<sub>2</sub> uptake at 650 °C was used to calculate the extent of reduction of NiO to Ni<sup>0</sup> for the Ni based catalysts.

Typical room temperature adsorption isotherms for H<sub>2</sub> chemisorption were determined by plotting micromoles of H<sub>2</sub> adsorbed vs pressure. The uptake due to chemisorption was then determined by extrapolating the straight-line portion of the isotherm to zero pressure.

The dispersion, % *D* was calculated from H<sub>2</sub> uptake according to equation (3.2) below assuming that the unreduced nickel was present in a separate dispersed layer in intimate contact with the support [4].

$$\%D = \frac{1.17X}{Wf} \quad (3.2)$$

where *X* = H<sub>2</sub> uptake in micromoles per gram of catalyst, *W* = weight percentage of nickel, and *f* = fraction of nickel oxide reduced to the metal.

The surface average Ni particle size,  $d_s$  was calculated by means of the equation (3.3) proposed by Smith *et al* [1]. The equation is based on the assumption that the metallic Ni particles are spherical.

$$d_s = \frac{101}{\%D} \quad (3.3)$$

### 3.1.6 Vibrational Spectroscopy

Vibrational spectroscopy was used to identify the nature/molecular composition of surfaces because it is specific for chemical bonds in molecules. The most common vibrational spectroscopies are FTIR and Raman. Raman and IR complement each other because not all molecular vibrations are both Raman active and IR active. Upon interaction with the incident radiation IR active molecules produce asymmetric vibrations while Raman active samples produce symmetric vibrations [5]. Raman spectroscopy was limited to the analysis of the spent catalysts and is discussed in detail in section 3.2.5.

#### 3.1.6.1 Infrared Spectroscopy (IR)

Conventional Fourier Transform Infrared (FTIR) spectroscopy was used to analyse the interaction of IR radiation with sample chemical functional groups which absorb IR radiation at certain frequencies. FTIR spectroscopy identifies functional groups based mainly on the stretching vibrations of molecules in the mid IR region of  $400 \text{ cm}^{-1}$  to  $4000 \text{ cm}^{-1}$ . The spent catalysts were analysed using Bruker Tensor 27 equipped with a diamond tip probe.

## 3.2 Catalytic activity and characterisation of coke

The relationship between the catalyst physico-chemical properties and the nature of carbon deposited on unmodified and MgO-modified 20% Ni/SiO<sub>2</sub> catalyst was based on the catalyst characterization techniques and coke characterization techniques.

### 3.2.1 Methane Decomposition: Experimental

The catalytic activity tests were carried out on a bench scale using a horizontal reactor. A schematic diagram for the reactor system used is presented in Figure 3.1. About 1 g of a catalyst was placed in a boat and activated *in situ* by reduction at atmospheric pressure under a H<sub>2</sub> (99.99%) flow (150 ml/min) at 650 °C for 3 h. Before the decomposition of methane, the system was flushed with argon ((99.99%) gas. The methane (>99.5%) gas feed was then passed over the activated catalyst for 72 h. After the reaction, the system was cooled down to room temperature in an argon atmosphere and the spent catalyst was subsequently removed from the reactor. The reactor temperature was controlled by electronic temperature controllers connected to the system through a thermocouple.

All the gases were supplied by AFROX (African Oxygen) Ltd. The activities of the Ni-based catalysts were compared in terms of methane conversion and the carbonaceous yield. Changes in catalytic activity and composition of the carbonaceous deposit were related to the dynamic, chemical and physical properties of the catalyst [1].

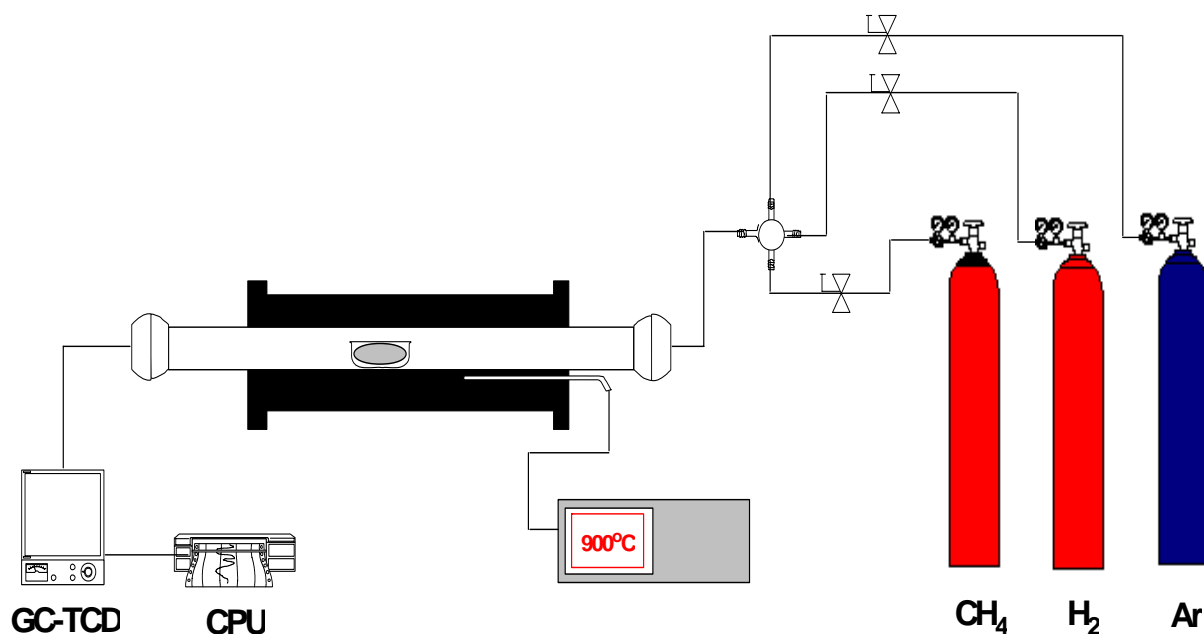


**Figure 3.1** A schematic diagram for the reactor system.

### 3.2.2 Gas Chromatography (GC)

The exit gas was analyzed by off-line gas chromatography. Gas chromatography is a powerful tool widely used for separation, identification and quantification of components in a mixture. In the technique, the gaseous sample is swept into a thermally-controlled column for analysis. Argon was used as a carrier gas in the GC. A GC chromatograph equipped with a thermal conductivity detector (TCD), and a Carboxen-1000 capillary column was used to determine methane conversion using Clarity software.

A typical chromatogram of the product gas analysis is illustrated in **Figure 3.2**. A calibration standard was injected into the GC and the retention times of the various components were used to identify components of the product gas. Methane conversion was expressed in terms of percentage areas of converted methane according to equation (3.4).

$$CH_4 \text{ Conversion} = \left( \frac{CH_{4IN} - CH_{4OUT}}{CH_{4IN}} \right) 100 \quad (3.4)$$

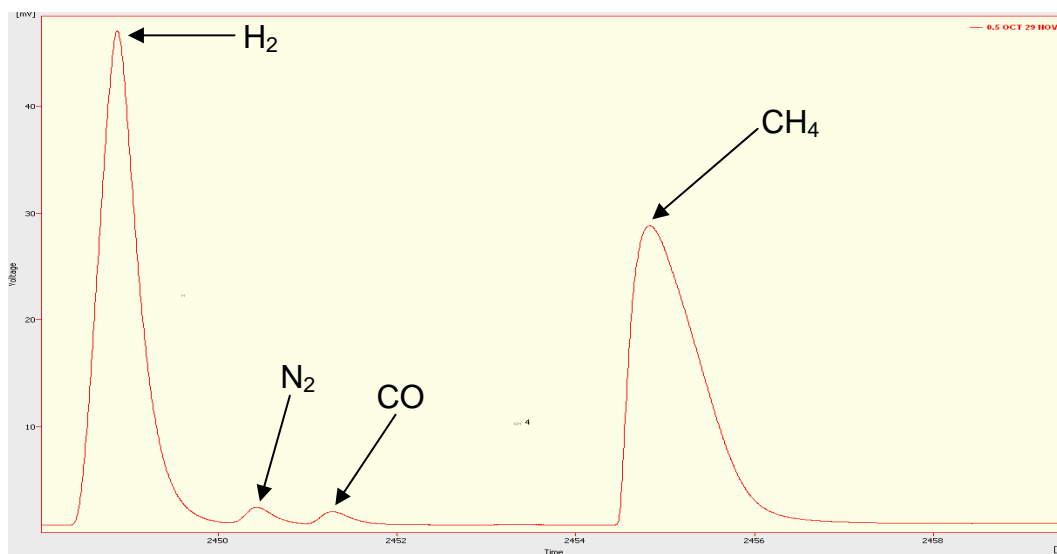


**Figure 3.2** A typical gas chromatogram of the exit gas obtained from catalytic methane decomposition over 20%Ni/SiO<sub>2</sub> catalyst.

### 3.2.3 Carbon, Hydrogen, Sulphur and Nitrogen Analysis (CHNS)

After each methane decomposition experiment, the boat loaded with the spent catalyst was weighed to determine the amount of deposited carbonaceous material. The carbon yield was also used to determine the best decomposition temperatures. The Carbon/ Hydrogen/Nitrogen / Sulphur (CHNS) elemental analysis was used to determine the actual elemental yield in the carbonaceous deposit in order to interpret the behaviour of the catalyst.

Quantitative analysis of the carbonaceous deposit was performed simultaneously on the LECO CHNS 932, equipped with thermal conductivity and infrared detectors. About 2 mg of sample was wrapped in a tin catalyst and dropped into a high frequency oven simultaneously with O<sub>2</sub> and combusted at 1000 °C. The product gases were carried by helium to a reducing environment

with copper wires heated at 800 °C. Oxides of nitrogen and sulphur were reduced to N<sub>2</sub> and SO<sub>2</sub> respectively and their concentrations were measured using a gas chromatogram equipped with a thermal conductivity detector [6]. The released CO<sub>2</sub> and H<sub>2</sub>O from carbon and hydrogen respectively are then measured by an infrared detector. Carbon yield was calculated as the fraction of total mass of the spent catalyst using CHNS analysis data using the following equation:

$$\text{Carbon Yield} = m_{tot} \times \%C_{CHNS} \quad (3.5)$$

where,  $m_{tot}$  is the mass of the spent catalyst.

In evaluating the promotional effect of incorporating MgO in silica supported nickel catalysts for hydrogen and carbon production, the carbon carrying capacity (C/Ni) of the unmodified and MgO-modified Ni/SiO<sub>2</sub> catalysts were recalculated taking into account the actual fraction of NiO reduced per gram of catalyst spent [2]. The following equation was applied:

$$\frac{C}{Ni_{red}} = \left( \frac{m_{tot}}{m_{cat} Wf} \right) \times \%C_{CHNS} \quad (3.6)$$

where  $m_{cat}$  is the mass of the fresh catalyst and  $f$  is the fraction of nickel oxide reduced to the metal.

### 3.2.4 Electron Microscopy (EM)

The spent Ni/SiO<sub>2</sub> catalysts surface structure and topography were examined by electron microscopy, a technique based on optical contrast. The overall optical contrast associated with the sample and photon interaction is caused by differential absorption of photons (amplitude contrast) or diffraction phenomena (phase contrast). EM provides identification of phase and structural information on crystals, direct images of surfaces, elemental composition and

distribution. In this study Conventional Transmission Electron Microscopy and Analytical Electron Microscopy were employed [7].

#### **3.2.4.1 Conventional Transmission Electron Microscopy (CTEM)**

The CTEM utilizes the amplitude contrast (bright field imaging mode), generating in favourable cases, and information on the active metal location on the support, particle size distributions, morphology and structural information on crystals [7].

#### **3.2.4.2 Analytical EM - Energy Dispersive X-ray Analysis (EDX)**

X-rays may be generated in the EM unit upon impingement of analyte sample with the incident beam/photon. A CTEM coupled to an EDX allows the analysis of characteristic X-rays generated in an EM unit. The patterns obtained are then compared with existing pattern in the database, allowing identification and quantification of elements with atomic number of at least 6 [7].

All ground TEM specimens were suspended in ethanol under ultrasonic vibration. The suspension produced was then transferred onto a perforated copper grid. The grid was then placed into the FEI Tecnai G<sup>2</sup> Spirit TEM transmission electron microscopy coupled to a double tilt holder of the EDX. The TEM apparatus operated at 120KeV. However CTEM was limited to analysing carbonaceous deposits because there was not enough contrast between the nickel oxide particles and silica support.

#### **3.2.5 Raman Spectroscopy**

Raman spectroscopy is based on the inelastic scattering of monochromatic radiation or photons upon impingement with the sample. The change in wavelength of the scattered radiation or photon provides the chemical and structural information of the sample. Raman scattering was

used to study the structural disorder of the carbonaceous deposit obtained over the 20%Ni/SiO<sub>2</sub> catalysts [5]. Ground carbonaceous samples were loaded into a sample holder in a micro-Raman spectrometer equipped with a laser source. The analysis was performed at a wavelength of 532 nm on the Jobin-Yvon T64 000 micro Raman Spectrometer.

### **3.2.6 Thermogravimetric Analysis (TGA)**

TGA is a thermal analysis technique in which the mass of the sample is monitored, against time or temperature, while the temperature of the sample, in a specified atmosphere, is programmed. TGA is used to measure changes in the mass of a sample as a function of temperature in a controlled atmosphere. From TGA curves, data on mass changes, thermal stability, decomposition temperatures, composition, and corrosion/oxidation reaction kinetics can be obtained.

In TGA, about 10 mg of sample was loaded into an aluminium cup supported by an analytical balance located outside the furnace chamber. The balance was zeroed and the sample cup heated according at 10 °C/ min. The sample was continuously weighed while being heated to 900 °C in an oxidative atmosphere. The thermogravimetric analyzer used was the Perkin Elmer STA 4 000.

### **3.3 Spent Catalyst Component Recovery**

In the spent catalyst, the soluble hydrocarbons can be removed through Soxhlet extraction. A Soxhlet extractor is a piece of apparatus designed to extract substances with a low solubility in a heated extracting solvent. It does this by allowing condensed solvent to wash through a paper thimble placed in the extractor which is designed to return the washings to the boiling flask by siphon action. [8]

About 15 g of the spent catalyst was placed in a cellulose thimble and loaded into the extractor with toluene heated at 110 °C for 12 h. The solvent was removed from the extract under vacuum using a rotary evaporator and concentrated to a volume of about 5 ml. The concentrated solvent was then analysed with a GC equipped with a FID [9].

Nickel leaching was proceeded by silica support removal [10]. After the Soxhlet extraction experiment, the dried spent catalyst was refluxed in 100 ml of 1M KOH aqueous solution for 2 h. The solid residue was washed with distilled water and dried. The Ni was then leached with sulphuric acid. The dried residue was then refluxed at 80 °C in 100 ml of 2M H<sub>2</sub>SO<sub>4</sub> for 1 h. The amount of leached Ni was determined with ICP and recorded as percentage recovery [11]. The residual coke was washed and dried and taken for TEM analysis.

### 3.4 References

1. C.H. Bartholomew, R.J. Farrato, “*Fundamentals of Industrial Catalytic Processes*”, 2<sup>nd</sup> Edition, Wiley-Interscience: Hoboken, NJ (2006)
2. G. Italiano, C. Espro, F. Arena, F. Frusteri, A. Parmaliana, *Catal. Lett.*, 124 (2008)7–12
3. J.M. Thomas, W.J. Thomas, “*Principle and Practice of Heterogenous Catalysis*”, VCH, Weinheim (1997)
4. D.G. Mustard, C.H. Bartholomew, *J. Catal.*, 67 (1981) 186-206
5. J. R. Ferraro, K. Nakamoto, C.W. Brown, “*Introductory Raman Spectroscopy*”, Academic Press, 2<sup>nd</sup> Edition, NY,(2003) 26
6. M. Thomas, “AMC Technical Briefs”, 29 *R. Soc. Chem.*, (2008)
7. J. Haber, J. H. Block, B. Delmon, *Pure & Appl. Chem.*, 67,( 1995)1257-1306
8. S. Mitra,” *Sample Preparation Techniques in Analytical Chemistry*”, vol 162, Wiley-Interscience, Hoboken, NJ (2006) 142
9. B. Delmon, G.F. Froment,” *Catalyst Deactivation*”, Proceedings of the 6<sup>th</sup> International Symposium (1994) 332
10. M.K. van der Lee, A.J. van Dillen, J.W. Geus, K.P. de Jong, J.H. Bitter, *Carbon* 44 (2006) 629–637
11. W. Mulak, B. Miazga, A. Szymczycha, *Int. J. Miner. Process.*, 77 (2005) 231– 235

## CHAPTER 4 RESULTS AND DISCUSSION

### 4.0 Introduction

This chapter presents and discusses results on the relationship between the catalyst physico-chemical properties and the nature of carbon deposited on unmodified and MgO-modified 20% Ni/SiO<sub>2</sub> during catalytic methane decomposition. Properties of the catalysts and carbon produced from the Ni supported catalysts were investigated using the methods presented in **Chapter 3**. It should be noted that the term coke refers to the carbonaceous species deposited on the catalyst.

### 4.1 Catalyst characterization

#### 4.1.1 Inductively Coupled Plasma -Atomic Emission Spectroscopy (ICP-AES) analysis

The amount of Ni and MgO loaded on the SiO<sub>2</sub> support was confirmed using ICP-AES analysis. **Table 4.1** shows the results of the ICP-AES analysis of the various catalysts after calcination. In **Table 4.1** **M** = Mg, **N** = Ni. The co-efficient represent the relative atomic ratios of Mg and Ni in the catalyst.

From the ICP-AES data in **Table 4.1**, it can be observed that the  $Mg_{at}/Ni_{at}$  in the range of 0.1- 2.2 was successfully attained. The lower values for Ni loading in catalysts with high MgO loading may be due to the formation of Ni<sub>x</sub>Mg<sub>1-x</sub>O solid solutions during calcination which might interfere with the acid leaching of ions [1].

**Table 4.1** Inductively Coupled Plasma-Atomic Emission Spectroscopy (ICP-AES) analysis results

Catalyst	Ni (%)loading	Mg (%)loading	Mg <sub>at</sub> /Ni <sub>at</sub> ratio
N-SiO <sub>2</sub>	19.0	-----	----
1M9N-SiO <sub>2</sub>	19.9	0.8	0.1
1M4N-SiO <sub>2</sub>	19.9	0.8	0.2
1M2N-SiO <sub>2</sub>	19.9	4.1	0.5
1M1N-SiO <sub>2</sub>	18.5	7.6	1.1
2M1N-SiO <sub>2</sub>	18.5	17.0	2.2

#### 4.1.2 Physico-chemical properties of the 20%Ni/SiO<sub>2</sub> catalysts

Catalytic activity depends on various factors including Ni particle size, dispersion and degree of reduction. The factors influencing catalytic activity will depend on the different nature of interaction between the active nickel species, MgO and the silica support. The basicity of the support may also play an important role [2]. **Table 4.2** presents physico-chemical properties of the 20%Ni/SiO<sub>2</sub> catalysts.

The results in **Table 4.2** indicate that the surface area of the Ni catalysts decreases with addition of MgO. The decrease in surface area with progressive addition of MgO suggests that MgO is

not a textural promoter [3]. Loss of surface area can be attributed to coverage of pores upon introducing MgO.

**Table 4.2** Physico-chemical properties of the 20%Ni/SiO<sub>2</sub> catalysts.

<b>Catalyst</b>	<b>SA<sub>BET</sub> (m<sup>2</sup>/g) ± 5%</b>	<b>NiO reduction degree ± 0.15%</b>	<b>Dispersion (% D) ± 0.15%</b>	<b>Average size <i>d<sub>s</sub></i> (nm) ± 2nm</b>
<b>N-SiO<sub>2</sub></b>	135	1.00	2.1	49
<b>1M9N-SiO<sub>2</sub></b>	133	1.00	2.2	47
<b>1M4N-SiO<sub>2</sub></b>	131	0.85	2.2	46
<b>1M2N-SiO<sub>2</sub></b>	110	0.87	2.6	40
<b>1M1N-SiO<sub>2</sub></b>	85	0.61	2.8	36
<b>2M1N-SiO<sub>2</sub></b>	54	0.34	2.2	46

The Ni particles show high dispersion on the silica support although the catalysts were prepared by the impregnation method which is usually associated with inhomogeneous distribution of the active component and low dispersion [4]. This result is consistent with reports in the literature that, when compared to other supports silica, usually ensures a better dispersion of nickel, regardless of the method of preparation [4].

It is generally accepted that supports with large surface area have better dispersion [5]; however **Table 4.2** indicates that in the 1M1N-SiO<sub>2</sub> and 1M2N-SiO<sub>2</sub> catalysts, Ni particle dispersion is even higher than in other catalysts despite progressive addition of MgO and consequently loss of

catalyst surface area. The presence of MgO in 1M1N-SiO<sub>2</sub> and 1M2N-SiO<sub>2</sub> catalysts seems to reduce the size of the Ni particles. These results are consistent with the findings of Jeong *et al* that addition of MgO to Ni/HY catalysts reduced the size of the Ni particles [6]. This result could be due to the formation of Ni<sub>x</sub>Mg<sub>1-x</sub>O solid solution which hinders the reduction of nickel ions and is more pronounced in catalysts with high MgO loadings [2]. Catalysts with a higher degree of reduction show a smaller nickel dispersion and large Ni particle size. For the 2M1N-SiO<sub>2</sub> catalyst, the low degree of reduction may have been due to excess MgO covering the nickel species [7]. Furthermore the loss of catalytic surface area due to the formation of the Ni<sub>x</sub>Mg<sub>1-x</sub>O solid solution may have promoted sintering leading to the large Ni particle size in the 2M1N-SiO<sub>2</sub> catalyst [8].

The difficulty in reduction of the Ni-based catalysts is also related to the formation of the nickel silicate species. The nickel silicate species could have been formed during calcination at 600 °C. Pease *et al* proposed that NiO-SiO<sub>2</sub> interactions are induced by the formation of SiO<sub>4</sub><sup>4-</sup> groups in the lattice of the NiO crystal at temperatures as low as 550 °C [9]. During reduction, a Si-Ni alloy may form, which might cause a lowering in the degree of reduction [2].

#### 4.1.3 X-Ray Diffraction analysis (XRD)

The diffraction patterns of the Ni-based catalysts were analysed to determine the phases of components present in the catalyst. As discussed earlier in **Chapter 2**, not all Ni faces are favourable for hydrocarbon decomposition. Diffraction planes for MgO, NiO and SiO<sub>2</sub> in the catalyst are shown in **Figure 4.1**.

It is known that the NiO and MgO components in the catalyst exhibit similar diffraction planes. This is because the Ni<sup>2+</sup> and Mg<sup>2+</sup> ions have similar valences, ionic radius values [ $r(\text{Ni}^{2+}) = 0.07$  nm and  $r(\text{Mg}^{2+}) = 0.065$  nm], and crystal cell dimensions. Thus, the NiO and MgO components in the catalyst can easily form a Ni<sub>x</sub>Mg<sub>1-x</sub>O solid solution due to the excellent mutual solubility

between them [10], as shown in **Figure 4.1**. Hence, the characterization of fresh catalysts by XRD did not allow particle size determination amongst the modified 20%Ni/SiO<sub>2</sub> catalysts due to the formation of the Ni<sub>x</sub>Mg<sub>1-x</sub>O solid solution.

Based on diffraction patterns in **Figure 4.2** and **Figure 4.3**, the diffraction peak in the range 15 - 30 ° confirmed the presence of amorphous SiO<sub>2</sub>. This result is consistent with the characteristics of amorphous SiO<sub>2</sub> [11]. The (111), (200), (220), (311) and (222) crystal planes for both MgO and NiO are observed around 37.5 °, 43.4 °, 62.9 °, 75.5 ° and 79.5 ° on the 2 theta scale [12,13]. Some studies have suggested that hydrocarbons decompose favourably to produce CNTs, on the Ni (100) and Ni (110) faces whilst the Ni (111) and Ni (311) faces are the favourable rear faces. The absence of the Ni (100) and Ni (110) suggests that methane decomposition occurred on the rear of the Ni (111) and Ni (311) crystal planes of the Ni particle [14]. Aroora *et al* also suggested that nickel/silica systems have predominated Ni (111) faces [9].

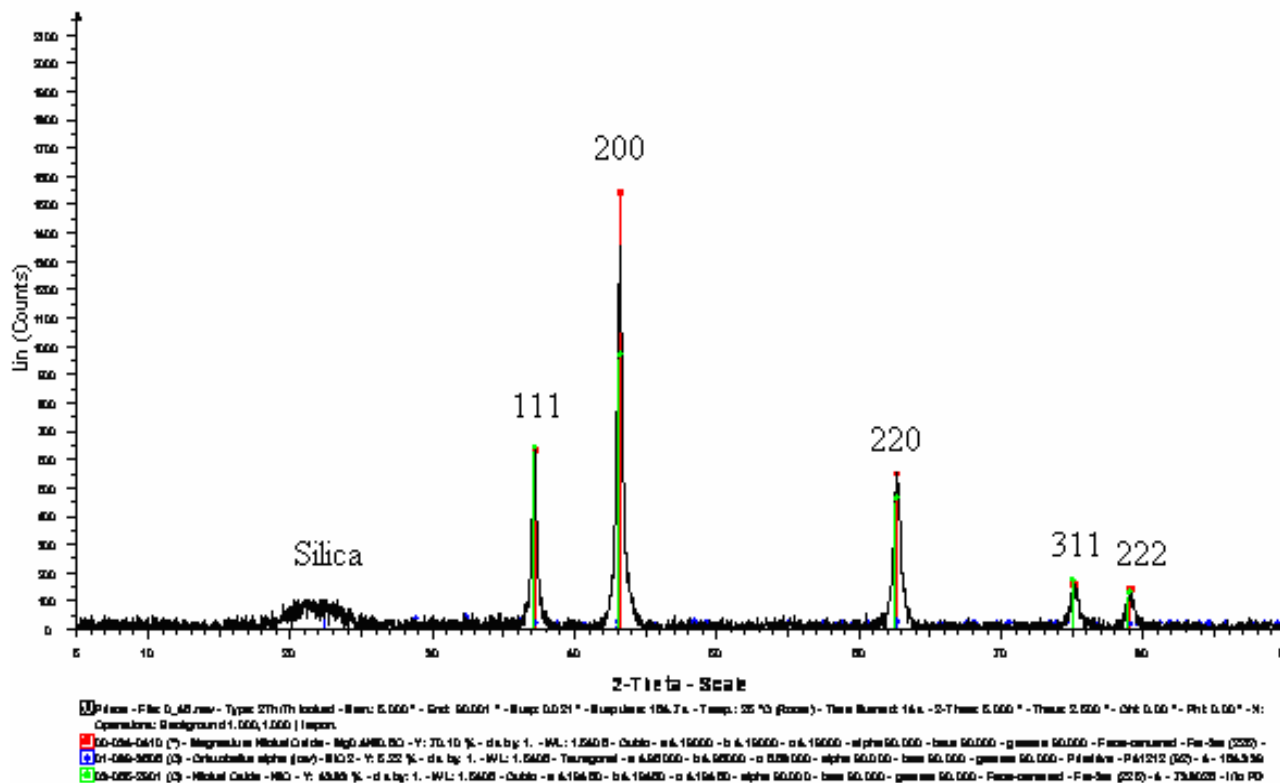


**Figure 4.1** Typical XRD pattern for 1M2N-SiO<sub>2</sub> catalyst.

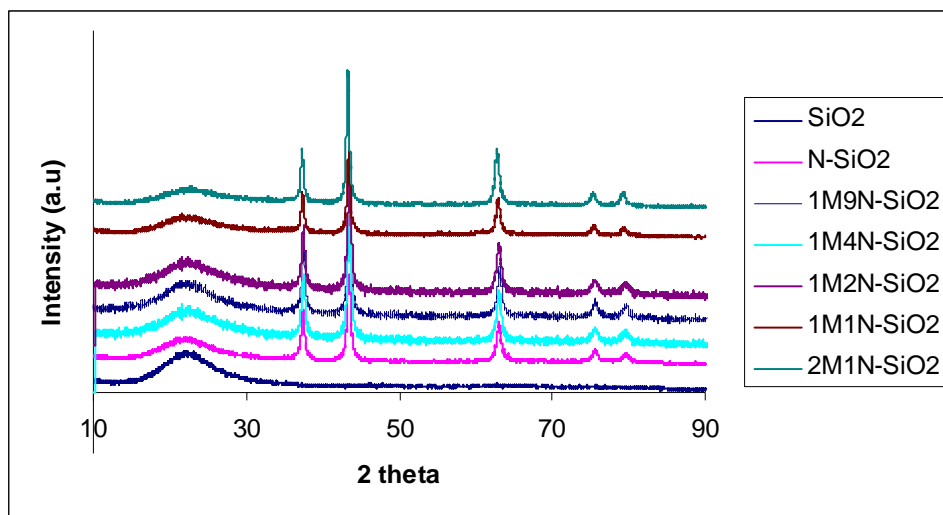


**Figure 4.2** XRD patterns of SiO<sub>2</sub>, N-SiO<sub>2</sub>, 1M9N-SiO<sub>2</sub>, 1M4N-SiO<sub>2</sub>, 1M2N-SiO<sub>2</sub>, 1M1N-SiO<sub>2</sub> and 2M1N-SiO<sub>2</sub>.

#### 4.1.4 Temperature Programmed Reduction (TPR)

The reduction profiles of the series of 20%Ni/SiO<sub>2</sub> catalysts were determined by TPR. The reduction profiles of the catalysts are shown in **Figure 4.3**. The TPR profile for the supported Ni catalysts is interpreted by invoking various degrees of interaction between NiO, MgO and SiO<sub>2</sub>, generally shown by three stages of H<sub>2</sub> consumption. A high H<sub>2</sub> consumption reflects the ease of reduction of a certain species in the catalyst sample. It can be observed that the relative rates of H<sub>2</sub> consumption at temperatures below 700 °C decline with progressive MgO loading.

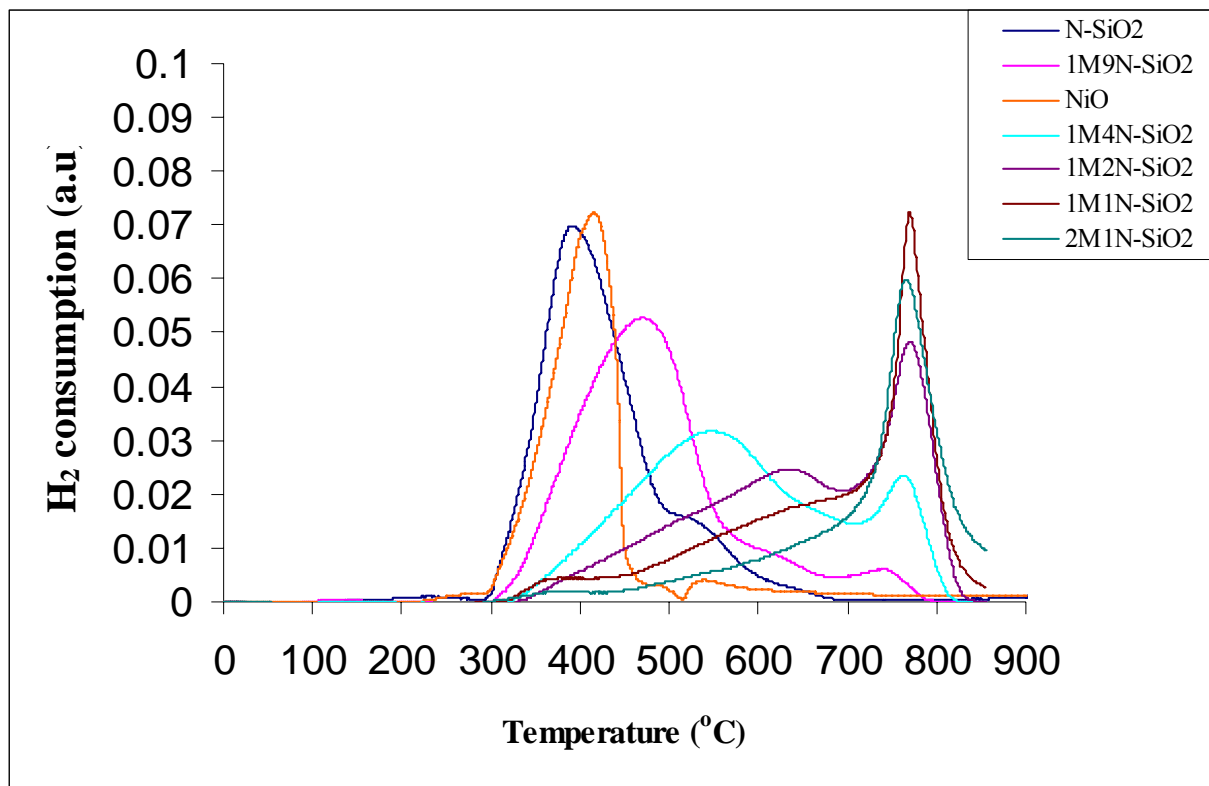


**Figure 4.3** TPR profile for NiO, N-SiO<sub>2</sub>, 1M9N-SiO<sub>2</sub>, 1M4N-SiO<sub>2</sub>, 1M2N-SiO<sub>2</sub>, 1M1N-SiO<sub>2</sub> and 2M1N-SiO<sub>2</sub> catalysts.

From **Figure 4.3**, it can be observed that the region between 300 °C and 487 °C corresponds to the reduction of the bulk NiO and highly dispersed NiO on the support. In this work one reduction peak was observed for bulk NiO, hence the variations of the H<sub>2</sub> consumption with temperature are not attributed to the presence of nickel ions in different oxidation states. NiO was assumed to be the dominant species present [15]. Hydrogen consumption in the region between 487 °C and 700 °C corresponds to the NiO species in interaction with SiO<sub>2</sub>, possibly as silicate species [15]. The reduction occurring in the region above 750 °C is attributed to the formation of hard to reduce Ni<sub>x</sub>Mg<sub>1-x</sub>O solid solution [3].

With the MgO-modified catalysts, a shift of the reduction signals to a higher temperature region is observed. The TPR profile indicates a lower H<sub>2</sub> consumption for the nickel silicate species with progressive addition of MgO to the catalysts than for the hard to reduce Ni<sub>x</sub>Mg<sub>1-x</sub>O solid solution. This result suggests that the MgO inhibits Ni-SiO<sub>2</sub> interactions by forming the hard to reduce Ni<sub>x</sub>Mg<sub>1-x</sub>O solid solution, due to the excellent mutual solubility between NiO and MgO. The effect of MgO is similar to the metal-support interaction inhibiting effect of K in K-promoted Ni/Al<sub>2</sub>O<sub>3</sub> catalysts [7]. The degree of reduction (**Table 4.2**) follows an analogous trend to the TPR profile of all samples.

It is generally accepted that large supported NiO particles are reduced at lower temperatures while small NiO particles are reduced at higher temperatures. Large NiO particles are reduced through a nucleation and fast propagation mechanism producing large Ni particles [16]. The hydrogen consumption in the region of 600-700 °C can be attributed to the reduction of stable Ni phyllosilicates which are characteristic of the reduction of small Ni particles in stronger interaction with SiO<sub>2</sub>, hence the higher reduction temperature [16]. The low mobility of the Ni species during the propagation step gives the high dispersion [16]. This proposal is consistent with the result that the Ni species in 1M1N-SiO<sub>2</sub> and 2M1N-SiO<sub>2</sub> catalysts in the region of 600-700 °C show enhanced reduction relative to the other catalysts due to the smaller particle sizes and consequently higher dispersion.

## 4.2 Catalytic activity and characterisation of coke

### 4.2.1 Methane Conversion

The activities of the Ni based catalysts were compared in terms of methane conversion using chromatograms similar to that shown in **Figure 3.2**. Both N<sub>2</sub> and CO gas peaks were observed in the chromatograms of the exit gas. However the CO peak was not observed in the chromatograms of by-passed methane. However the percentage areas due to these peaks were

less than 0.1%. This suggested that the CO peak was due to the reaction of product carbon and oxygen. The oxygen was derived from the support lattice [17]. The N<sub>2</sub> peak in both the bypassed methane and product exit gas suggested a systematic error probably due to a minor leak in the system. Percentage areas due to methane were used to calculate percentage methane conversion. After the decomposition of methane, the actual carbon yield obtained over the unmodified and MgO-modified 20%Ni/SiO<sub>2</sub> were determined by use of CHNS elemental analysis.

#### 4.2.2 The Effect of Temperature on Methane Decomposition

CHNS analysis data was used to determine the actual amount of carbon deposited at each given temperature. The choice of the optimum temperature of operation was made based on the amount of carbon deposited on the unmodified 20%Ni/SiO<sub>2</sub> (N-SiO<sub>2</sub>) in a temperature range of 500-800 °C. A graphical representation of the amount of the carbon deposited on the catalyst, and the corresponding temperature, is shown in **Figure 4.4** below. In **Figure 4.4**, it can be observed that increasing the temperature from 700 °C to 800 °C does not have much effect on the performance of N-SiO<sub>2</sub>. The results indicate that over a temperature range of 500-800 °C, the unmodified 20%Ni/SiO<sub>2</sub> exhibits an optimum temperature of methane decomposition at about 600 °C. Hence, all experiments on the catalytic effect of MgO on Ni/SiO<sub>2</sub> in methane decomposition were conducted at 600 °C.

Some researchers have reported the sintering of Ni particles from temperatures as low as 600 °C which they consider as the Tamman temperature [2]. According to Moulajn *et al*, Ni particles become more mobile as they approach the Tamman temperature (~ 726 °C) and consequently sinter to larger particles [18]. On the other hand, the solubility of carbon in Ni particles decreases with increase of hydrocarbon decomposition temperature. Furthermore, the diffusion of carbon on larger Ni particles is lower than the surface carbon formation rate; hence, at high temperatures

carbon accumulates on the surface of the active Ni particles, isolating them from the reactant gas [19]. Therefore, the low yield of carbon at temperatures of 700 °C and 800 °C suggests that the polymerization of carbon atoms might have occurred on nickel particles.

It is generally accepted that at low temperatures, the rate determining step is the adsorption of methane on the catalyst surface while at high temperatures the rate determining step is the dissolution of carbon atoms [19]. At 500 °C and 600 °C, the unmodified 20%Ni/SiO<sub>2</sub> catalyst gave a higher carbon yield than at 700 °C and 800 °C. This suggests that the adsorption of methane has less effect on the rate determining step than carbon dissolution.

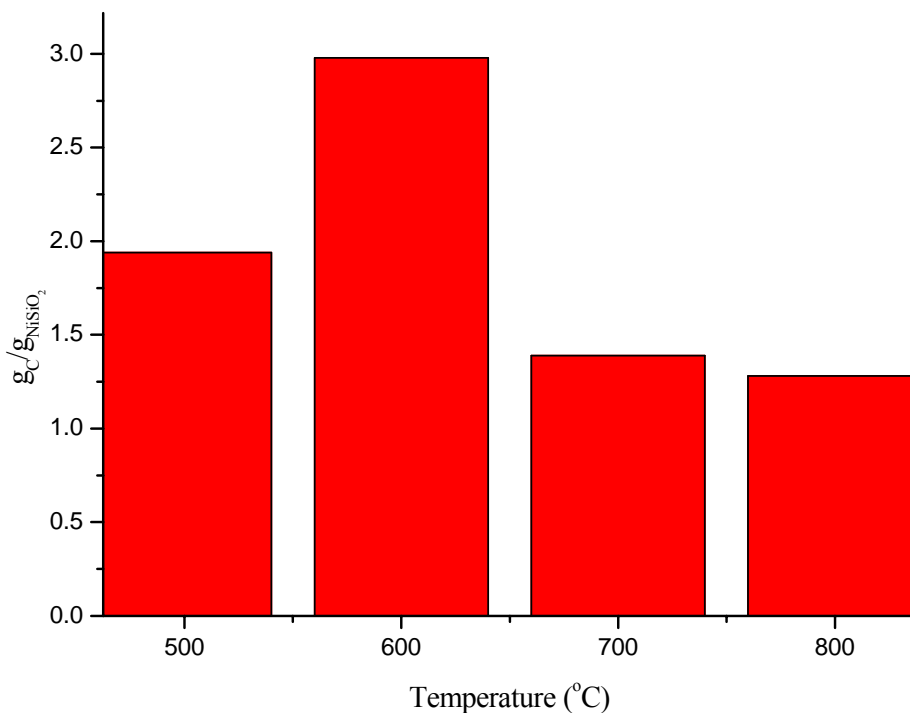


**Figure 4.4** Carbon yield obtained over N-SiO<sub>2</sub> in the range of 500 - 800°C.

### 4.2.3 Effect of MgO in 20%Ni/SiO<sub>2</sub> on carbon yield

A graphical illustration of amount of the carbon obtained at 600 °C on the unmodified and MgO-modified 20%Ni/SiO<sub>2</sub> catalysts is presented in **Figure 4.5**. The data shows that the N-SiO<sub>2</sub> catalyst had the highest carbon carrying capacity of 3.0g<sub>C</sub>/g<sub>cat</sub>. The lower carbon yields observed for the MgO-modified 20%Ni/SiO<sub>2</sub> catalysts suggests that the MgO exerts a carbon suppression effect on 20%Ni/SiO<sub>2</sub> catalyst and consequently methane decomposition.

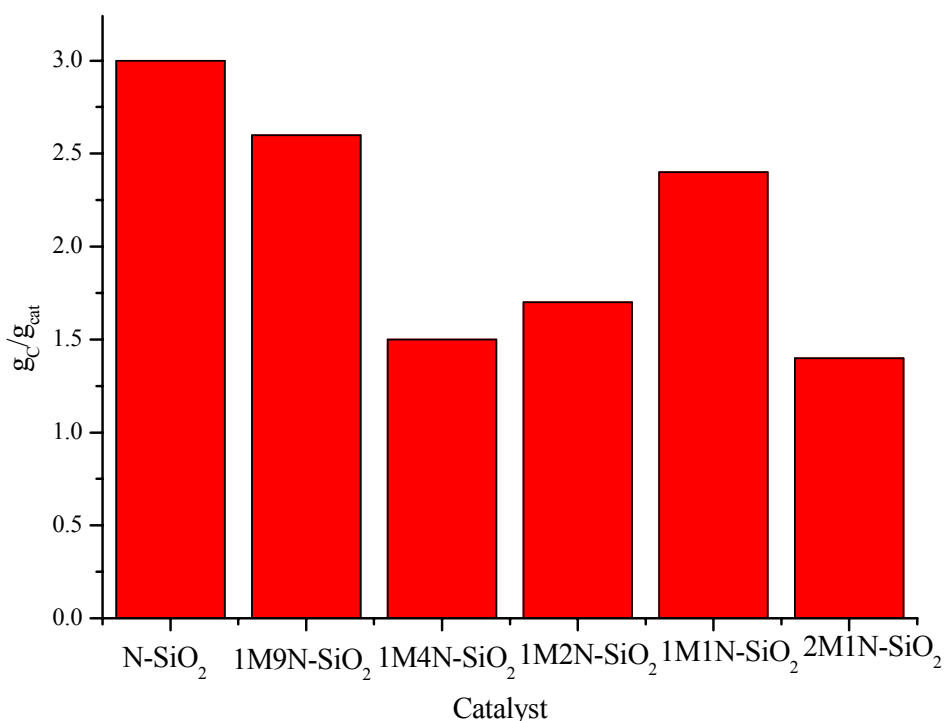


**Figure 4.5** Carbon yield on N-SiO<sub>2</sub>, 1M9N-SiO<sub>2</sub>, 1M4N-SiO<sub>2</sub>, 1M2N-SiO<sub>2</sub>, 1M1N-SiO<sub>2</sub>, 2M1N-SiO<sub>2</sub> catalysts at 600 °C after 72 h.

With reference to **Table 4.2**, the 1M1N-SiO<sub>2</sub> catalyst with an average Ni particle size of 36 nm had a fairly high carbon yield despite a low degree of reduction, suggesting that particle size may have a major contribution towards the effective decomposition of methane. This result is

consistent with the findings of Chen *et al* that the optimum Ni particle size for methane decomposition is in the range of 20-40 nm [5].

These results are also consistent with the suggestions of van Hardeveld *et al* that the specific nickel step density decreases with an increase in particle size [20]. Density Functional Theory studies (DFT) suggest that reactions at step sites dominate the overall activity [20]. This implies that the nickel step density may depend on the size of the nickel particle and consequently that the big particles are less efficient in decomposing methane.

The conflicting results concerning the variations in carbon yield over 1M9N-SiO<sub>2</sub>, 1M4N-SiO<sub>2</sub>, and 2M1N-SiO<sub>2</sub> catalysts (**Figure 4.5**) regardless of similar Ni particle dispersion and size (**Table 4.2**), also suggests that the degree of reduction also plays an important role. The lower carbon yields obtained over 2M1N-SiO<sub>2</sub> and 1M4N-SiO<sub>2</sub> catalysts could be attributed to a decreased number of available active nickel sites for methane decomposition. It can be observed from **Figure 4.5** and **Table 4.2**, that the 2M1N-SiO<sub>2</sub> catalyst with a lower degree of reduction than the 1M4N-SiO<sub>2</sub> catalyst has a similar carbon yield and Ni particle size. This result suggests that high reduction degree presents numerous particles that could easily sinter and not facilitate carbon deposition while a low degree of reduction presents very few nickel sites for methane decomposition. Excess MgO may also cover the most active Ni step sites in the 2M1NSiO<sub>2</sub> [20,7].

The carbon carrying capacity ( $g_C/g_{cat}$ ) of the unmodified and MgO-modified Ni/SiO<sub>2</sub> catalysts were recalculated taking into account the actual fraction of NiO reduced in one gram of catalyst spent. The recalculated values of  $g_C/g_{cat}$  per gram of catalyst spent were reported as  $g_C/g_{Ni_{red}}$  and plotted against the corresponding catalyst. A graphical illustration for the calculated values of  $g_C/g_{Ni_{red}}$  for the unmodified and MgO-modified Ni/SiO<sub>2</sub> catalysts is presented in **Figure 4.6**.

The calculated values of  $g_C/g_{Ni_{red}}$  per gram of catalyst spent indicate that the presence of MgO only exhibits its beneficial effect over N-SiO<sub>2</sub> (16  $g_C/g_{Ni_{red}}$ ) in 2M1N-SiO<sub>2</sub> (22  $g_C/g_{Ni_{red}}$ ), with  $Mg_{at}/Ni_{at}$  ratio of 2.2 and 1M1N-SiO<sub>2</sub> (21  $g_C/g_{Ni_{red}}$ ), with  $Mg_{at}/Ni_{at}$  ratio of 1.0) catalysts, in terms of carbon yield per reduced fraction of NiO particles per gram of catalyst spent. This result is not consistent with the findings of Italiano *et al* that reported a saturation-shaped trend with a plateau in  $g_C/g_{Ni_{red}}$  for  $Mg_{at}/Ni_{at}$  ratio higher than 0.5 in Ni/SiO<sub>2</sub>/Silica Cloth catalysts at a temperature of 600 °C [3].

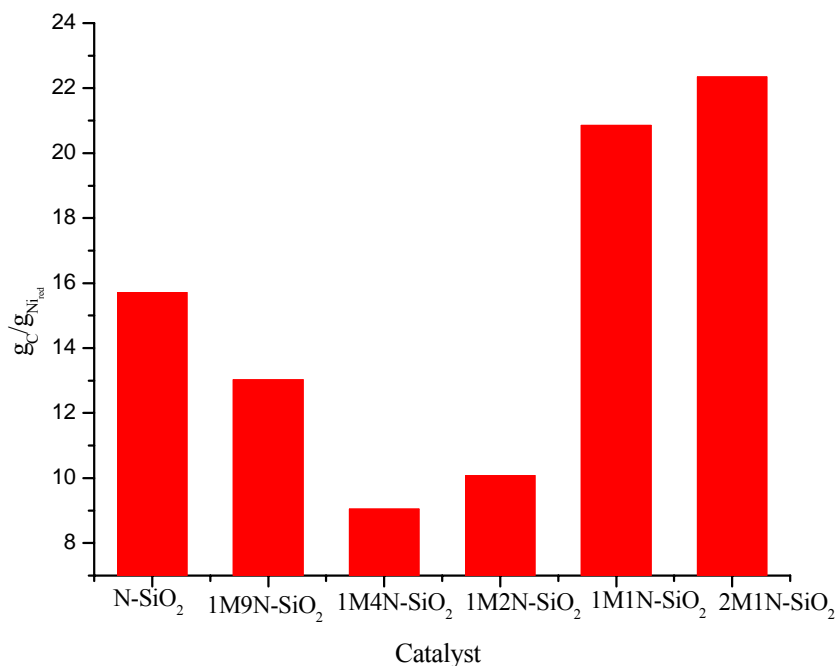


**Figure 4.6** Graphical illustrations of  $g_C/g_{Ni_{red}}$  corrected values for yields obtained over N-SiO<sub>2</sub>, 1M9N-SiO<sub>2</sub>, 1M4N-SiO<sub>2</sub>, 1M2N-SiO<sub>2</sub>, 1M1N-SiO<sub>2</sub> and 2M1N-SiO<sub>2</sub> catalysts at 600 °C.

However, by considering the actual carbon yield per gram of catalyst spent (**Figure 4.5**), it can be observed that the highest carbon carrying capacity of  $3g_C/g_{cat}$  and was obtained over N-SiO<sub>2</sub>

catalyst. Therefore we can conclude that it is not worthwhile to modify the 20%Ni/SiO<sub>2</sub> catalysts with MgO for direct methane decomposition.

#### 4.2.4 TEM analysis

TEM studies were conducted on the coke deposited on unmodified and MgO-modified Ni/SiO<sub>2</sub> catalysts at 600 °C. The TEM micrographs in **Figures 4.7a-4.11a** of the coke deposited on unmodified and MgO-modified Ni/SiO<sub>2</sub> catalysts revealed that the coke deposited on unmodified and MgO-modified Ni/SiO<sub>2</sub> catalysts has a filamentous structure. The corresponding diameter distributions of the carbon nanofilament obtained over the respective catalysts are shown in **Figures 4.7b-4.12b**. The carbon nanofilaments had diameters in the range of 20-100 nm. Carbon nanofilaments with diameters exceeding 100 nm were not grown. The carbon nanofilament diameter was assumed to be similar to the size of Ni particle from which it was grown. Therefore the results suggest that Ni particles with particle sizes exceeding 100 nm do not facilitate carbon deposition and consequently methane decomposition at 600 °C. These findings are consistent with the carbon nanotubes with the diameter of 20-100 nm commonly produced, while carbon nanotubes with the diameter exceeding 100 nm are unstable and are rarely grown [15,21].

The filamentous structure of carbon nanofilaments on both the unmodified and MgO-modified Ni/SiO<sub>2</sub> catalysts suggest that the presence of MgO does not modify the structural characteristics of the coke. The variation in carbon nanofilament diameter distribution suggests that sintering and attrition of the Ni particles, although some studies suggest that Ni particles in Ni/SiO<sub>2</sub> do not sinter significantly in H<sub>2</sub> atmosphere and that a carbon containing gas is a pre-requisite for sintering [22]. Upon exposure to the methane, Ni particles become more fluid under the action of carbon dissolved and sinter to large particles [15]. The TEM micrographs indicate the absence of encapsulating carbon. In this study the lack of amorphous carbon was attributed to the resistance of methane towards self-pyrolysis, up to temperatures as high as 800 °C.

Some studies have suggested that there is no typical strong metal-support interaction (SMSI) between Ni and silica in Ni/SiO<sub>2</sub> catalyst systems [4]. The TPR profiles also suggest that the addition of MgO to the 20%Ni/SiO<sub>2</sub> catalysts further inhibits SMSI. This idea suggests that carbon nanofilament formation may occur by the tip growth mechanism. Italiano *et al* also reported carbon nanofilament growth by the tip growth mechanism [3]. Other studies have suggested that hydrocarbons decompose favourably on the rear Ni (111) and Ni (311) faces [14]. Based on XRD patterns, it may be argued that filamentous carbon predominantly grows from the Ni (111) and Ni (311) faces by the tip-growth mechanism.

It can be observed from the TEM micrographs that most of the carbon nanofilaments appear broken. The breaking of the carbon nanofilaments as supports may contribute to loss of catalytic activity [3]. The carbon nanofilaments may break during the long synthesis times and the continuous deposition of carbon on the walls of carbon filaments. Carbon deposition might not occur along the layers parallel to the tube but randomly on the tube. The carbon nanofilament breakage may occur due to strain caused by continuous deposition of carbon on defective walls [23].

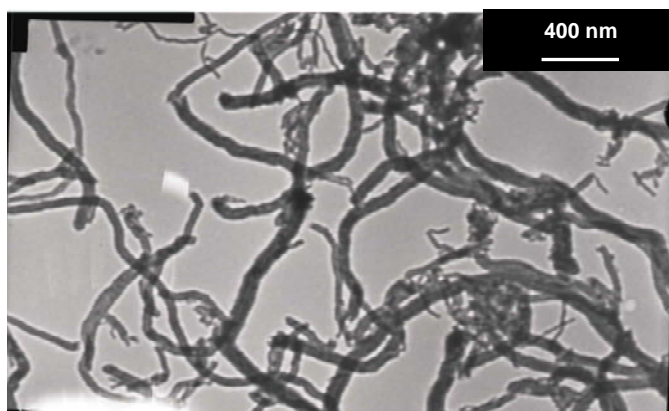


**Figure 4.7a** TEM micrograph of carbon nanofilaments obtained over the N-SiO<sub>2</sub> catalyst at 600 °C.

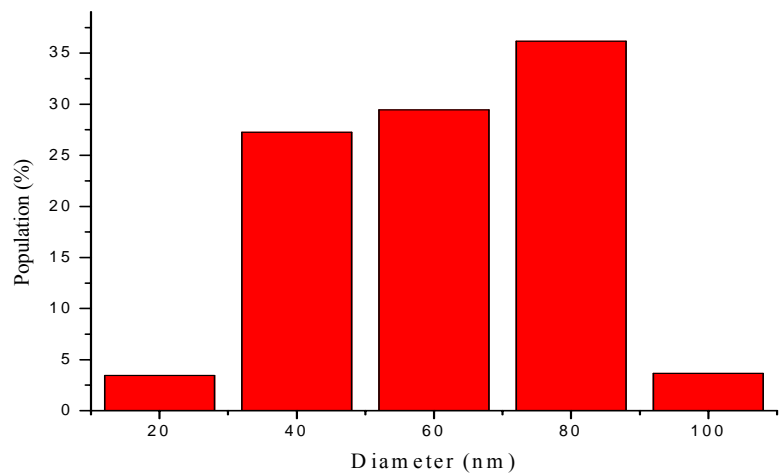


**Figure 4.7b** Diameter distribution of carbon nanofilaments obtained over the N-SiO<sub>2</sub> catalyst at 600 °C.

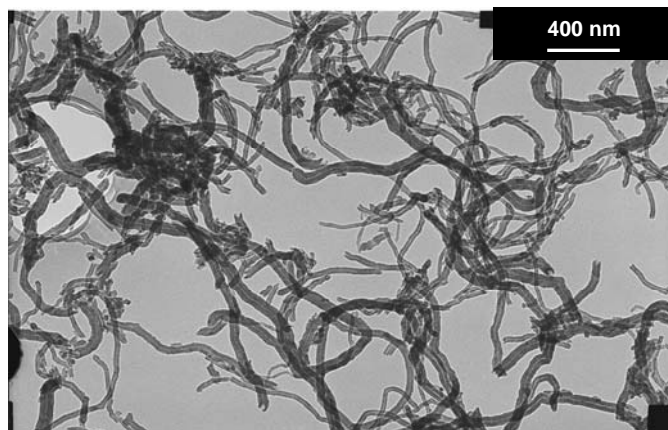


**Figure 4.8a** TEM micrograph of carbon nanofilaments obtained over the 1M9N-SiO<sub>2</sub> catalyst at 600 °C.

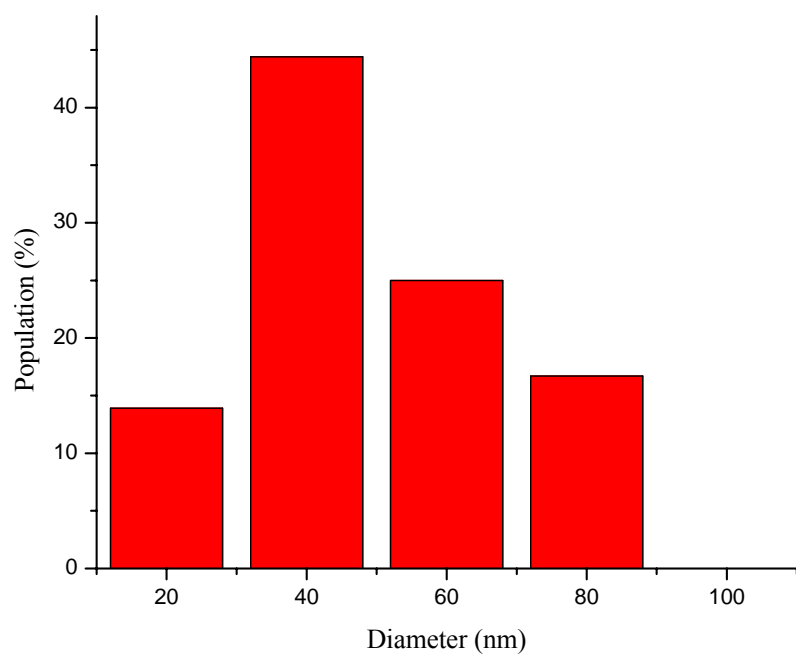


**Figure 4.8b** Diameter distributions of carbon nanofilaments obtained over the 1M9N-SiO<sub>2</sub> catalyst at 600 °C.

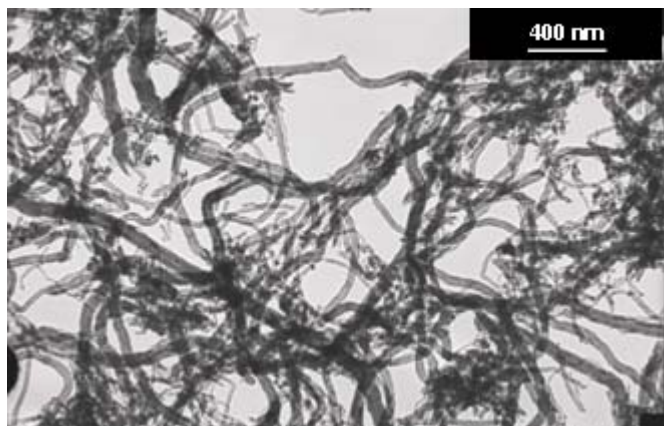


**Figure 4.9a** TEM micrograph of carbon nanofilaments obtained over the 1M4N-SiO<sub>2</sub> catalyst at 600 °C.

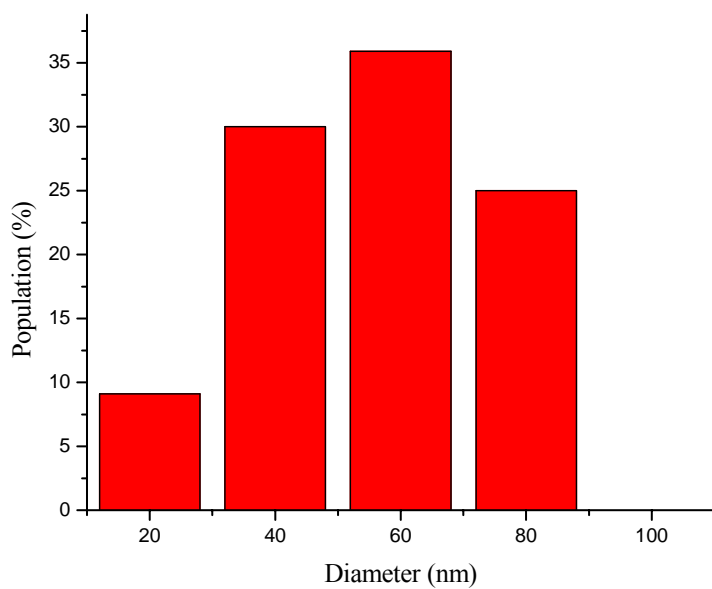


**Figure 4.9b** Diameter distributions of carbon nanofilaments obtained over the 1M4N-SiO<sub>2</sub> catalyst at 600 °C.

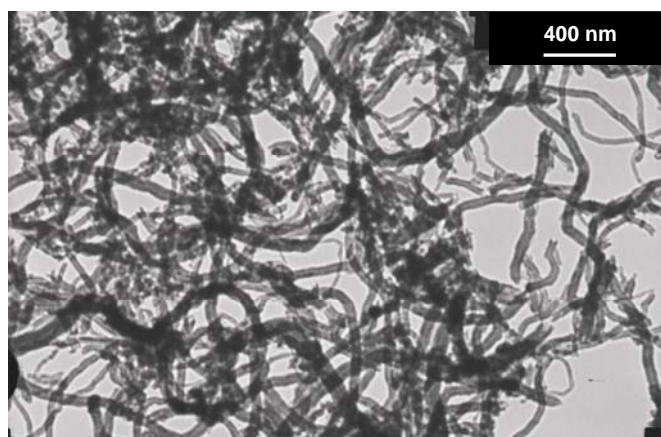


**Figure 4.10a** TEM micrograph of carbon nanofilaments obtained over the 1M2N-SiO<sub>2</sub> catalyst at 600 °C.

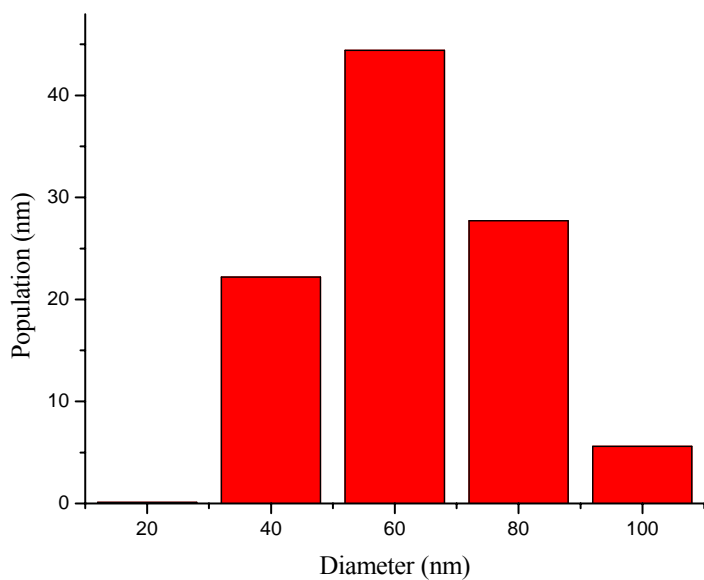


**Figure 4.10b** Diameter distributions of carbon nanofilaments obtained over the 1M2N-SiO<sub>2</sub> catalyst at 600 °C.

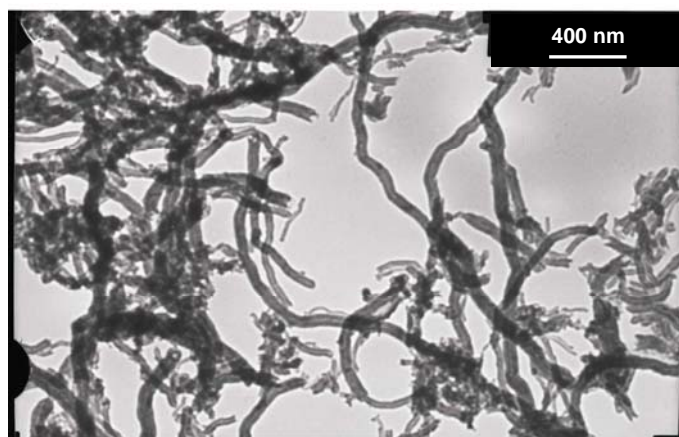


**Figure 4.11a** TEM micrograph of carbon nanofilaments obtained over the 1M1N-SiO<sub>2</sub> catalyst at 600 °C.

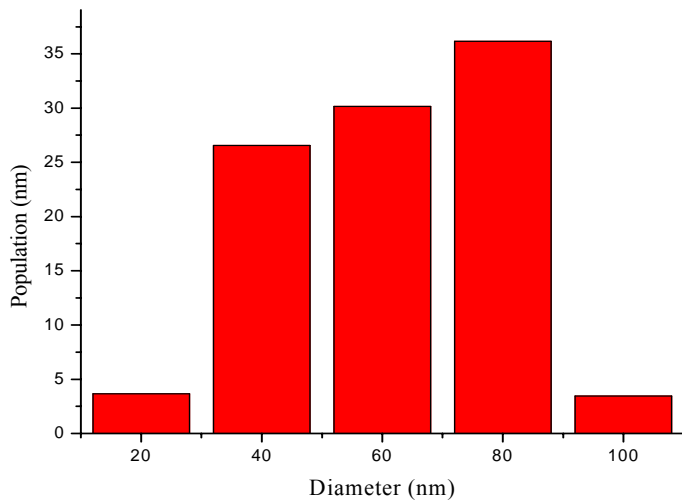


**Figure 4.11b** Diameter distributions of carbon nanofilaments obtained over the 1M1N-SiO<sub>2</sub> catalyst at 600 °C.

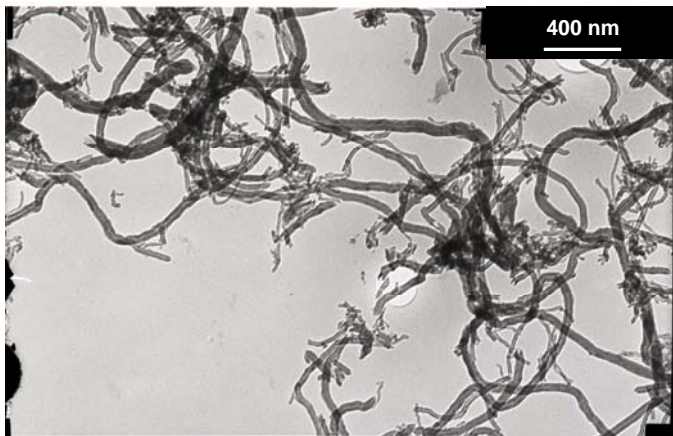


**Figure 4.12a** TEM micrograph of carbon nanofilaments obtained over the 2M1N-SiO<sub>2</sub> catalyst at 600 °C.

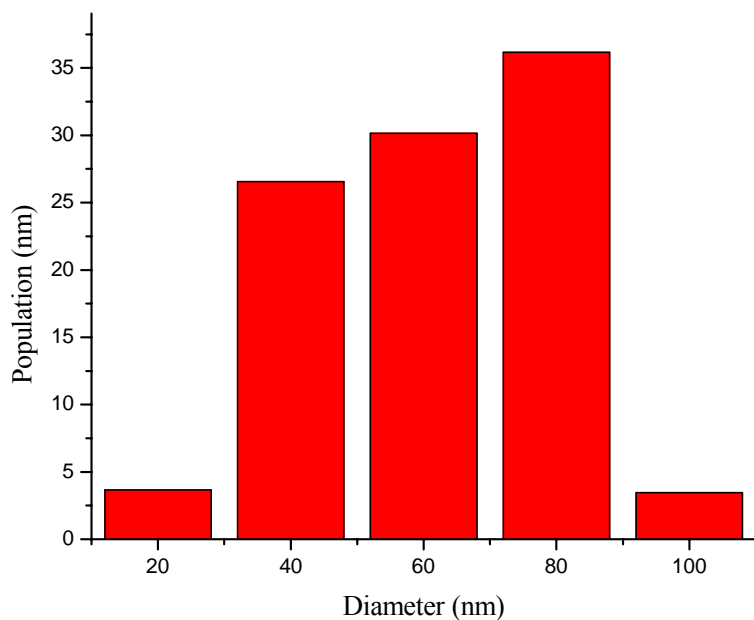


**Figure 4.12b** Diameter distributions of carbon nanofilaments obtained over the 2M1N-SiO<sub>2</sub> catalyst at 600 °C.

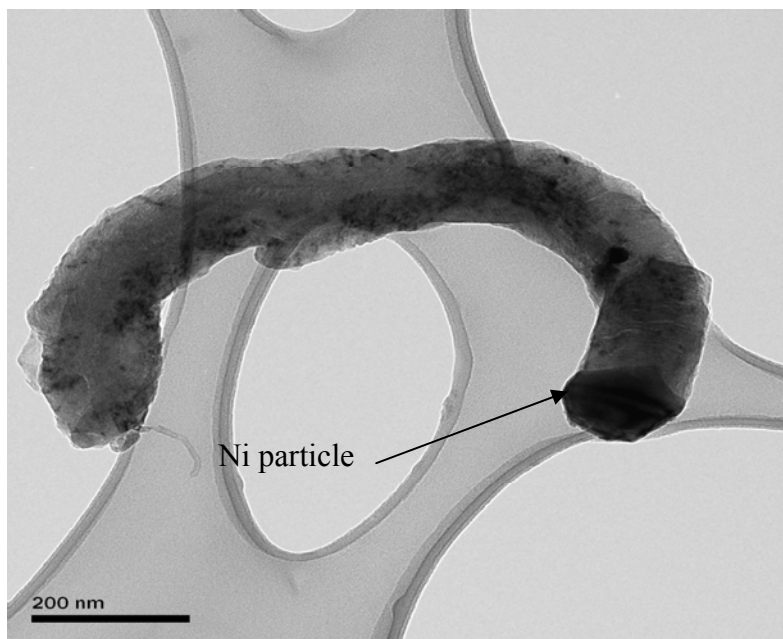


**Figure 4.13** TEM micrograph of a carbon nanofiber obtained over the 1M2N-SiO<sub>2</sub> catalyst at 500 °C, showing the presence of the Ni particle at the tip of the carbon nanofiber.

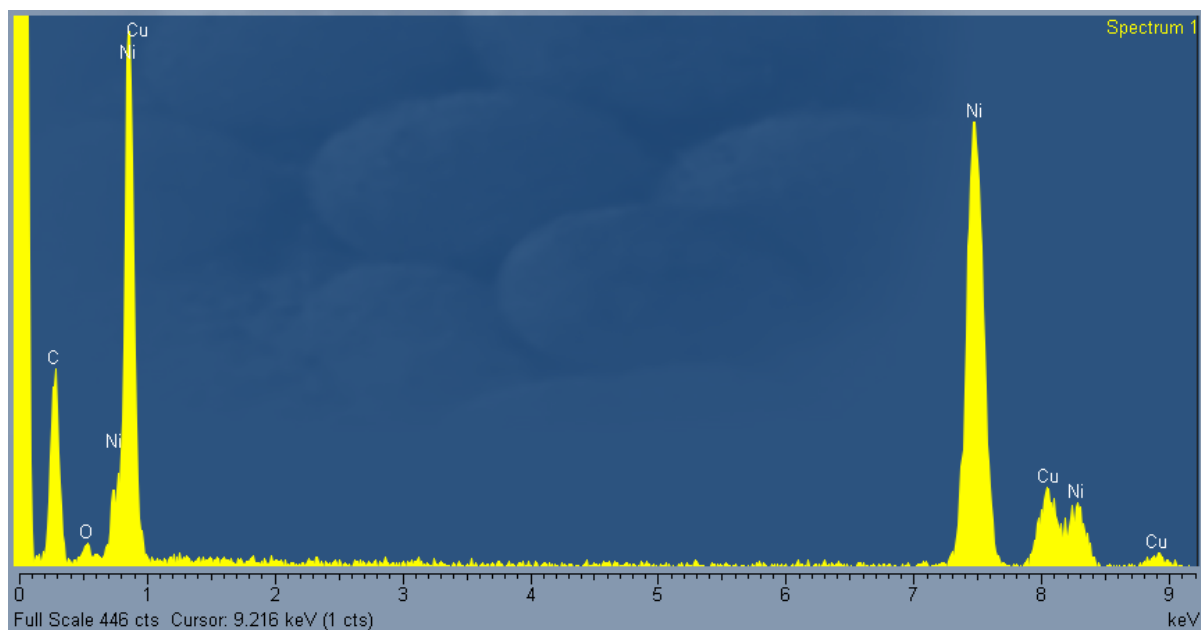


**Figure 4.14** Corresponding EDX pattern of the carbon nanofiber obtained over the 1M2N-SiO<sub>2</sub> catalyst at 500 °C.

The TEM micrograph in **Figure 4.13** and EDX pattern (**Figure 4.14**) of carbon nanofiber obtained over 1M2N-SiO<sub>2</sub> catalyst at 500 °C confirm the presence of the Ni particle at the end of the carbon nanofiber. From the EDX patterns and TEM studies we can assume that the growth of the carbon nanofilaments occurs by the tip growth mechanism. This result is consistent with the Ni particle being the active site for methane decomposition and suggests that MgO does not directly take part in the decomposition of methane [3]. The coke deposited does not block the active Ni metal but may act as a support for the active Ni particle with increasing time on stream. Hence, the active Ni metal is still exposed to the reactant gas. However filamentous carbon causes the breakage of the catalyst structure and may lead to pressure drop in the reactor [3].

#### 4.2.5 BET analysis

Surface area and pore volume measurements obtained from nitrogen physisorption are presented in **Table 4.3**. The BET data of the catalysts shows an increase in surface area for all the Ni based catalysts after methane decomposition. The increase in surface area is due to the formation of high surface area carbon nanofilaments as shown in TEM micrographs.

**Table 4.3** Surface area and pore volume measurements from nitrogen physisorption.

Catalyst	Fresh Catalyst		Spent Catalyst	
	SA <sub>BET</sub> (m <sup>2</sup> /g) ± 5%	Pore Volume cm <sup>3</sup> /g ± 5%	SA <sub>BET</sub> (m <sup>2</sup> /g) ± 5%	Pore Volume cm <sup>3</sup> /g ± 5%
N-SiO <sub>2</sub>	135	0.40	148	0.27
1M9N-SiO <sub>2</sub>	133	0.38	142	0.24
1M4N-SiO <sub>2</sub>	131	0.38	128	0.25
1M2N-SiO <sub>2</sub>	111	0.38	121	0.28
1M1N-SiO <sub>2</sub>	86	0.27	95	0.28
2M1N-SiO <sub>2</sub>	54	0.29	63	0.30

Based on the BET data and TEM analysis, catalyst deactivation cannot be attributed to blocked pores, since the coke is in the form of carbon nanofilaments. Italiano *et al* also suggested that the tip growth mechanism of carbon nanofilament formation invokes the detachment of the active nickel particle leading to the break down the catalyst structure [3]. Therefore the active Ni

particle will be continuously being exposed to the reactant gas until the carbon nanofilament breaks. The presence of hydrogen also ensures fresh Ni surfaces, which further enhance the catalytic reactivity and active sites for the formation of carbon nanofilaments.

#### **4.2.6 The Effect of MgO-modified 20%Ni/SiO<sub>2</sub> on methane decomposition**

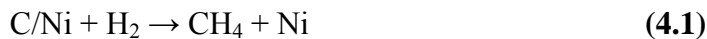
Methane conversion profiles obtained from the Ni catalysts at 600 °C are shown in **Figure 4.15**. Generally the methane decomposition graph activity exhibits 3 stages of activity: the initial stage characterized by high initial methane decomposition, the pseudo steady state and the catalyst deactivation stage. High initial methane conversions were obtained for all the catalysts. The initial methane conversions might have declined due to initial coke deposition on most of the active sites on the catalysts. The pseudo steady state might have been reached due to the growth of carbon nanofilaments. Considering the pseudo steady state, the highest methane conversions for the catalysts were in the range of 45-55 %. This result is consistent with the literature in that methane conversion at 600 °C is thermodynamically limited such that ( $H_2 > 60\%$ ) cannot be attained [24]. It has also been suggested that high hydrogen concentrations retard the growth of the carbon filaments and catalyst deactivation through competitive adsorption of the active sites between CH<sub>4</sub> and H<sub>2</sub> [25].

It can be observed in **Figure 4.15** that the N-SiO<sub>2</sub> catalyst had lower methane conversions than the MgO-modified catalysts during the pseudo steady state. Although MgO addition to Ni/SiO<sub>2</sub> seems to enhance methane conversion in the pseudo steady state, the MgO modified Ni-based catalysts accumulated less coke than the bare Ni catalyst. The inhibition of coke deposition on MgO-modified Ni/SiO<sub>2</sub> can be attributed to the Lewis basicity of MgO on the silica support [26].

The higher activity of the MgO-modified catalysts during the pseudo steady state may be explained by considering the contact of MgO species on the support and the nickel particle at the tip of the filamentous carbon. Over time there is less contact between MgO and the active nickel particle (which is the point of carbon growth). This suggests that the carbon formation is less hindered and hydrogasification occurs to a lesser extent [7]. However after 2 000 mins, (Figure 4.4) deactivation is abrupt for catalysts with a relatively high MgO loading. The reason for this might require further study.

The slower catalyst deactivation rate shown by the N-SiO<sub>2</sub>, 1M9N-SiO<sub>2</sub>, 1M4N-SiO<sub>2</sub>, 1M2N-SiO<sub>2</sub> and 2M1N-SiO<sub>2</sub> catalysts with larger average Ni particles than in the 1M1N-SiO<sub>2</sub> catalyst may be explained by the difference in the carbon diffusion rates in small and large Ni particles. Large Ni particles provide a smaller catalytic surface area and a longer diffusion length leading to lower carbon saturation and hence a slower deactivation rate [5].

Since the overall catalyst deactivation is the outcome of the reversible competing reactions, coke deposition and coke gasification (hydrogasification in this case) [27], the carbon suppressing effect of MgO on 20%Ni/SiO<sub>2</sub> based catalysts may be assumed to be the formation of easily gasifiable carbon. A reasonable hypothesis on the promoter effects of MgO can be analogous to the behaviour of potassium promoted nickel catalysts in steam reforming, where potassium is preferentially located along the more stable nickel step sites. The MgO as a carbon formation suppressor may block the nickel steps, eliminating the carbon nucleation sites [20]. The hydrogasification of carbon occurs at the nickel/carbon nanofilament interface, catalyzed by the nickel particle itself (Equation 4.1).



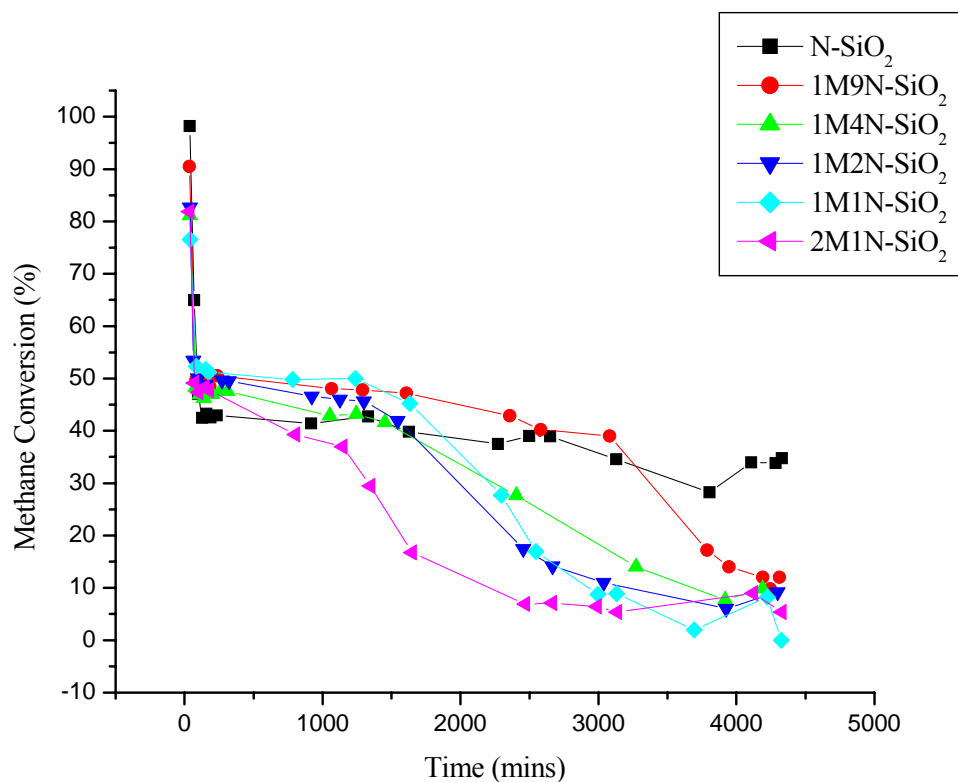


**Figure 4.15** Methane conversion profiles of the 20% Ni/SiO<sub>2</sub> catalysts; N-SiO<sub>2</sub>, 1M9N-SiO<sub>2</sub>, 1M4N-SiO<sub>2</sub>, 1M2N-SiO<sub>2</sub>, 1M1N-SiO<sub>2</sub> and 2M1N-SiO<sub>2</sub> catalysts at 600 °C.

Although it is known that MgO species acting as promoters in steam reforming can lead to the formation of C<sub>2</sub><sup>+</sup> hydrocarbons [28], C<sub>2</sub><sup>+</sup> hydrocarbons in the exit gas were not detected for MgO modified Ni based catalysis.

#### 4.2.7 Raman Spectroscopy

Raman spectroscopy measurements were taken at a 532 nm laser excitation wavelength. A typical Raman spectrum of carbon nanofilaments is shown in **Figure 4.16**. Two main spectral regions were detected for the carbon nanofilaments in the range 800 – 3000 cm<sup>-1</sup>. The spectra

were consistent with the findings of Donato *et al* [29]. The two main regions are characterized as;

- (a) the first-order Raman scattering attributed to the  $sp^2$  hybridized carbon atoms vibration bands in the range of  $1200-1700\text{ cm}^{-1}$ , and
- (b) the corresponding second order harmonic with vibration bands above  $2400\text{ cm}^{-1}$ [29].

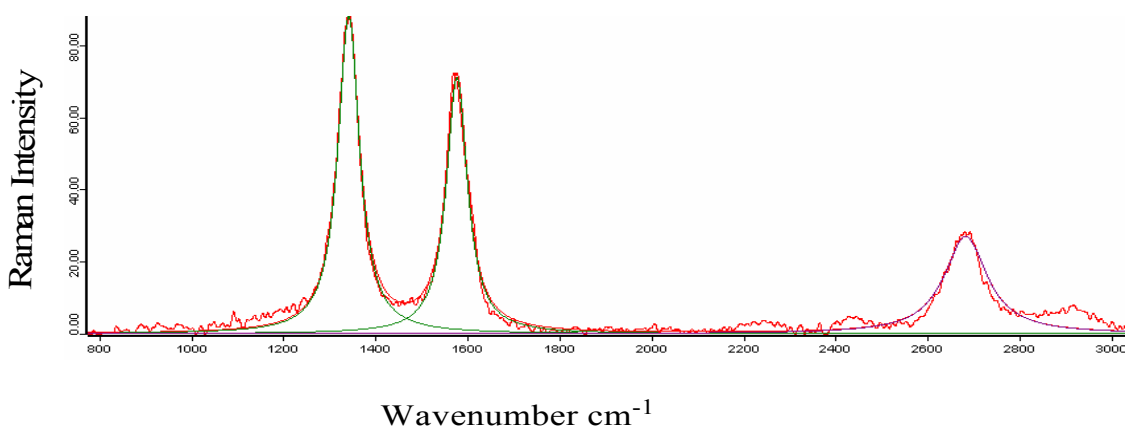


**Figure 4.16** A typical Lorentzian-Gaussian fit of a Raman spectrum obtained from coke deposited on the 1M1N-SiO<sub>2</sub> catalyst at 600 °C.

Prominent vibration bands around  $1338\text{ cm}^{-1}$ ,  $1567\text{ cm}^{-1}$  and  $2687\text{ cm}^{-1}$  can be observed in **Figure 4.16**. Vibration bands around  $1567\text{ cm}^{-1}$  are characteristic of the G-band arising from typical stretching modes of C=C bonds of graphite. The vibrational mode around  $1338\text{ cm}^{-1}$  designated the D (disorder)-band is characteristic of defective/disordered features in graphite sheets. The D-band emanates from double resonance attributed to the vibrations of carbon dangling bonds, in plane terminations of disordered graphite or amorphous carbon. The D-band is also associated with defects and impurities in CNTs [30]. The corresponding second order harmonic has vibration bands at  $2687\text{ cm}^{-1}$ . The second order harmonic is usually associated with the degree of crystallinity of the CNTs and the presence of MWNTs [31].

The D/G band area ratios ( $A_D/A_G$ ) determine the structural disorder originating from the formation of defects in the graphite sheets [29]. The lower the  $A_D/A_G$  ratio, the more graphitic and orderly the carbon nanofilaments are and vice versa [32]. The Raman spectra of carbon nanofilaments obtained in the methane decomposition temperature range of 500-600 °C are presented in **Figure 4.17**.

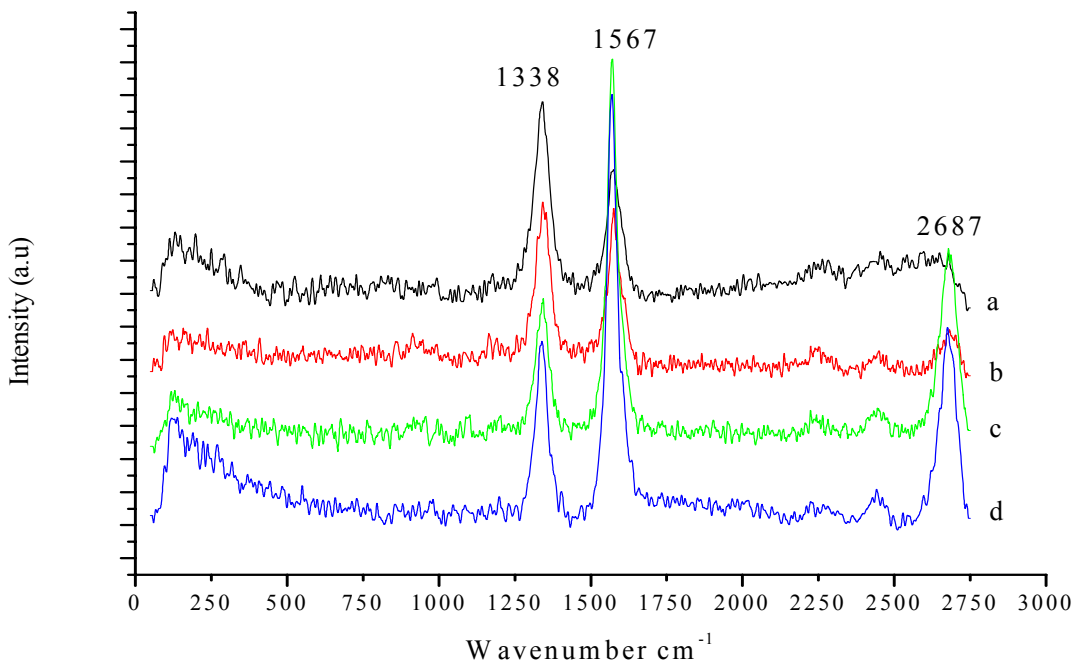


**Figure 4.17** Raman spectra of carbon nanofilaments obtained over N-SiO<sub>2</sub> at; (a) 500 °C, (b) 600 °C, (c) 700 °C and (d) 800 °C.

Although methane decomposition in Ni/SiO<sub>2</sub> systems is less efficient at temperatures higher than 650 °C, MWNTs formation has been reported to be highly favourable at 700 °C [21]. In the current work, the second order harmonic is absent in carbon nanofilaments obtained at 500 °C. This is because at 500 °C, CNFs formation is more favorable (**Figure 4.13**) than CNTs formation. This result is consistent with the findings of Takenaka *et al* that carbon nanofibers are formed at a temperature of 500 °C [21]. Therefore the appearance of the second order harmonic

around  $2687\text{ cm}^{-1}$  first observed on carbon nanofilaments formed at  $600\text{ }^{\circ}\text{C}$  suggests that methane decomposition from temperatures as low as  $600\text{ }^{\circ}\text{C}$  produces MWNTs.

The ( $A_D/A_G$ ) ratios of the carbon nanofilaments formed on unmodified  $20\%\text{Ni/SiO}_2$  catalyst (N-SiO<sub>2</sub>) at corresponding methane decomposition temperatures are presented in **Table 4.4**. The high ( $A_D/A_G$ ) value of 1.3 presented in **Table 4.4** indicates that there is high structural disorder in the carbon nanofilaments formed in the temperature range of  $500\text{-}700\text{ }^{\circ}\text{C}$ . However the lower  $A_D/A_G$  of 0.9 presented by carbon nanofilaments obtained at  $800\text{ }^{\circ}\text{C}$  suggests the improved order in the carbon deposit. The deterioration in orderliness at lower temperatures could be because of higher carbon deposition rates on the walls of the carbon nanofilaments. Carbon deposition may not occur along the layers parallel to the nanofilament but randomly on the nanofilament. The carbon nanofilament may break because of continuous deposition of carbon on defective walls [23].

**Table 4.4** Effect of temperature on structural disorder.

Catalyst/decomposition temperature	$A_D/A_G$
N-SiO <sub>2</sub> , T <sub>R</sub> 500	1.3
N-SiO <sub>2</sub> , T <sub>R</sub> 600	1.3
N-SiO <sub>2</sub> , T <sub>R</sub> 700	1.3
N-SiO <sub>2</sub> , T <sub>R</sub> 800	0.9

The Raman spectra of carbon nanofilaments obtained on unmodified-Ni/SiO<sub>2</sub> and MgO-modified Ni/SiO<sub>2</sub> catalysts are presented in **Figure 4.18**. It can be observed from **Figure 4.18** that the carbon nanofilaments obtained over all Ni/SiO<sub>2</sub> based catalyst have vibrational modes around  $2687\text{ cm}^{-1}$ .

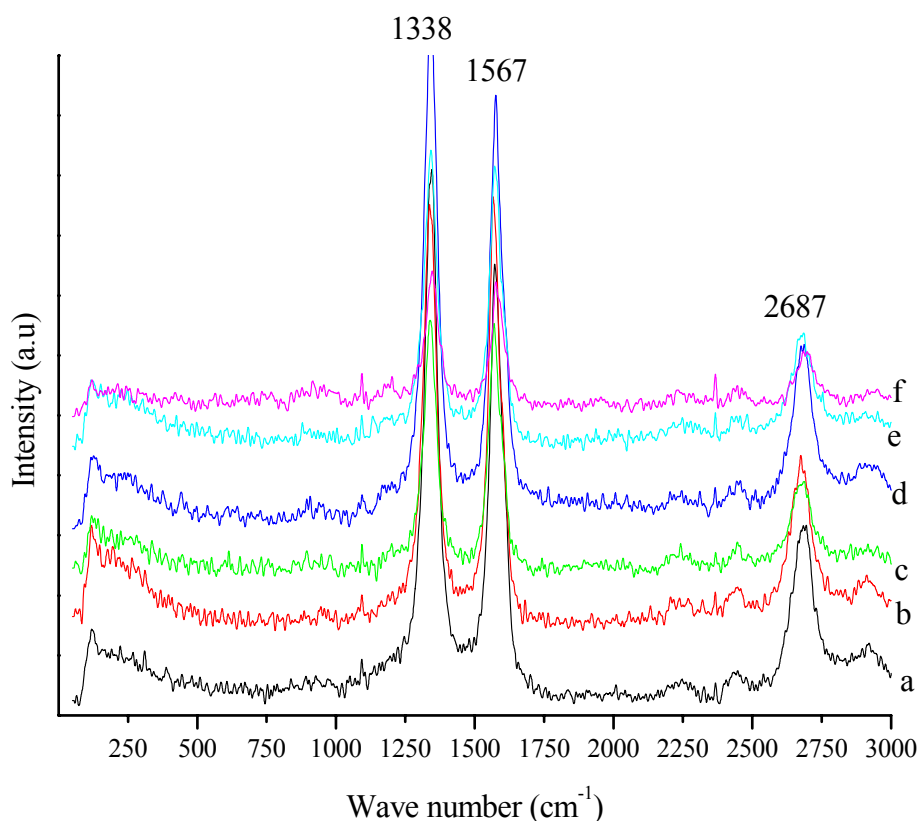


**Figure 4.18** Raman spectra of carbon nanofilaments obtained over unmodified- Ni/SiO<sub>2</sub> and MgO- modified Ni/SiO<sub>2</sub> catalysts; (a) N-SiO<sub>2</sub>, (b) 1M9N-SiO<sub>2</sub>, (c) 1M4N-SiO<sub>2</sub>, (d) 1M2N-SiO<sub>2</sub>, (e) 1M1N-SiO<sub>2</sub> (f) 2M1N-SiO<sub>2</sub> at 600 °C.

The effect of MgO addition on carbon nanofilament structural order was evaluated using  $A_D/A_G$  ratios. The results are presented in **Table 4.5**. From the data presented in **Table 4.5**, it can be observed from the  $A_D/A_G$  ratios that there is a high degree of disorder in the carbon obtained with the unmodified and MgO-modified 20%Ni/SiO<sub>2</sub> catalysts. TEM analysis of the carbon nanofilaments also suggests that these materials contain numerous defects at the ends of the filaments. The degree of disorder in the carbon nanofilaments obtained over the unmodified and MgO- modified 20%Ni/SiO<sub>2</sub> catalysts are almost similar suggesting that there is temperature

dependence for the degree of structural order in carbon nanofilaments. The results suggest that there is no distinct relationship between the degree of crystallinity or the amount of MgO added to the 20%Ni/SiO<sub>2</sub> catalysts.

**Table 4.5** Effect of MgO addition on carbon nanofilament structural disorder.

<b>Catalyst</b>	<b>A<sub>D</sub>/A<sub>G</sub></b>
<b>N-SiO<sub>2</sub></b>	1.3
<b>1M9N-SiO<sub>2</sub></b>	1.2
<b>1M4N2-SiO<sub>2</sub></b>	1.2
<b>1M2N-SiO<sub>2</sub></b>	1.2
<b>1M1N-SiO<sub>2</sub></b>	1.2
<b>2M1N-SiO<sub>2</sub></b>	1.3

#### **4.2.8 Thermogravimetric Analysis (TGA)**

Thermogravimetric analysis (TGA) experiments were performed in air. The TGA provided information on the oxidative stability of the carbon nanofilaments. The reactivity of the carbon nanofilaments towards oxygen manifest in the TGA weight loss profile. The oxidative stability curves of carbon nanofilaments when heated to 900 °C in air are shown in **Figure 4.19**.

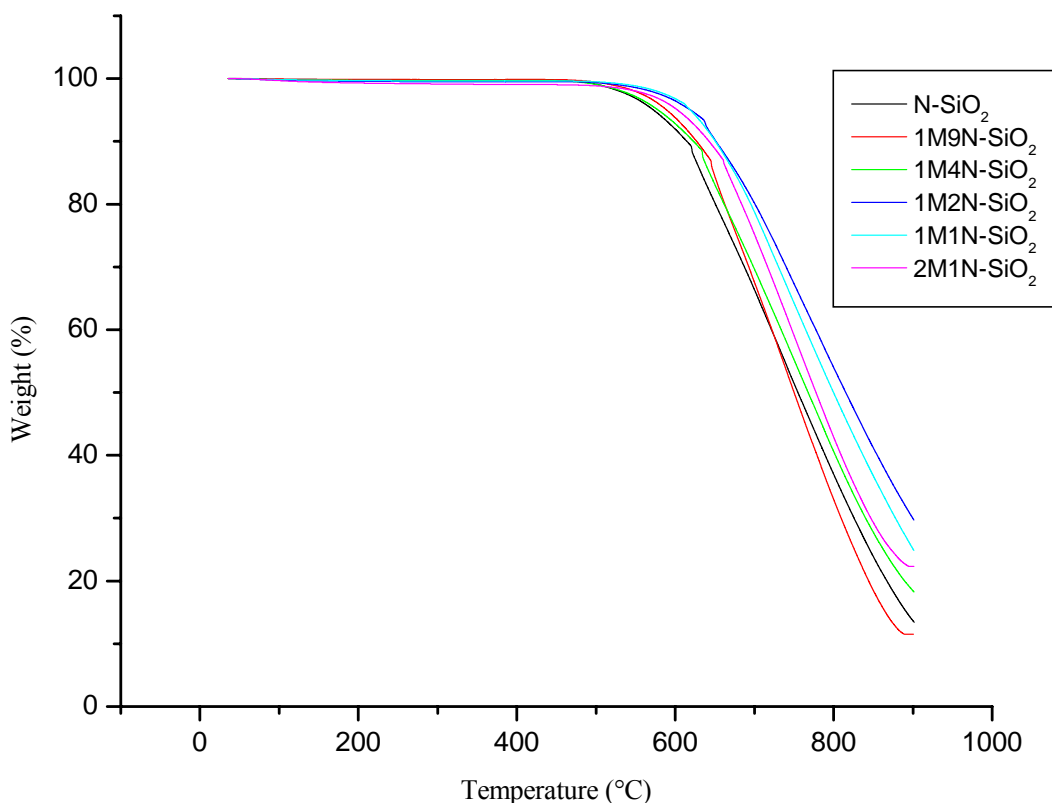


**Figure 4.19** The oxidative stability curves for the carbon nanofilaments obtained at 600 °C over the unmodified and MgO-modified Ni/SiO<sub>2</sub> catalysts; N-SiO<sub>2</sub>, 1M9N-SiO<sub>2</sub>, 1M4N-SiO<sub>2</sub>, 1M2N-SiO<sub>2</sub>, 1M1N-SiO<sub>2</sub> and 2M1N-SiO<sub>2</sub>.

The variation in the degree of steepness of the slope and consequently a higher reactivity toward oxidation may result from the difference in diameter and lattice defect site density. A smaller diameter results in a higher degree of steepness and subsequently a higher reactivity toward oxygen, while defects enable oxygen to permeate the carbon nanofilaments facilitating rapid oxidation [33].

During the thermogravimetric analysis the simultaneous reactions of carbon and nickel oxidation may lead to inaccurate results regarding the amount of carbon in the sample [27]. No weight gain was observed in the TGA profile. This result suggests that Ni particles in the sample might have

been partially oxidized during handling considering the nanometric nature of the Ni particles [34]. However, further oxidation of nickel to nickel oxide might result from the peeling away of graphite sheets through combustion [33]. It has been suggested that the presence of Ni might catalyze the oxidation of the carbon nanofilaments, however the exact nature of the mechanism is unknown [35].

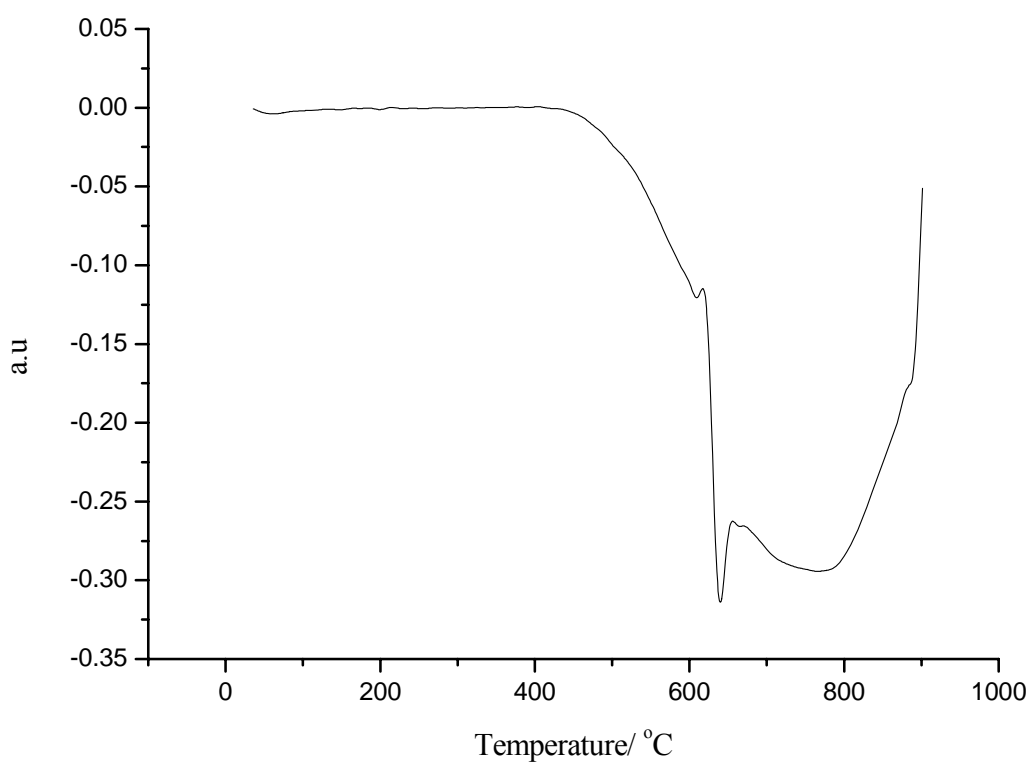


**Figure 4.20** The differential curve for the carbon nanofilaments obtained at 600 °C over the 1M2N-SiO<sub>2</sub> catalyst.

A typical differential curve of the oxidative stability of the carbon nanofilaments is shown in **Figure 4.20**. The differential curves of the oxidative stability curves of both the unmodified and MgO-modified 20%Ni/SiO<sub>2</sub> spent catalysts did not reveal major differences in the overall

stability of the carbon nanofilaments. The differential curves of all the samples showed two sharp peaks and a broad peak centred around 600 °C, 630 °C and 740 °C respectively. This result suggested that there is no major difference in the overall oxidative stability of the carbon nanofilaments obtained from both the unmodified and MgO-modified 20%Ni/SiO<sub>2</sub> catalysts. The result could be because there is no significant variation in crystallinity of the carbon nanofilaments obtained over the catalysts as suggested by the data obtained from Raman spectroscopy.

#### 4.2.9 Infrared Spectroscopy (FTIR)

The IR transmission spectra of the spent catalyst are shown in **Figure 4.21**. With reference to the TEM images of the coke obtained it can be observed that the carbonaceous material is mainly CNFs/CNTs. To date, not much IR spectral information on as-grown CNTs has been collected [36].

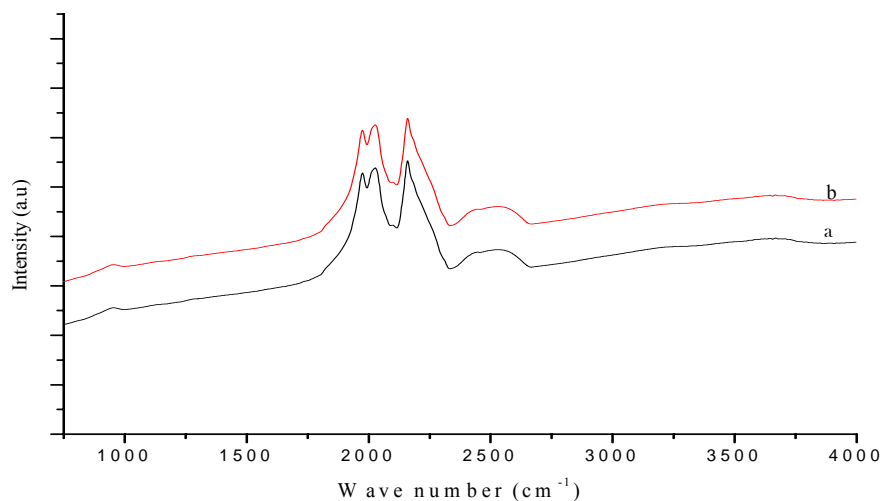


**Figure 4.21** FTIR transmission spectra of the spent catalyst obtained over (a) spent N-SiO<sub>2</sub>, (b) spent 1M1N-SiO<sub>2</sub> catalysts at 600 °C.

It can be observed from **Figure 4.21** that the as-grown carbon nanofilaments strongly absorbed infrared radiation over the mid IR region (600- 4000  $\text{cm}^{-1}$ ). Spectral features (aromatic bands) of conventional coke are usually seen bands at 1590, 1460, 1390 and 1380  $\text{cm}^{-1}$ , which characterize aromatic C-C stretching,  $-\text{CH}_2$  and  $-\text{CH}_3$  bending respectively [37]. The spectral features characteristic of conventional coke was not observed. The characterization of the spent catalysts by FTIR did not reveal much information on the nature of carbon contained in the solids.

### 4.3 Spent Catalyst Component Recovery

The unmodified 20%NiSiO<sub>2</sub> spent catalyst (N-SiO<sub>2</sub>) was weighed before and after Soxhlet extraction. The mass of the spent catalyst before and after Soxhlet extraction was recorded in **Table 4.6**. The absence of a significant mass loss indicates that there were relatively no toluene-soluble organic components in the spent catalyst.

**Table 4.6** Mass of the spent catalyst before and after Soxhlet extraction.

Catalyst	Mass of catalyst before extraction (g) $\pm$ 0.0001g	Mass of catalyst after extraction (g) $\pm$ 0.0001g	Change in mass of catalyst (g) $\pm$ 0.0001g
N-SiO <sub>2</sub>	14.5047	14.4979	0.0068

Chromatograms of toluene before and after Soxhlet extraction of the coke are shown in **Figure 4.22** and **Figure 4.23** respectively. The chromatograms were obtained from obtained from a GC equipped with a FID. There was no significant change in the integrated peak areas of the toluene before and after Soxhlet extraction. Furthermore the absence of new peaks in the chromatogram

of toluene after Soxhlet extraction (compare **Fig 4.22** and **Fig 4.23**) also suggests that there were no extractable components in the coke.

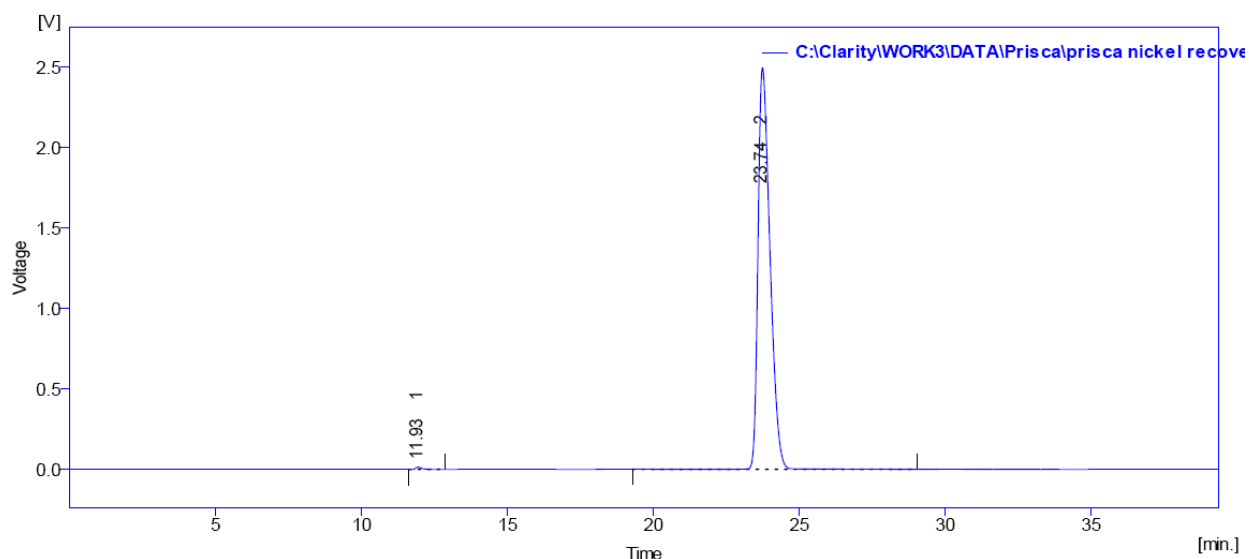


**Figure 4.22** Chromatogram of neat Toluene before Soxhlet extraction.

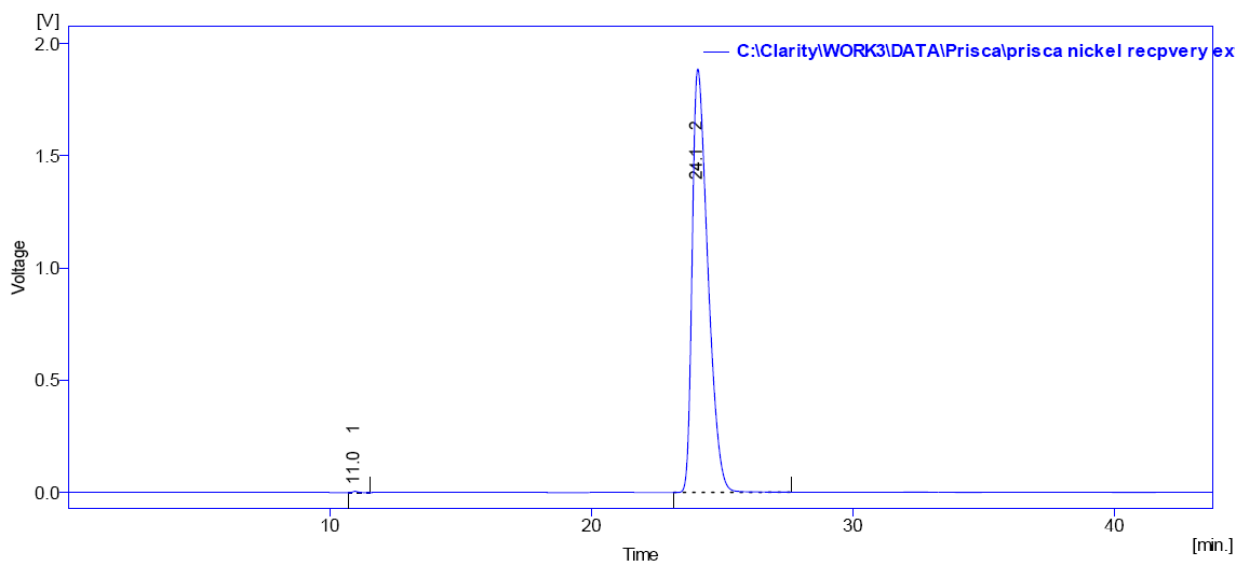


**Figure 4.23** Chromatogram of Toluene after Soxhlet extraction.

Upon treatment of the N-SiO<sub>2</sub> catalyst with sulphuric acid, some nickel was removed. The amount of nickel in solution was determined by ICP-AES and converted to mass in grams. Results on nickel leaching are presented in **Table 4.7**.

**Table 4.7** Results for nickel leaching.

Catalyst	Expected mass of nickel in solution (g) $\pm$ <b>d</b>	Mass of nickel in solution (g) $\pm$ <b>d</b>	Percentage mass of nickel recovered (%) $\pm$ <b>d</b>
<b>N-SiO<sub>2</sub></b>	1.23	0.08	6.71

The results indicate that nickel leaching with sulphuric acid was not effective as expected. The difference in the mass expected and recovered could be due to the mild conditions used in an effort to avoid extreme etching of the carbon nanofilaments. The TEM micrograph of the carbon nanofilaments after nickel leaching is shown in **Figure 4.24**.

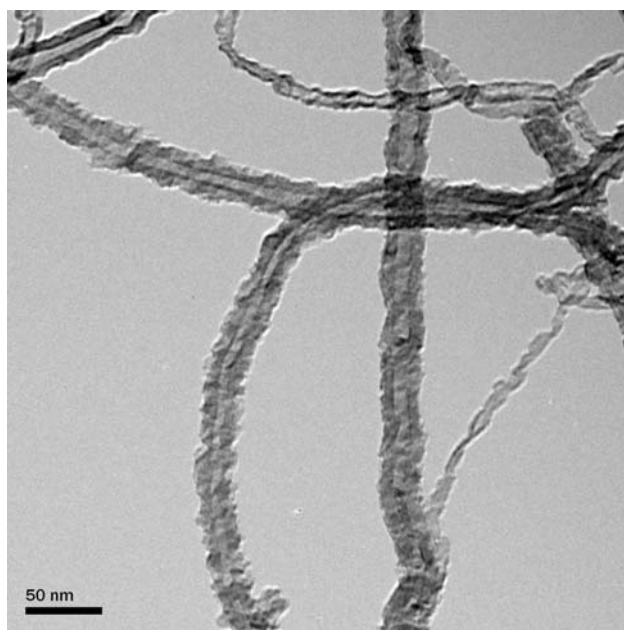


**Figure 4.24** TEM micrograph of the carbon nanofilaments obtained over N-SiO<sub>2</sub> catalyst at 600 °C after nickel leaching.

The TEM micrograph of the carbon nanofilaments after nickel leaching shows that the sulphuric acid etched the carbon nanofilaments to some extent. The rough surface of the etched carbon nanofilaments would provide good catalyst anchoring sites and act as support. However because sulphuric acid was used in Ni leaching, the carbon nanofilaments use as support would be limited to catalytic processes resistant to sulphur poisoning. The etched carbon nanofilaments could be used as nanocomposite fillers.

#### 4.4 References

1. Y. Shirane, S. Nabika, S. Sakamoto, I. Nakashima, *Int. J. Mineral Processing*, 19 (1987) 237-251
2. H.M. Swaan, V.C.H. Kroll, G.A. Martin, C. Mirodatos, *Catal. Today*, 21 ( 1994) 571-578
3. G. Italiano, C. Espro, F. Arena, F. Frusteri , A. Parmaliana, *Catal. Lett.*, 124 (2008)7–12
4. K. Hadjiivanov, M. Mihaylov, D. Klissurski, P. Stefanov, N. Abadjieva, E. Vassileva,y and L. Mintchev, *J. Catal.*, 185 (1999) 314–323
5. D. Chen, K. O. Christensen, E. Ochoa-Fernández, Z. Yu, B. Total, N. Latorre, A. Monzón, A. Holmen, *J. Catal.*, 229 (2005) 82–96
- 6 B. Huang, X. Li, S. Ji, Baolang, F. Habimana, C. Li, *J. Nat. Gas Chem.*, 17 (2008) 225–231
7. J. Juan-Juan, M. C. Roma´n-Marti´nez, M. J. Illa´n-Go´mez, *Appl. Catal. A: General*, 301 (2006) 9–15
8. K.O. Christensen, D. Chen , R. Lødeng, A. Holmen, *Appl. Catal. A: General*, 314 (2006) 9–22
9. P. S. Arora, R. St. C. Smart, *Surf. Interf. Anal.*, 24 (1996) 539-548
10. A. N. Pour, Y. Zamani, K. J. Jozani, J. Y. Mehr, *React. Kinet. Catal. Lett.*, 86 (2005) 157-162
11. A. Loaiza-Gil , M. Villarroel, J. F. Balbuena, M. A. Lacruz, S. Gonzalez-Cort´es, *J. Molecular Catalysis A: Chemical*, 281 (2008) 207–213

12. H. W. Kim , S. H. Shim, J. W. Lee, *Thin Solid Films*, 515 (2007) 6433–6437
13. H. Qiao, Z. Wei, H. Yang, L. Zhu, X. Yan, *J. Nanomaterials*, (2009) 1-5
14. A. K. M. F. Kibria, Y. H. Mo, K. S. Nahm, M. J. Kimb, *Carbon*, 40 (2002) 1241–1247
15. M. A. Ermakova, D.Y. Ermakov, *Catalysis Today*, 77 (2002) 225-235
16. A. Galdikas, C. Descorme, D. Duprez, F. Dong, H. Shinjoh, *Topics in Catal.*, 30 (2004)405-409
17. L. Stievano, N. Kemache, N. Chakroune, J. F Lambert, *Catal. Lett.*, 100 (2005) 169-179
18. J. A. Moulijn, A. E. Van Diepen, F. Kapteijn, *Appl. Catal.*, A 212 (2001) 3-16
19. M. Inoue, K. Asai, Y. Nagayasu, K. Takane, S. Iwamoto, E. Yagasaki, K. Ishii  
*Diamond and Related Materials* 17 (2008)1471-1475
20. J. Sehested, *Catal. Today*, 111 (2006) 103-110
21. S.P. Chai, S.H.S. Zein, A.R. Mohamed, ” A Review On Carbon Nanotubes Production Via Catalytic Methane Decomposition”, 1<sup>st</sup> National Postgraduate Colloquim , School Of Chemical Engineering University of Sains Malaysia, Seri Ampangan (2004) 60-69
22. M. K. van der Lee, A. J. van Dillen, J. W. Geus, K. P. de Jong, J. H. Bitter,  
*Carbon*, 44 (2006) 629–637.
23. S. D. Mhlanga, N.J. Coville, *J. Nanosci. and Nanotech.*, 10 (2010) 1-9
24. H. Abbas, W.M.A.W. Daud, *Int. J. Hydrogen Energy*, 35 (2010) 1160-1190
25. J.I. Villacampa , C. Royo, E. Romeo, J.A. Montoya , P. Del Angel, A. Monzóna, *Appl. Catal. A: General*, 252 (2003) 363–383
26. J. Y. Mehr, K. J. Jozani, A. N. Pour, Y. Zamani, *React.Kinet.Catal.Lett.*, 75

- (2002) 267-273
27. C.A. Querin, *Catal. R. Soc. Chem.*, 1 (2004) 166-206
28. A. M. Venezia, A. Parmaliana, A. Mezzapica, G. Deganello, *J. Catal.*, 172 (1997) 463-470
29. M. G. Donato, G. Messina, S. Santangelo, S. Galvagno, C. Milone, A. Pistone, *J. Phys.: Conference Series*, 61 (2007) 931-935
30. M. S. Dresselhaus, A. Jorio, M. Hofmann, G. Dresselhaus, R. Saito, *Nano Lett.*, 10 (2010) 751-758
31. Z. Li, E. Dervishi, Y. Xu, V. Saini, M. Mahmood, O. D. Oshin, A. R. Biris, A. S. Biris, *Catal. Lett.*, 131 (2009) 356-363
32. C. J. Lee, J. Park, J. A. Yu, *Chem. Phys. Lett.*, 360 (2002) 250
33. D. Bom, R. Andrews, D. Jacques, J. Anthony, B. chen, M. S. Meier, J. P. Selegue, *Nanoletters*, 2 (2002) 615-619
34. J.L. Pinilla, I. Suelves, M. J. Lazro, R. Moliner, J.M. Palacios, *Appl. Catal. A: General* 363 (2009) 199-207
35. H. Li, N. Zhao, C. He, C. Shi, X. Du, J. Li, *Mat. Sci. and Eng. A.*, 473 (2008) 355-359
36. L-H. Teng, T-D. Tang, *J. Zhejiang Univ, Sci. A* 9 (2008) 720-726
37. Z. Sarbak, *React. Kinet. Catal. Lett.*, 84 (2005) 263-270

## CHAPTER 5 CONCLUSION AND RECOMMENDATIONS

### 5.0 Conclusion

This chapter is mainly based on the results obtained in the study of the promotional effects of MgO on 20%Ni/SiO<sub>2</sub> and on the characteristics of the resulting coke deposited over the catalysts. In summary, a two step method for the production of hydrogen and carbon from direct methane decomposition on 20%Ni/SiO<sub>2</sub> catalysts was achieved. The direct decomposition of methane overcomes the limitation of a major CO<sub>x</sub> contamination of the hydrogen gas experienced in other hydrogen production process involving hydrocarbons.

A series of MgO-modified 20%Ni/SiO<sub>2</sub> catalysts of Mg<sub>at</sub>/Ni<sub>at</sub> ratio of 0.1-2.2 were successfully prepared by the co-impregnation method. The highest pseudo steady state methane conversions for all the catalysts were in the range of 45-55% at an optimum temperature of 600 °C. The study revealed that high coke yields on the unmodified and MgO modified 20%Ni/SiO<sub>2</sub> occurred on a catalyst with an optimum particle size of 36 nm, high degrees of reduction and low MgO loadings. This result suggested that Ni catalysed methane decomposition is dependent on the size of the Ni particle and the reducibility of the nickel species.

Characterization of the physico-chemical properties of the conventional unmodified and MgO-modified 20%Ni/SiO<sub>2</sub> catalysts suggest that the incorporation of MgO in 20%Ni/SiO<sub>2</sub> catalysts increased the dispersion and reduced the size of the Ni particles on the support. The excellent mutual solubility between NiO and MgO brought about by their similar crystal dimensions as shown by XRD patterns, favours the formation of Ni<sub>x</sub>Mg<sub>1-x</sub>O solid solution reducing the interaction of the NiO with the silica support and consequently inhibiting the formation of the nickel silicate species. However the Ni<sub>x</sub>Mg<sub>1-x</sub>O solid solution is hard to reduce, hence the progressive addition of MgO to 20%Ni/SiO<sub>2</sub> catalysts reduces the degree of reduction of the NiO species. The shift of the reduction signals to higher temperatures in TPR profiles of MgO-modified 20%Ni/SiO<sub>2</sub> catalysts also indicates a decrease in the reducibility of the NiO species.

The formation of  $\text{Ni}_x\text{Mg}_{1-x}\text{O}$  solid solution reduces the fraction of Ni active sites available for methane decomposition.

The TEM studies revealed that coke, in the form of carbon nanofilaments, grew by the tip growth mechanism on both the unmodified and MgO-modified 20%Ni/SiO<sub>2</sub> catalysts. This suggests that the incorporation of MgO in 20%Ni/SiO<sub>2</sub> catalysts did not promote strong metal-support-interactions (SMSI) to promote the carbon nanofilament base growth mechanism; hence the Ni particle was detached from the support during carbon nanofilament growth. The tip growth mechanism suggests that the growth of the carbon nanofilaments may lead to the carbon nanofilament acting as a support to the active Ni particle, ensuring that it is continuously exposed to the reactant methane gas. The tip growth mechanism suggests that catalyst deactivation through pore blockage is unlikely.

A higher coke yield was obtained over the unmodified 20%Ni/SiO<sub>2</sub> (N-SiO<sub>2</sub>) catalyst compared to the MgO-modified catalyst (1M9N-SiO<sub>2</sub>) regardless of the similar degree of reduction, Ni particle dispersion and size. This result suggests that the addition of MgO to the 20%Ni/SiO<sub>2</sub> catalyst exerts a coke suppression effect. High methane conversions exhibited by MgO-modified catalysts during the pseudo-steady state may be explained by considering reduced contact between the active Ni particle at the tip of the carbon nanofilament and the MgO on the support.

The N-SiO<sub>2</sub> catalyst had the best catalytic performance in terms coke capacity (3.0g<sub>C</sub>/g<sub>cat</sub>). The optimum ratio of  $\text{Mg}_{\text{at}}/\text{Ni}_{\text{at}}$  in 20% Ni/SiO<sub>2</sub> for methane decomposition was 0.1 in the 1M9N-SiO<sub>2</sub> catalyst with a coke capacity of 2.6g<sub>C</sub>/g<sub>cat</sub>. Values of  $\text{C}/\text{Ni}_{\text{red}}$  per gram of spent catalyst indicate that the presence of MgO only exhibits its beneficial effect over N-SiO<sub>2</sub> (16 g<sub>C</sub>/g<sub>Nired</sub>) in 2M1N-SiO<sub>2</sub>, with  $\text{Mg}_{\text{at}}/\text{Ni}_{\text{at}}$  ratio of 2.2 (22 g<sub>C</sub>/g<sub>Nired</sub>) and 1M1N-SiO<sub>2</sub>, with  $\text{Mg}_{\text{at}}/\text{Ni}_{\text{at}}$  ratio of 1.0 (21 g<sub>C</sub>/g<sub>Nired</sub>) catalysts, in terms of carbon yield per reduced fraction of NiO particles per gram of spent catalyst. These results indicate that it is not worthwhile to modify the 20%Ni/SiO<sub>2</sub> catalysts with MgO for direct methane decomposition.

The 1M1N-SiO<sub>2</sub> catalyst with an average Ni particle size of 36 nm had higher coke yield than the other MgO-modified 20%Ni/SiO<sub>2</sub> catalysts with bigger particle sizes

and higher degrees of reduction. The carbon nanofilament diameter was assumed to be similar to that of the Ni particle from which it was grown. The carbon nanofilaments diameters were within a range of 20 nm-100 nm. No carbon nanofilaments exceeded a diameter of 100 nm. Therefore it is suggested that Ni particles in 20%Ni/SiO<sub>2</sub> catalysts exceeding 100 nm do not facilitate methane decomposition.

The 1M9N-SiO<sub>2</sub>, 1M4N-SiO<sub>2</sub> and 2M1N-SiO<sub>2</sub> catalysts had similar Ni particle dispersion and size but different degrees of reduction had variations in coke yield. The highest coke yield was obtained over the 1M9N-SiO<sub>2</sub> catalyst with highest degree of reduction. This result suggested that high degrees of reduction of catalysts were important in methane decomposition.

Raman spectroscopy studies on the carbon nanofilaments obtained over unmodified and MgO-modified 20%Ni/SiO<sub>2</sub> catalysts at 600 °C did not show variation in the A<sub>D</sub>/A<sub>G</sub> ratios indicating that the MgO presence had no effect on the degree of structural order of the carbon nanofilaments. All the carbon nanofilaments obtained on the catalysts showed a high degree of disorder at 600 °C.

Thermogravimetric analysis of the carbon nanofilaments in air showed that all the carbon nanofilaments had an onset oxidative reactivity from temperatures as low as 600 °C. A reasonable explanation could be that there is no variation in the degree of order in the carbon nanofilaments as suggested by the Raman spectroscopy data. However, after the onset temperature of oxidation (600 °C), the degree at which the carbon oxidised varied slightly within the samples, probably due to differences in defect site densities and carbon nanofilament diameters. Defect sites are permeable to oxygen and consequently facilitate rapid oxidation. Smaller diameter structures are highly reactive toward oxygen.

Infrared spectroscopy studies revealed that the coke obtained adsorbed strongly and hence did not reveal much information on adsorbed species present on the spent catalysts.

The processing of the spent catalyst for reuse was attempted through the separation of metal and carbon nanofilament but was found to be inefficient. The possible applications for reuse included; (a) sulphuric acid-leached Ni for use in electroplating as nickel sulphate and (b) purified carbon nanofilaments for use in nanocomposites. The coke had little toluene-soluble components and attempts at separating coke from the spent catalyst through nickel leaching with sulphuric acid were ineffective as the amount of nickel leached was too low. Furthermore, upon leaching treatment the carbon nanofilaments were rough due to acid etching. The rough carbon nanofilaments could be possibly be used for as fillers in nanocomposites

### **5.1 Recommendations**

- Develop methods of catalyst preparation that vary Ni particle size in 20%Ni/SiO<sub>2</sub> catalysts for methane decomposition.
- Recommend a more comprehensive study on CO<sub>2</sub> capture and storage will need to be performed to ensure the sustainability of H<sub>2</sub> production from methane.